PHASE CHANGE TEMPERATURE SENSOR FOR HIGH RADIATION ENVIRONMENT: MATERIAL, ADDITIVE TECHNOLOGY AND STRUCTURE DEVELOPMENT

by

Al Amin Ahmed Simon

A dissertation

submitted in partial fulfillment

of the requirements for the degree of

Doctor of Philosophy in Electrical and Computer Engineering

Boise State University

August 2021

BOISE STATE UNIVERSITY GRADUATE COLLEGE

DEFENSE COMMITTEE AND FINAL READING APPROVALS

of the dissertation submitted by

Al-Amin Ahmed Simon

Dissertation Title: Phase Change Temperature Sensor for High Radiation Environment: Material, Additive Technology and Structure Development

Date of Final Oral Examination: 26 May 2021

The following individuals read and discussed the dissertation submitted by student Al-Amin Ahmed Simon, and they evaluated the student's presentation and response to questions during the final oral examination. They found that the student passed the final oral examination.

Maria Mitkova, Ph.D.	Chair, Supervisory Committee
Harish Subbaraman, Ph.D.	Member, Supervisory Committee
Kurtis Cantley, Ph.D.	Member, Supervisory Committee
David Estrada, Ph.D.	Member, Supervisory Committee
Marc Cahay, Ph.D.	External Examiner

The final reading approval of the dissertation was granted by Maria Mitkova, Ph.D., Chair of the Supervisory Committee. The dissertation was approved by the Graduate College.

DEDICATION

To my wife Sajia for her support and motivation over the years.

ACKNOWLEDGMENTS

First, I would like to express my gratitude to my academic advisor, Dr. Maria Mitkova, for opening this door of opportunity for me at Boise State University. Her support and mentoring have helped me to enhance my career and made me a better human being. I would also like to extend my gratitude towards my committee members, Dr. Harish Subbaraman, Dr. David Estrada and Dr. Kurtis Cantley, for helping me accomplish this milestone. I especially would like to extend my gratitude to Dr. David Estrada and Dr. Harish Subbaraman for providing me access to their lab facilities. Furthermore, I thank Dr. Isabella van Rooyen for creating an internship opportunity in Idaho National Lab (INL) that helped me launch my first research project. Also, I would like to thank Dr. Brian Roberds for allowing me to do an internship at L3Harris. I am thankful to Peter Miranda, Travis Gabel and all the staffs at IML and Boise State Surface Science Lab for their patience, training, and assistance throughout my work. I am grateful to the ECE staff for their diligent work with travel, finances, and resources at Boise State, especially Jenn Ambrose and Kelly Martinez. My gratitude extends to Dr. Harish Subbaraman for his guidance and expertise in printing. Also, I am thankful to my colleagues Dr. Twinkle Pandhi (Ink Formulation and Printing), Lyle Jones (Electrical Characterization), Henri Kunold (Material Characterization), Shah Mohammad Rahmot Ullah and Dr. Bahareh Badamchi (Optical fiber and Plasmonic Device Characterization). I would also like to acknowledge my friends from both Boise and Dhaka, who have always been there for emotional and motivational support. Touhid, Prottoy, Nabil, Maruf,

Pradeep, Rafat, Sadi, Shihanuk, Masud, Shahed, Moinul, Amy, Karib, I am genuinely thankful for all your help and support. I am also thankful to Mr. Marshall Mathers for all his songs that have motivated me in my worst times. Lastly, I would like to thank my family, who prepared me for the realities of life and tried to provide me with all the world opportunities to be my best.

FUNDING

This work has been funded by Department of Energy grant number DOE-NE 0008691 and NSUF-RTE 19-2832. We gracefully acknowledge DOE's contribution to the advancement of our research.

ABSTRACT

Performance of any sensor in a nuclear reactor involves reliable operation under a harsh environment (i.e., high temperature, neutron irradiation, and a high dose of ionizing radiation). In this environment, accurate and continuous monitoring of temperature is critical for the reactor's stability and proper functionality. Furthermore, during the development and testing stages of new materials and structural components for these systems, it is imperative to collect in-situ measurement data about the exact test conditions for real-time analysis of their performance. To meet the compelling need of such sensing devices, we propose radiation-hard temperature sensors based on the phase change phenomenon of chalcogenide glasses. The primary goal is to resolve the monitoring of the cladding temperature of light water and metallic or ceramic sodium-cooled fast reactors within a temperature range of 400°C to 600°C. This work is focused on studies of Ge-Se(S) chalcogenide glasses that have crystallization temperatures in this range. Each chalcogenide glass transforms and becomes crystalline at a specific heating rate at a definite temperature. As a result of this, both the electrical resistance and optical properties of the materials change. As this is the first time such devices have been fabricated, this work submits new data regarding materials research, various device structures, fabrication, performance, and testing under irradiation. The application of these materials in devices usually involves the formation of a thin film that works as an active layer. Traditionally, thin films are prepared by thermal evaporation, sputtering or chemical vapor deposition and they require high vacuum machinery and patterning

applying photolithography. To avoid using such heavy machinery and costly fabrication processes, we investigate the formulation of nanoparticle inks of chalcogenide glasses, the formation of printed thin films using the inks, low-cost sintering and demonstrate their application in electronic and photonic sensors utilizing their phase transition effects. The printed chalcogenide glass films showed similar structural, electronic and optical properties as the thermally evaporated films. The newly developed process steps reported in this work describe chalcogenide glasses nanoparticle inks formulation, their application by inkjet printing and dip-coating methods and sintering to fabricate phase change temperature sensors. To interpret and predict the printed films' performance, Raman spectroscopy, X-ray Diffraction Spectroscopy, Energy Dispersion Spectroscopy, Atom Force Microscopy, temperature dependent Ellipsometry, and other methods are used. An essential part of materials' behavior is related to the materials' and devices' response to ion beam irradiation. Both experimental data and simulation are analyzed to study the effect of irradiation. Based on the different working principles, electrical, optical and plasmonic temperature sensors are investigated. An array of optical fiber devices fabricated with different chalcogenide glasses is shown to perform a real-time temperature reading. This work could be used as a paradigm for sensor fabrication and testing for high radiation environments and nanoparticle inks of chalcogenide glasses formulation and their application by inkjet printing and dip-coating. The most novel outcome of this work adds chalcogenide glasses to the list of inkjet printable materials, thus opening up an opportunity to achieve arbitrary structures for optical and electronic applications without photolithography.

TABLE OF CONTENTS

LIST OF TABLES

LIST OF FIGURES

LIST OF ABBREVIATIONS

ChG	Chalcogenide Glass
TE	Thermally Evaporated
CS	Corner-Sharing structure
ES	Edge-Sharing structure
ETH	Ethane-like structure
Ge	Germanium
Se	Selenium
S	Sulphur
SET	The device is crystallized by heating, the high current state
RESET	The device is brought down to amorphous state by electrical pulsing
n	Refractive Index
k	Extinction Coefficient
VASE	Variable Angle Spectroscopic Ellipsometry
SAED	Small Area X-ray Diffraction
CD/DVD	Compact Disc/ Digital Video Disc
PCM	Phase Change Memory
DPA	Displacements per atom

CHAPTER ONE: INTRODUCTION

Nuclear technology has developed and become an integral part of the world economy at a staggering rate in the last decade. According to the International Atomic Energy Agency (IAEA) statistics, 438 power reactors were operating globally in 2015. The US alone had 99 of them, and 19.5% of electricity in the US is generated from nuclear reactors [1]. Though accidents like in Fukushima caused reduced investment in this sector, with low-cost production and low carbon emission, the essentiality of the nuclear reactors in the power sector has been increased.

New technologies have been developed to sense and control systems with precision to ensure the safety and reliability of the reactors. The reactors and the entire operation of the plant are controlled and monitored by the instrumentation and control (I&C) systems. According to IAEA, the I&C has three significant roles [2].

a. They construct the nervous system of the plant and decisions are taken by the operator based on their reading.
b. The precision and reliability of sensors are the center point for automatic control. An accurate and fast response from the sensors is essential for the operator to make a decision.
c. The I&C safety systems work as a safety lock to prevent any undesired conditions from the outcomes of any slip-ups made by both the operator and the automatic control system. During any abnormal conditions, they

provide instant automatic action to prevent reactor melting or other environmental hazards.

To maintain uninterrupted operation and safety of a plant, pressure and temperature sensors are two of the essential instruments [3]. This project is focused on the development of novel in-situ, reusable temperature sensors. The idea is to integrate temperature monitoring using a combination of electronic and photonic properties of radiation hard devices and heat-induced crystallization of chalcogenide glasses (ChGs).

Despite various advancements in sensing technology, the primary mechanism of temperature measurement has not changed significantly since the first-generation power plants. To work in a high radiation and temperature environment, sensors must be radiation hard and maintain their micro and macroscopic integrity under high temperatures. They also must withstand high neutron flux (10^{11} - 10^{14} $cm^{-3}s^{-1}$). These conditions make it very difficult to build an electronic sensor that is impervious to radiation. Some of the most widely used sensors in high radiation environments are described next.

Current Technologies

Resistance Temperature Detectors (RTDs)

RTDs are based on the phenomena that the electrical resistance of metals rises with temperature because of the random motion of electrons and lattice vibration increase with the temperature inside the metal. There are two types of RTDs used in nuclear plants, direct immersion and thermowell mounted [3]. Their use is prolific in CANada Deuterium Uranium (CANDU) reactors [3], [4]. Platinum is typically used to build RTDs, and nickel or copper are also used. Most RTDs are coiled wire wrapped around a

ceramic or glass core. The relation between temperature and resistance change is very close to linear but non-linearity is observed in high temperature [5].

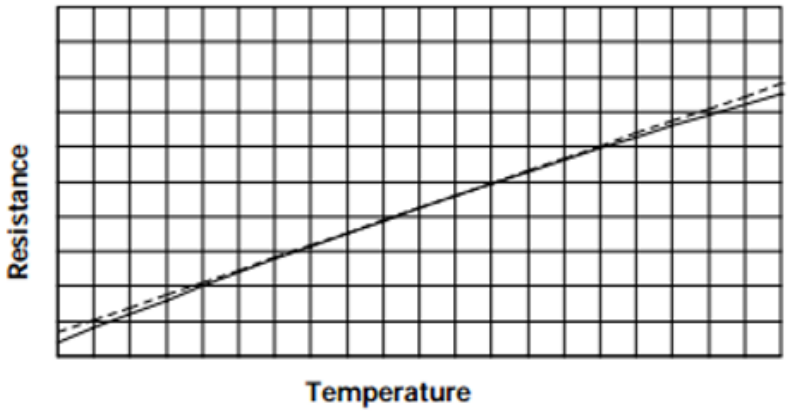

Figure 1.1 RTD Resistance vs. Temperature. The dashed line is reference [5].

RTDs need external current to measure the resistance change. Thus, with measuring current I, I^2R heating inside the RTD device presents itself as a problem known as "self-heating" [4], which gives an erroneous rise to the reading. Also, gamma heating due to radiation absorption and heat loss through thermowell (known as "stem loss" [6]), used to isolate RTDs causes error in reading [4]. The thermal neutron cross-section of the most widely used metal in RTDs, platinum (Pt), is relatively low 10.3 [7], making it a good choice for nuclear-related application.

Thermocouple:

In 1821, Thomas Seebeck discovered that when two different metals were joined at both ends and one end is at a different temperature than the other, an electromotive force (EMF) is induced, thus current flows. If metal is heated, the electrons inside the metal gain kinetic energy and move from the hot to the cold end [8]. This is called the Seebeck effect. The induced voltage is determined by the Seebeck coefficient (unit V/°C), which is unique for each material [8]. When two metals with different Seebeck

coefficients are joined together, there is a net voltage difference between the junctions and current flows. Since the Seebeck coefficient is unique for each material, heating leads to a change in the generation of induced voltage per unit temperature change [9]. Thermocouples are temperature sensors based on the Seebeck effect.

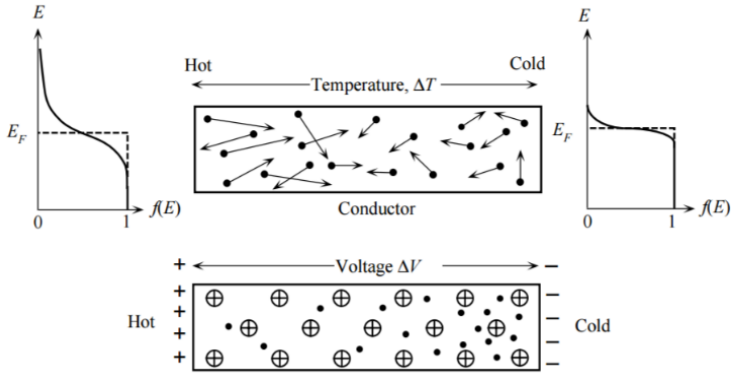

Figure 1.2 The Seebeck effect [9].

For more than 50 years, the most typical in-pile temperature measurement has been done by thermocouples [9]. Below is a list of the most common types of thermocouples used in reactors.

Thermocouples with metal sheath and mineral insulation [9]:

Below 1100°C: - Ni-Cr / Ni-Al (K-type)

- Ni-Cr-Si / Ni-Si (N-type)

Above 1100°C: - W-Re alloys (C-type)

One of the main problems that occurs in thermocouples is drift due to transmutation (effect of neutron absorption) or because of the material degradation at high temperature (above 1100°C) [10]. It is also determined that the wire diameter plays a vital role in Type-K and N thermocouples reliability [8], [11]. With heat treatment,

thermocouples' reliability can be improved but heat treatment temperature has a more significant effect than the duration [10].

Melt Wire Sensors

Melt wires do precisely what their name suggests. Wires of various metals which melt at various temperatures are kept and allowed to melt and thus, the peak temperature reached is measured. Melt wires are included in non-instrumented tests to measure the peak temperature.

Theoretically, good melt wires are pure materials with a single melting temperature or alloys with well-defined eutectics [12]. They also should have low cross-sections to reduce the effect of transmutation and high geometry change should be observed. The density of the wire, local gamma flux and thermal resistance between surroundings and the wire affect its performance. The higher the precision is needed, the higher the number of wires are needed. Some materials and corresponding melting temperatures could be found in a library that Idaho National Lab has published [12].

Surface Acoustic Wave Sensors (SAWs):

These are various microelectromechanical systems (MEMS) whose working principle depends on the modulation of surface acoustic waves to determine a change in a physical property. They transduce an electrical signal into a mechanical wave which is perturbed by a physical phenomenon.

The rudimentary SAWs consist of a piezoelectric substrate, an interdigitated transducer (IDT) on one side of the surface of the substrate, and another IDT on the other side. The IDTs are an array of interleaved metal strips that can be excited by an external source. The distance between the IDTs is the path the acoustic wave propagates through

and is known as the delay-line. The basic idea is to generate a mechanical wave into the substrate whose temperature is to be measured and then measure the signal delay by the output transducer. The output transducer converts the vibration into the electrical signal and completes the measurement. Another way of preparation of SAWs is by keeping the output IDT open circuit and the reflected waves from the open circuit IDT are then converted to an electrical signal. The most important factor is that temperature influences the round-trip delay [13]. Four effects that may cause the ultrasonic wave velocity to change have been used in these sensors [13]:

a. Mass loading of the surface
b. Change of material stiffness
c. Change of electrical conductivity at the surface
d. Change of permittivity at the surface

With the increase of temperature, the vibration of the atoms increases and reduces Young's modulus. So, the materials become stiffer. This change of stiffness influences the wave propagation velocity.

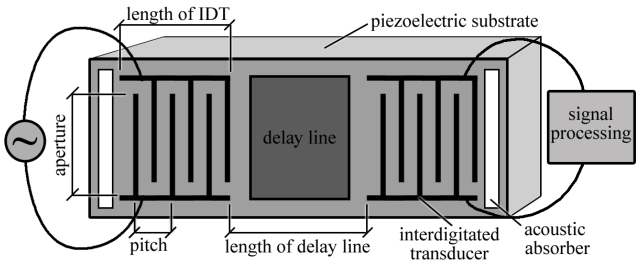

Figure 1.3 Integrated Transducers [14].

The performance of piezoelectric materials is influenced by radiation, high temperatures, and pressure. A study showed that Bismuth Titanate is capable of transduction up to 5 $x10^{20}$ n/cm^2, Zinc Oxide is capable of transduction up to at least 6.27

$x10^{20}$ n/cm^2, and Aluminum Nitride is capable of transduction up to at least 8.65 $x10^{20}$ n/cm^2 [15].

For their stability in ultra-high temperature, Langasite (LGS), $LiNbO_3$ (LN), AlN and $YCa_4O(BO_3)_3$(YCOB) are the most common piezoelectric materials. HT YCOB devices show higher stability and reliability even at temperatures over 1,000°C [16].

Fiber Bragg Grating Sensors (FBG)

Among optical sensors, the FBG, which reflect a wavelength of light that shifts in response to variations in temperature (and strain) because of change in periodicity and shape, are widely used. However, there is a requirement that the Radiation-Induced Absorption (RIA) of light in the fiber should be within a specified limit [16], [17].

FBGs are made by holographic interference or phase mask to expose a short length of photosensitive fiber to a periodic distribution of light intensity. The refractive index of the fiber is permanently altered as a function of the light intensity to which it is exposed. The resulting periodic variation in the refractive index is called a fiber Bragg grating and both temperature and strain induce an effect on the refractive index [18]. So, the reflected wavelength changes with the temperature variation.

FBGs go through decay in reflectivity with elevated temperature and the decay decreases with time in a quasi-stable value [19]. Thermal annealing is a handy procedure to reduce this decay. They can measure up to 800°C with type II gratings [19]. The hollow-core photonic fibers are found to be radiation hard. They are found to withstand a fast neutron fluence of 10^{20} n/cm^2 and an ionizing dose of 16 GGy for both single and multimode fibers. When considered that RIA measurements losses < 10 dB are

acceptable for Optical Fiber Sensors (OFS) in reactors, OFS can be used if the spectral range is 800 to 1100/1200 nm [20].

One-centimeter resolution temperature measurements in a high radiation environment using Rayleigh scatter in single-mode fibers over various coatings and dopant concentrations were successfully achieved [21]. The result of this study is shown in Figure 1.4. The fibers used in this experiment are

a) SMF28 – Polyamide coated,
b) 1550 nm Silica core – Acrylate coated,
c) 1550 nm 20 wt% GeO doped – Acrylate coated
d) 1300 nm – Copper coated. The SMF-28 fiber and 1300nm copper-coated fiber both have Germania-doped cores, approximately 5 wt% GeO.

The noncontact fiber-optic temperature sensor is also a useful device for temperature monitoring. It demonstrated high effectivity in sensing spent fuel water pool temperature. AgCl:AgBr polycrystalline fiber - an infrared optical fiber, was used in the experiment to operate between 30-70°C.

Johnson Noise Thermometers (JNT)

Noise thermometry has been newly employed in temperature measurements in nuclear plants. Using these sensors, temperatures in the range of 1000-2000°C can be measured [22]. The JNTs measure the Johnson noise, which is a physical phenomenon that due to a temperature change, a thermal agitation of charge carriers occurs inside a conductor even with zero electrical excitation [23]. Johnson noise is a fundamental representation of temperature rather than a response to temperature, they are invariant to chemical and mechanical changes in the sensor material property [24].

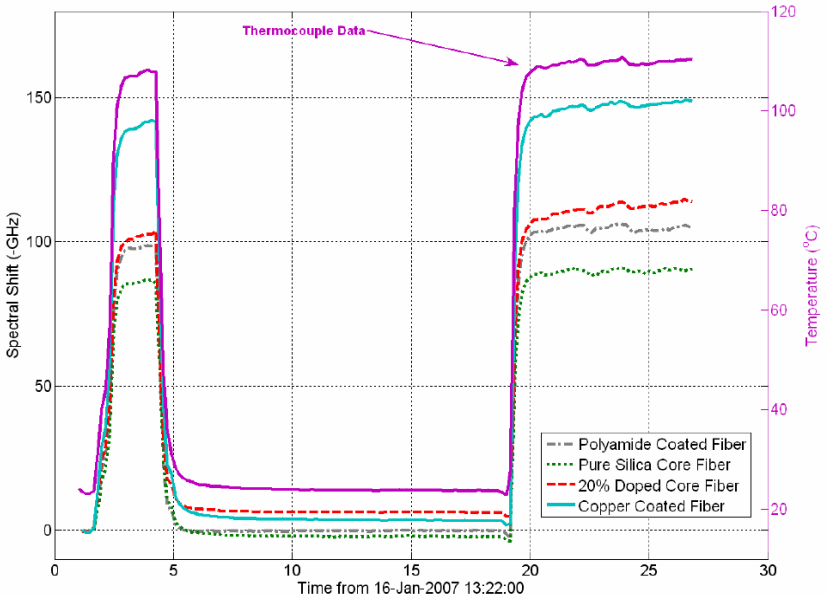

Figure 1.4 Spectral shift at high neutron fluence area (lowest values are found when the reactor was shut off). In all four cases, evidence of linear correlation to temperature is found. The nonlinearity between 40-50°C can be explained as a result of the rapid temperature increase during reactor startup [21].

Due to the small-signal measurement requirement, JNTs are challenging to implement but they can be applied to the parallel of RTDs without altering the configurations [24]. A JNT developed at Oak-Ridge National Lab (ORNL) is proposed to employ in a SP-100 space reactor, which requires 1% measurement uncertainty at 1375K and 8 seconds' response time without maintenance for 7 years [25].

All these temperature sensors have their own merits and demerits. Indeed, based on the physics and fabrication, different types of materials are needed for each type of sensor and the fabrication of such devices requires various types of machinery. On the other hand, the phase change in ChG can be utilized to fabricate electrical, optical and plasmonic temperature sensors. The idea about phase change devices has been applied in the year 2012, by a group of researchers from International Business Machines (IBM) for creation of a phase change temperature sensor [26]. It was proposed to measure the

internal temperature of a chip when it reaches a specific temperature. The phase change material (PCM) proposed for this device uses a ternary chalcogenide glass, $Ge_2Sb_2Te_5$ (GST-225). GST-225 crystallizes at around 160°C and can be re-amorphized by melting it at 600°C. The material shows lower resistivity in the crystal phase than in amorphous. By supplying a constant voltage across it and measuring the current, the temperature can be monitored to see if it has reached 160°C. The structure of the device is shown in Figure 1.5.

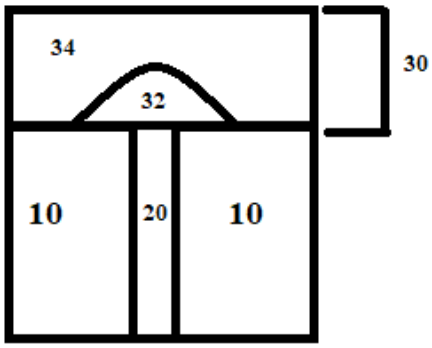

Figure 1.5 A typical phase change temperature sensor (PCT) element structure [26].

The sensor has a dielectric layer 10, a heating element 20, and a PCM element 30. The PCT comprises a phase changing portion 32 and a crystalline portion 34. The phase-changing portion 32 is hemispherical. Although both 32 and 34 are made from the same PCM, only the phase-changing portion 32 switches between an amorphous state and a crystalline state, while the crystalline portion stays crystalline. The schematic here shows the measuring unit. The top electrode (on top of 30) and bottom electrode (beneath 10 and 20) are omitted here.

The structure, material and operation of this sensor are the same as any phase change memory device, with only one exception. Instead of electrical pulsing (PC

Memory), the sensor crystallizes when the ambient temperature reaches its crystallization temperature. Amorphous to crystalline phase transition changes the electrical resistance and optical properties (refractive index *n* and extinction coefficient *k*).

There are a large number of chalcogenide glasses from different systems (e.g., Ge-Se, Ge-S, Ge-Sb-Te), each crystallizes at different temperatures based on their composition and the heating rate. Moreover, due to a large number of defects in their molecular structure, these materials show high tolerance for both ionizing and non-ionizing radiation.

Since both optical and electrical properties of materials stem from the molecular structure, arrangement of structural units and bandgap, it is imperative to study these materials experimentally. Moreover, crystallization kinetics plays a crucial role in the performance of the devices. Before going further into the detail of the experiments and collected data analysis, a theoretical analysis based on the literature review is necessary. Next, the chemistry of chalcogenide glass, glass formation, crystallization kinetics and the underlying reason behind their radiation hardness are discussed.

To our best understanding, among the chalcogenide glasses, Germanium (Ge)-Selenium (Se) and Germanium (Ge)-Sulphur (S) systems are the perfect candidates. The reasons for choosing compositions from these systems are radiation hardness, expectation for high crystallization temperature, based on their glass transition temperature data, their stable glass formation in quite a wide compositional region and high electrical and optical contrast between amorphous and crystalline phase. We will explain these properties of the Ge-Se and Ge-S systems. We will begin with a general description of S, Se and Te as they are suitable glass formers with moderate bonding strength, which allows for high flexibility of the structures built with these elements.

Introduction to Chalcogenide Glass and Crystallization

Electronic Structure and Bond Formation Chalcogenide Glasses

Chalcogens are group 16 elements. The chalcogen elements have 2s and 4p electrons in their outer shell. The p electrons are the main reasons behind chalcogens' optical and electrical properties. Two of these electrons participate in covalent bonding with other atoms and the remaining two p electrons form a pair –the so-called "lone pair" (LP) because both electrons belong to the same atom. During bond formation, the s electrons do not participate because they are in a low energy condition and paired.

Properties of Chalcogenide Glasses

The use of thin films of a particular ChG, which have unique properties of high thermal stability and high radiation stability, is needed for the proposed devices. These glasses contain a chalcogen element – sulfur, selenium, or tellurium combined with other elements and are amorphous. Since for this particular study, only the most temperature stable ChGs are of interest, we will regard the properties of Ge- containing ChG and in a broader aspect, ChG containing elements from group 4 of the Periodic table. The reason for this is that the thermal stability of the ChG is a function of the strength of the chemical bonds between the elements forming the glass and the coordination in the structure of the glasses. In the case of Ge-containing ChG, covalent bonding forms between Ge and the chalcogen elements. Ge has 2s and 2p electrons in its outer shell, which, like in carbon, undergo sp3 hybridization forming four equally strong covalent bonds under an angle of 103°. They connect to the two p-electrons of chalcogen elements which participate in chemical bonds, making the chalcogen elements two-fold coordinated. At these valent conditions, tetrahedral structural units form with the Ge atom

in the center of a tetrahedral pyramid with the chalcogen elements in its corners. Since the glasses are amorphous materials, which have a short-range order satisfying their valent states but lack a long-range order, the elements building them can be combined in many different combinations within the glass forming regions. This allows the structural units to be arranged in different configurations. Sulfur atoms create chains with other sulfur atoms where the bond angle is 105°. Within a chain, there are two specific locations where each of the sulfur atoms can be located. These locations are known as eclipsed (cis) or staggered (trans) configurations, as shown in Figure 1.6 [27].

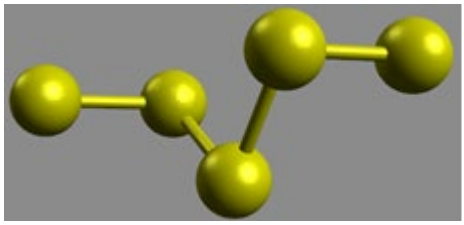

Figure 1.6 Sulfur atoms within a sulfur chain.

Sulfur also forms *orthorhombic* rings with 8 sulfur atoms with a trans configuration at bond angles of 105º. This *orthorhombic* structure is shown in Figure 1.7 [27].

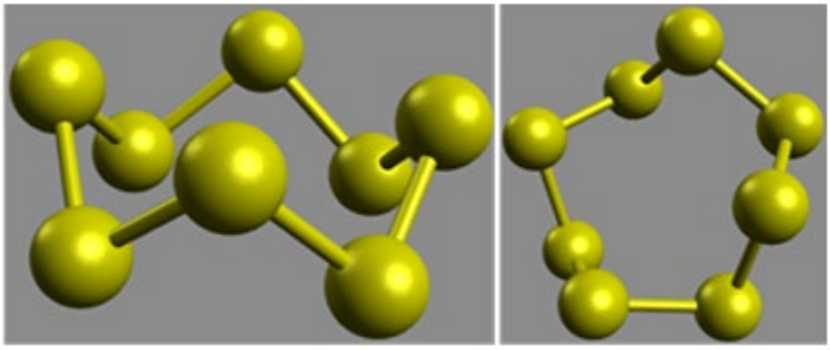

Figure 1.7 *Orthorhombic* sulfur rings S_8 a) side view b) front view.

In sulfur-rich glasses, the sulfur rings can phase separate from the remainder of the glass network, which is the main reason for the smaller glass formation region compared to the selenium-containing system. Additionally, sulfur has a significantly higher partial pressure, which is an attribute that is unique to sulfur-containing glass in contrast to the other two chalcogen-containing glasses.

On the other hand, Selenium forms only hexagonal chains held together by Van der Waals forces acting between them. Unlike Sulfur *orthorhombic* rings, these chains are parallel to each other, and each atom has a bond angle of approximately 103.1º [28].

Like Selenium, Tellurium also forms long spiraling hexagonal chains held together by Van der Waals forces [29]. Tellurium is considered a semi-metal and has characteristics like metals, such as a very narrow bandgap, high conductivity, and lustrous appearance. Additionally, because of the weak strength of the Ge-Te bonds, the glasses from the Ge-Te system have very low characteristic temperatures, because of which we are not considering them in this project.

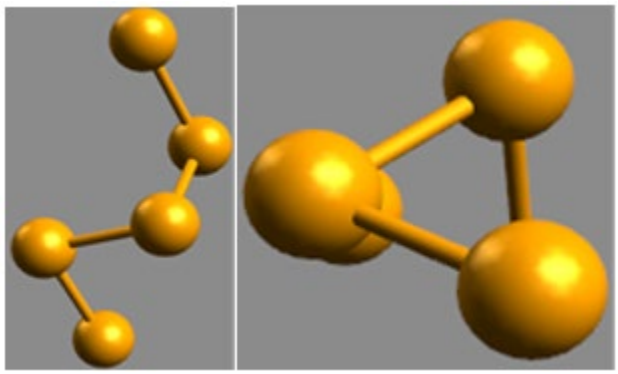

Figure 1.8 Selenium chains a) configuration of the chains b) top view of the chains.

The inclusion of Ge leads to the formation of a variety of tetrahedral configurations in which the tetrahedrons can be connected with their corners – forming corner-sharing (CS) building blocks and their edges, forming edge-sharing (ES) building blocks. When the Ge content is very high and there are not enough chalcogen atoms to satisfy its fourfold coordination, Ge-Ge bond formation is possible which leads to occurrence of ethane-like structure or distorted rock salt structure, as shown in Figure 1.9.

Glass Formation

Based on entropy and structural order, materials are classified into four types – solids, liquids, gases, and plasma. Solids have the lowest entropy while gases and plasma have the highest and liquids lie in between. The structural order is another factor for the solids, which classifies the solids into single crystalline, polycrystalline, and amorphous. Amorphous materials have short-range order but no long-range order. Single crystalline materials have long-range orders and polycrystalline consists of several single-crystalline clusters with grain boundaries between the different types of crystals. Theoretically, it is possible to create glass from most of the materials by cooling their melts at an appropriate rate, but they may not be stable. Most glasses are made from a specific composition that needs specific cooling rates. The compositional region in which the materials can vitrify is called the glass-forming region and is of various extent.

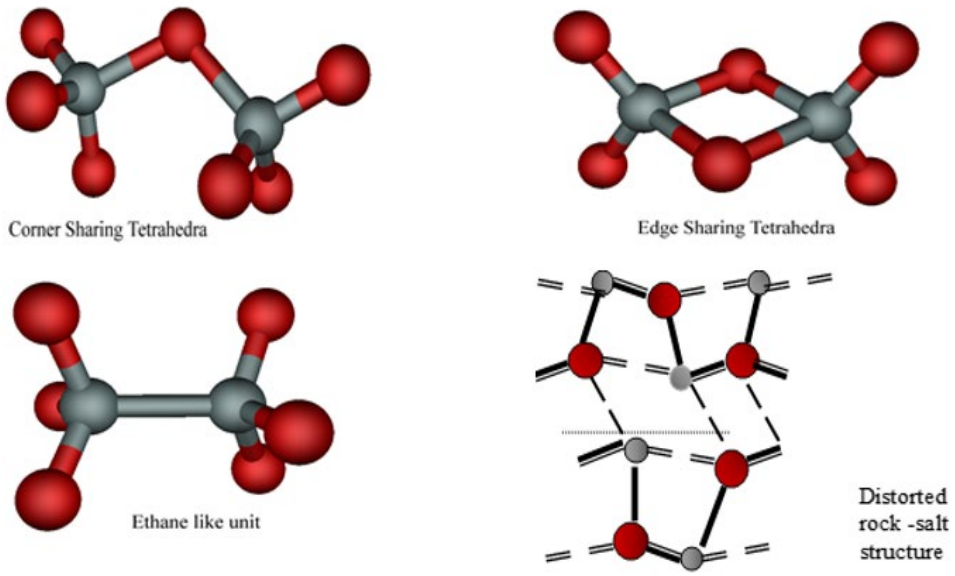

Figure 1.9 Structural building blocks of Ge containing chalcogenide glasses (Red=Se, Grey=Ge).

Bond constraint theory explains glass-forming capability [30]. To quantify the ability of a composition to become glass, Mean Coordination Number (MCN) is used. Any composition with an MCN of 2.4 can easily be transformed into a glass because this MCN indicates a situation where the number of constraints per atom is equal to the degrees of freedom of each atom. MCN, r is expressed by

$$r = Z_A \frac{x}{100} + Z_B \frac{100 - x}{100} \quad (1.1)$$

Here Z is the number of additional valence electrons; it is required to satisfy the 8N rule of bonding. Subscripts A and B refer to elements A and B. M. F. Thorpe further developed the relation between glass quality and MCN. According to him, r = 2.4 is the transition point from floppy (r < 2.4) to rigid (r >2.4) structure of glasses [31]–[35]. Chalcogen-rich glasses are floppy, which means they have more flexibility in their bonds because of their low coordination. In between the floppy and rigid states, an intermediate

phase was discovered by P. Boolchand [36]–[39]. In this phase, glasses are non-stressed rigid and they do not display aging effect.

The usual way to produce chalcogenide glasses is by melt quenching technique. Elements are measured precisely to match the composition and then placed inside an ampule. Then the pressure inside the ampule is reduced to a vacuum (10^{-6} torr) and sealed. The sealed ampoule is then placed inside a furnace and the furnace is programmed to assure the needed temperature regime to produce glass. For the binary chalcogenide glasses, it normally takes 5 – 10 days to produce glass. The furnace heats up the ampule above the melting temperature of the elements in it, so that the materials melt completely and mix and homogenize uniformly. The mixing process can be improved by rocking the furnace with the chalcogenide material.

When the synthesis is complete, the ampules are taken out of the furnace and quenched in water. While cooling, when the material reaches the glass transition temperature (T_g), it starts becoming solid. During the transition, the viscosity of the material goes so high that it cannot flow and can be identified as solid. The quenching must be fast to freeze the order characteristic for the liquid material around the glass transition temperature and keep the material glassy (amorphous). If the material is cooled rather slowly, the liquid then solidifies by becoming crystalline. So, the cooling rate is a crucial factor in the formation of glasses [40], [41]. Finding the T_g for any material can be done by differential scanning calorimetry (DSC). It is an exothermic step change in the DSC curve. During the glass transition, the heat capacity of the material increases and thus more heat is needed to change per unit temperature. Ge_xSe_{100-x} system shows a wide glass-

forming region. Below are phase diagrams of Ge-Se, Ge-S and Ge-Te systems, indicating the glass-forming region [27].

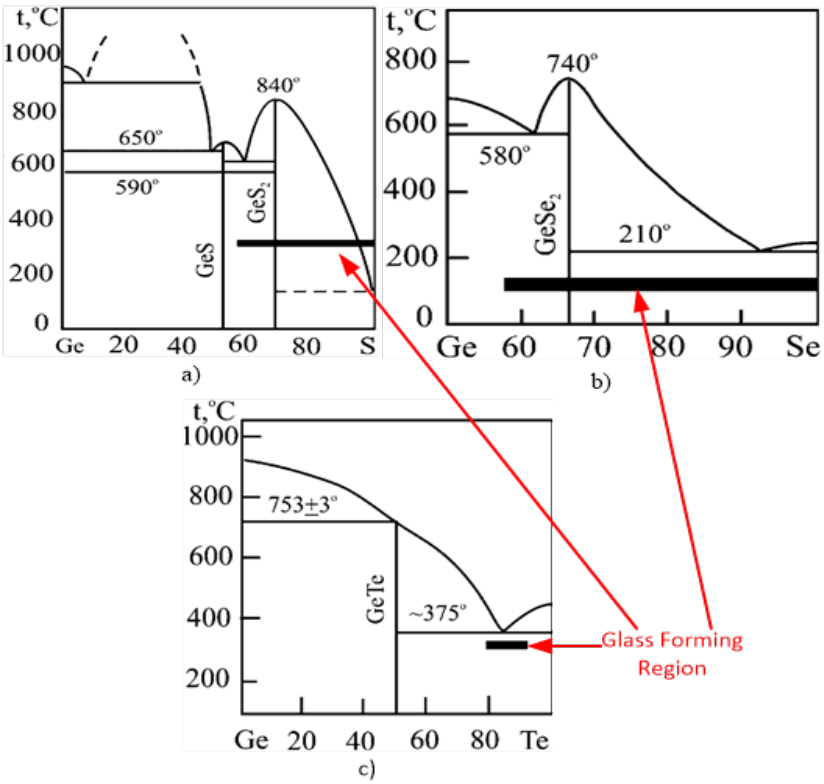

Figure 1.10 Phase diagram of Ge containing chalcogenide systems and glass forming regions (a) Ge-S (b) Ge-Se (c) Ge-Te [27].

Molecular Structure of Ge-Se (S) Glass Systems

The systems of interest are mainly built by Ge-Ch heteropolar and homopolar Ch-Ch or Ge-Ge bonds. The heteropolar bonding has priority to form. In the binary chalcogenide glass $Ge_xSe(S)_{100-x}$ system, at the stoichiometric composition (x =33), the system contains only heteropolar Ge-Se(S) bonds (if we consider it defect-free). For x < 33 and x > 33, the system contains not only heteropolar bonds but also homopolar Se-Se (S-S) and Ge-Ge bonds, respectively [42].

It has been proposed that $Ge_xSe(S)_{100-x}$ alloys can be described by chemically ordered clusters that are planted in a continuous network, such as corner-sharing tetrahedra $Ge(Se_{1/2})_4$, (Se)n chains and $Ge_2(Se_{1/2})_6$ ethane-like structural units. It is also suggested that the first two types dominate for x<=33 and the third type (which is much less deformable) is expected to occur on the Ge-rich side (x>33) [42].

Crystallization of Glasses

The crystallization process depends on internal energy and entropy of crystalline and amorphous states by Gibbs equation, G= H-TS [43]. Amorphous materials have no geometrical order, so the internal energy and enthalpy are larger than crystalline materials. The lower the Gibbs energy, the more spontaneous the crystallization process is. The glassy or amorphous state is metastable because the free energy of the system is above the minimum. The crystalline state has the lowest free energy and thus is a more stable state of the materials. In 1897, Ostwald explained the "step rule" [43]. Ostwald's rule of stages or Ostwald step rule states:

"When leaving a given state and in transforming to another state, the state which is sought out is not the thermodynamically stable one, but the state nearest in stability to the original state." [43]

The rule implies that the amorphous system changes gradually from lesser stable to most stable through intermediate steps. Depending on the composition of the material it is possible to get one or more crystalline structures through this process [44]. Crystallization is an exothermic process and in the DSC curve, it is presented through an exothermic peak. A typical DSC curve is shown in Figure 1.11. The y-axis heat flow is plotted as mW/mg and the exothermic peaks are presented in the down direction. This

mW/mg is a measurement of heat needed to increase per unit temperature of per mg of material. So, this curve is a measurement of the heat capacity of the sample at different temperatures. At T_g, the curve shows an endothermic step. At glass transition temperature, a transition from hard solid to more viscous material occurs. In this high viscous liquid, interatomic distance increases, which in turn makes the material softer. So, heat capacity increases, and more heat is needed to increase the temperature of the material with higher viscosity.

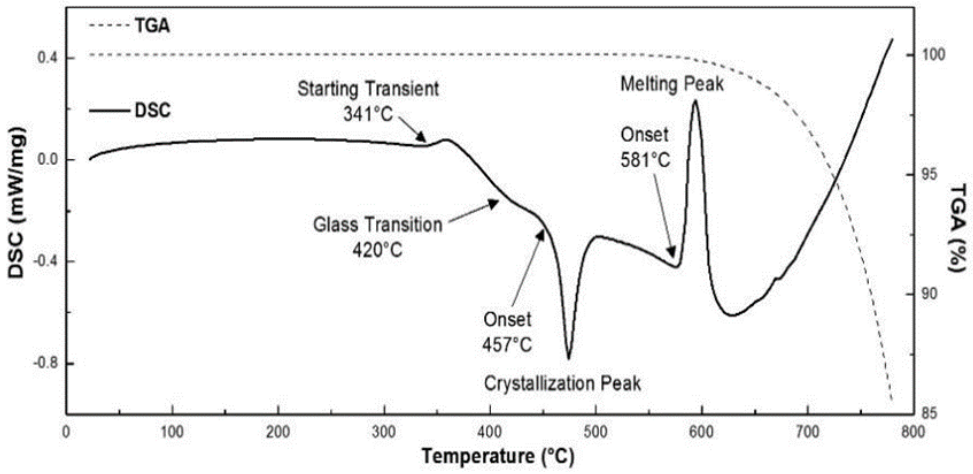

Figure 1.11 A typical DSC curve of $Ge_{20}Se_{80}$ (temperature vs. heat flow) showing glass transition T_g, crystallization temperature T_c, melting point T_m. Exothermic is downwards. This was done at BSU.

At onset T_o, the curve shows an exothermic peak. This is when the material starts to crystallize and transforms to its condition with the lowest entropy. Depending on the composition, bond reordering and new band formation can take place inside the material.

This amorphous to crystalline phase transition thus releases energy in the system and the signature of this effect is an exothermic peak. At T_m, the curve shows an endothermic peak. The supplied heat to the sample at that temperature goes to melting the material rather than increasing the temperature.

Crystallization happens in two-step processes; first, nucleation occurs, followed by a growth of the nuclei. The nucleation can be homogeneous or heterogeneous. Spontaneous nuclei formation in the melt is called Homogeneous nucleation. Nuclei formation on a pre-existing surface or interface of the material is called Heterogeneous nucleation [45], [46]. Nuclei formation depends upon whether the system can overcome the kinetic and thermodynamic barrier. To form a stable nucleus, the formation of that nucleus must reduce the system's free energy. This ensures overcoming the thermodynamic barrier. The size of the nucleus also plays a vital role. For a given temperature, the spontaneous formation of the nucleus has to be of a certain size called the "critical radius". This reduces the free energy and maintains stability. At lower temperatures, the critical radius reduces and makes stable nuclei formation more probable [45]. For homogenous nucleation, the change in Gibbs free energy is given by

$$\Delta \boldsymbol{G} = -\boldsymbol{V}(\Delta \boldsymbol{G_v}) + \boldsymbol{A\gamma} \quad \textbf{(1.2)}$$

V= Volume of crystal

A= Crystal/amorphous interfacial area

γ= Crystal/amorphous interfacial energy per area

$\Delta \mathbf{G_v}$= the difference between free energies per unit volume of crystal & amorphous

So, in the occurrence of small crystals, the positive surface energy term dominates and crystals dissolve again. For crystals having the critical radius and larger, the first term dominates, making the nuclei stable and growth happens. For homogeneous nucleation, **A** represents the interfacial area of crystals and amorphous materials. Crystal forms on an existing surface or interface (walls of the container, impurity particles) in the case of heterogeneous nucleation. Here, due to the formation of crystals on the surface, the

volume **V** could be the same, but the surface area **A** is less as the crystals are not perfectly spherical. So, the free energy is reduced.

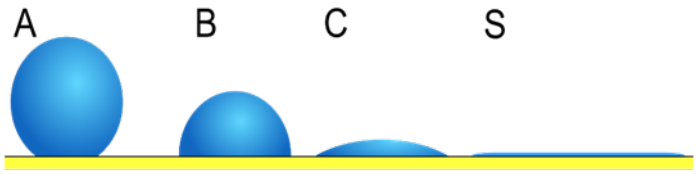

Figure 1.12 Heterogeneous crystallization [47]

As the nucleation rate is related to Gibbs free energy by the equation

$$R = R_c e^{\left(\frac{-\Delta G}{kT}\right)} \quad \textbf{(1.3)}$$

R= Rate of nucleation

K= Boltzmann constant

T= Temperature

$\mathbf{R_c}$= Rate constant

So, for the same critical radius heterogeneous nucleation can be exponentially faster than homogeneous nucleation. After nucleation comes growth, where the nucleus grows. More atoms are accumulating with the crystal. Considering v is the atomic jump frequency, the growth is calculated by the rate of atoms moving from amorphous to crystalline phases,

$$V_{a-c} = ve^{\left(\frac{-\Delta E}{kT}\right)} \quad \textbf{(1.4)}$$

and the rate of atoms moving from crystalline to amorphous phases,

$$V_{c-a} = ve^{\left(\frac{-\Delta E-\Delta G}{kT}\right)} \quad \textit{(1.5)}$$

So, the net crystal growth rate is,

$$U = a(V_{a-c} - V_{c-a}) \quad \textit{(1.6)}$$

a= The interatomic distance

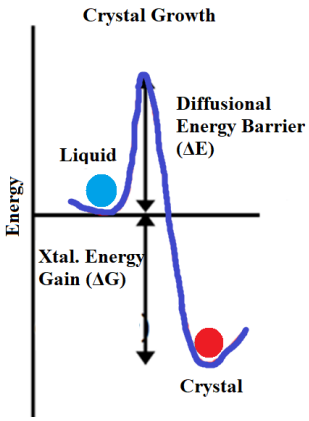

Figure 1.13 Crystal growth and energy diagram [45].

In the proposed devices, ChGs will be in contact with the waveguides, metal electrodes and probably an oxide layer on the surfaces. So, on the surface heterogeneous crystallization will occur. With a faster rate of nucleation, the crystallization process will be dominated by heterogeneous nucleation.

Radiation Hardness

Since the discovery of the semiconducting properties of chalcogenide glasses by Goryunova and Kolomiets [48], it was theorized that these glassy materials, owing to positional (topological) and compositional (chemical) disorders frozen near a glass transition temperature (T_g) during melt-quenching, would not incur any additional structural defects by the irradiation treatment that would change their physical properties [49]. This can be understood by studying their bond formation, structure and consequently band gap.

In Ge – containing glasses, the inclusion of Ge leads to the formation of variety of tetrahedral configurations in which the tetrahedra can be connected with their corners – forming corner-sharing (CS) building block. They can be connected through their edges, forming edge-sharing (ES) building blocks. When the Ge content is very high and there are not enough chalcogen atoms to satisfy its fourfold coordination, the occurrence of the

Ge-Ge bond is possible in the formation of an ethane-like structure or distorted rock salt structure. In addition to that, due to their amorphous nature, ChGs have numerous defects (dangling bonds) in their network.

Because of the amorphous structure of the material, these defects manifest themselves as "gap states" in the bandgap of ChGs [50], [51]. Near the center of the gap, the states are highly localized, so the electron exchange or hopping probability is low. It was proposed [52], [53] that in ChGs, these defect states are at dangling bonds D^0, and the lattice (not in the crystalline sense but the network) distortion is powerful enough to produce charged centers D^+ and D^- out of D^0. Moreover, the LPs form the upper portion of the valence band and D^+ interacts with the neighboring LPs and the interaction distorts the environment. Figure 1.14 represents the relation between network structure and band gap. Figure 1.15 demonstrates the relation between electronic states, carrier mobility and conductivity.

The localized states play a vital role in making the ChGs radiation hard and indifferent to doping up to some extent. These states behave like recombination centers and traps in the band gap. A high number of these traps contribute significantly to capture free carriers produced by ionizing radiation. So, it is difficult to move Fermi level (E_F) either by doping or by irradiation. This is the so-called "Fermi level pinning" phenomenon and is the main reason for all properties' stability of these materials by introducing impurity atoms in them.

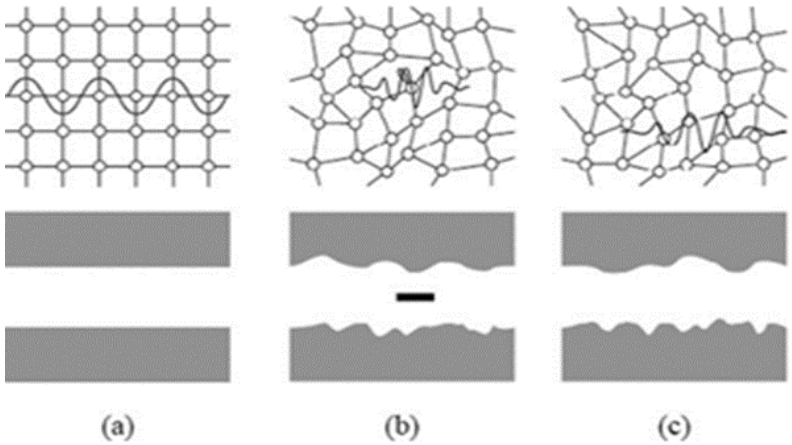

Figure 1.14 Electron wave functions and band structures in (a) an ideal crystal, (b) a disordered network with a dangling bond, and (c) a fully connected strained network [53].

In addition to that, the thermal neutron cross sections of naturally abundant Ge, Se and S are quite low (Ge 0.4, Se 0.61 and S 0.54 barn [7]). With the Fermi level locked at the center and low thermal neutron cross-section, it is expected that change in composition up to some extent produced by neutron capture and nuclear transmutation will not change the optical properties of the ChGs.

Besides the band gap argument, K. Tanaka developed a model according to which flipping of atoms can be achieved due to the interaction of the glass structure with the electromagnetic waves and the formation of electron-hole pairs. This, however, does not change the structure and consequently, the properties of the material stay the same [54]. According to this model, if two chalcogen atoms A and B belong to two neighboring chains between which Van der Waals force is acting, under irradiation, electron-hole pair forms. By this, atom A becomes charged and the force acting between atom A and B becomes Coulombic in nature and it forces atom A to a new position A'. At the availability of high density of the charged defects around the electron-hole pair, they

recombine and atom A remains in its new position A'. This, however, does not change the structure substantially and so the properties of the material stay unchanged.

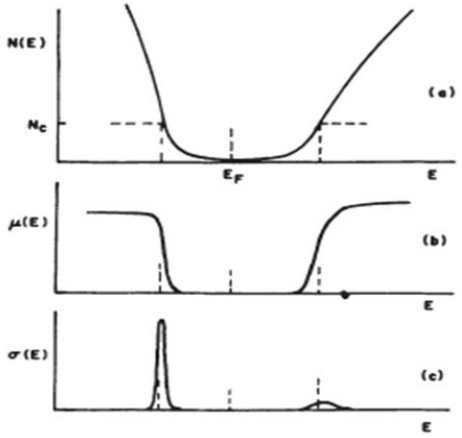

Figure 1.15 Model of an amorphous semiconducting alloy (e.g. ChGs). Schematically drawn as (a) function of electron energy are in a. the density of states N(E), (b) the mobility μ(E) of holes and electrons, respectively, and (c) the differential conductivity σ(E) [51].

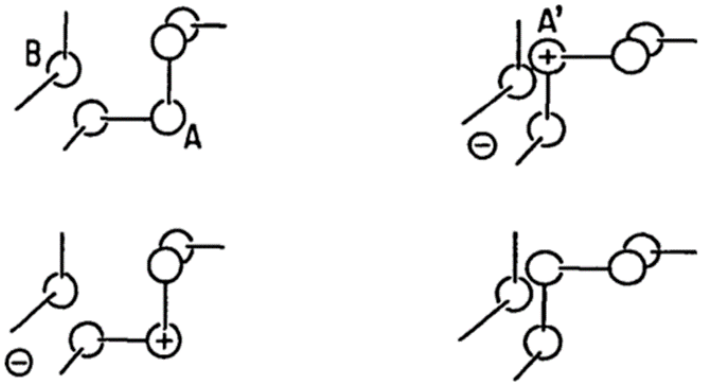

Figure 1.16 Bond twisting model [54].

As the number of e-h pairs increases, i.e., defect density increases, the recombination is faster. In other words, under radiation, at lower doses, there should be some measurable effects. However, with an increase of radiation, fluence/dose, there should be a region where the change of properties with radiation reaches saturation until

radiation-induced oxidation/ chemical change (gamma radiation), erosion (high DPA) and transmutation (high flux of thermal neutron) become dominant factors and change material property.

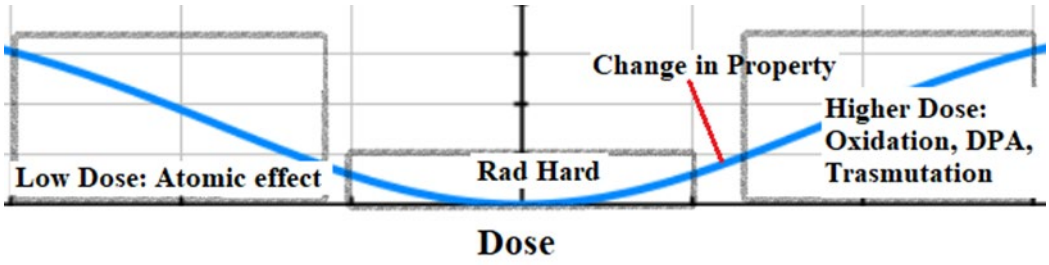

Figure 1.17 Dose vs. change in property in ChGs (sketch).

One other evidence of radiation hardness of ChGs has been reported by studying their thermal properties in DSC. DSC of the gamma-irradiated (gamma-quanta mean energy 1.25MeV, ^{60}Co source, temperature at 303 K, accumulated dose ~4, 8, 12, 24, 33kGy) $Se_{96}Sn_4$ showed that the onset of crystallization does not change [55]. It has also been demonstrated that the refractive index of $Ge_{22}As_{20}Se_{58}$ glass changes less than 1% after irradiation of up to 3 Mrad of gamma radiation dose [56]. Shpotyuk et al. reported that the transmission goes down in glassy As_2S_3 after gamma irradiation (dose 10MGy) and the change is partially reversible by annealing near the glass transition temperature [57]. Furthermore, Macko et al. reported (±3%) change in transmission in GeS_8 glass [58] after fast neutron irradiation (10^{16}-10^{19} n/cm^2) in the wavelength range 250-800 nm. As most of the chalcogenide glasses are transparent from 600 nm and beyond, further research is needed to elucidate the change in longer wavelengths, like 1310 or 1550 nm. Ovshinsky et al. reported that neutrons of 14 MeV, with a fluence of 10^{13} n/cm^2 do not change the threshold voltage of Ge-Ch based S-50 Ovonic Threshold Switches (OTS) [51]. Edmond, Male and Chester studied the influence of reactor irradiation, created by a

gamma-ray flux of 5×10^{13} MeV cm^{-2} s^{-1}, as well as fast and thermal neutron fluxes of 3×10^{13} cm^{-2} s^{-1}, on electrical properties of liquid semiconductors in the mixed As–S–Se–Te–Ge system. They report that no changes were detected even at the fast neutron doses up to 1.8×10^{20} cm^{-2}. But it remained unclear whether this irradiation did not produce significant damage or that high-temperature thermal heating (at more than 470 K) was enough to anneal any damage [59]. One of the most interesting revelations comes from the works of Sarsembinov and his group [60]. They irradiated thermally evaporated thin films of Ge_2S_3 with 2MeV electrons and an integrated flux of $10^{17}e/cm^2$. The thin films showed a reduction in transmission and a shift in the short wavelength edge of the transmission spectrum (wavelength: 600nm-800nm) after irradiation. But after annealing the thin film for 10 hours at 433K in a vacuum 10^{-3} torr, the change was completely reversible. One of the reasons behind the radiation hardness of Ge-containing glasses compared to arsenic is that Ge has higher coordination than arsenic. Ge forms 4 bonds with neighboring chalcogen elements, whereas As forms 3 bonds, it requires less energy to displace As atoms than Ge.

The study also found that As_2Se_3 is the least responsive to neutron radiation and only a small (<5nm) shift towards a higher wavelength was reported. Self-restoration, annealing to reverse radiation impact and Fermi level pinning are the major properties making the ChG family an important candidate for devices working in a radiation environment. All mentioned data lead to conclusion that one could expect stable device performance while individual films could undergo some structural changes.

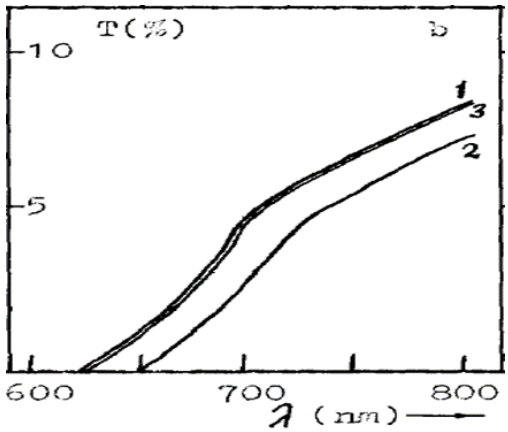

Figure 1.20 Spectral dependencies of %transmission in Ge_2S_3 before (1) and after (2) Irradiation and after annealing the (3) [60].

From the theories and literature review, it seems non-stochiometric Ge-S and Ge-Se glasses are good starting compositions to study for temperature sensing material for our specific application.

Dissertation Outline

Chapter 1: This chapter describes the motivation for this work along with the introduction to chalcogenide glasses and crystallization kinetics.

Chapter 2: This chapter describes the experimental methods that are used in this work.

Chapter 3: A study of crystallization kinetics and its relationship with the optical properties of Ge-Se chalcogenide glasses are presented in chapter 3. This chapter is a crucial step towards selecting compatible materials for the specific applications. This is a comprehensive study to understand the performance and limitation of the materials. This chapter is based on the following published papers

a. Sakaguchi, Y., Hanashima, T., Ohara, K., **Simon, Al-Amin A**., Mitkova, M., Structural transformation in Ge_xS_{100-x} ($10 \leq x \leq 40$) network glasses: Structural varieties in short-range, medium-range, and nanoscopic scale.

Phys. Rev. Materials **3**, 035601. (2019) https://doi.org/10.1103/PhysRevMaterials.3.035601

b. **Ahmed Simon, AA**., Badamchi, B., Subbaraman, H. et al. Phase change in Ge–Se chalcogenide glasses and its implications on optical temperature-sensing devices. *J Mater Sci: Mater Electron* 31, 11211–11226 (2020). https://doi.org/10.1007/s10854-020-03669-0

Chapter 4: Since the fabricated devices must perform under irradiation, an extensive study of the materials under Xe ion irradiation is performed. This study is essential towards understanding the reliability of the devices under irradiation. Chapter 4 elucidates effect of ion irradiation on the crystalline structure of Ge-Se glasses and provides a complete guideline on how to test materials and devices for radiation hardness. It is based on the following publication:

Ahmed Simon, A., Jones, L., Sakaguchi, Y., Kunold, H., van Rooyen, I. and Mitkova, M. (2021), Effect of Ion Irradiation on Amorphous and Crystalline Ge–Se and Their Application as Phase Change Temperature Sensor. *Phys. Status Solidi B* 2000429. https://doi.org/10.1002/pssb.202000429

Chapter 5: This chapter deals with the additive manufacturing of chalcogenide glass. Nanoparticles formation, inks preparation, characterization of the ink, inkjet printing and dip coating of chalcogenide glasses are described in this chapter. Raman spectroscopy, XRD and EDS data of the printed films are compared with the respective data of the thermally evaporated films. This chapter is based on the below mentioned papers

a) **Ahmed Simon, A.**, B. Badamchi, Jones, L., Kunold, H., van Rooyen, I., Sakaguchi, Y., H. Subbaraman and Mitkova, M. (2021), Introduction of

Chalcogenide Glasses to Additive Manufacturing - Nanoparticle Ink Formulation, Inkjet Printing, and Phase Change Device Fabrication*, Scientic Reports (Under Review)*

b) **Ahmed Simon, A**., Rahmot Ullah, S., Badamchi, B., Subbaraman, H., & Mitkova, M. (2019). Materials Characterization of Thin Films Printed with Ge20Se80 Ink. Microscopy and Microanalysis, *25*(S2), 2606-2607. doi:10.1017/S143192761901376X

Chapter 6: This chapter describes the devices and their performance. Thermally evaporated, printed and dip-coated devices are tested. An array of fiber devices is tested to show the real-time performance of the devices. Parts of this chapter are based on below-mentioned papers

a. **Ahmed Simon, A.**, Jones, L., Sakaguchi, Y., Kunold, H., van Rooyen, I. and Mitkova, M. (2021), Effect of Ion Irradiation on Amorphous and Crystalline Ge–Se and Their Application as Phase Change Temperature Sensor. *Phys. Status Solidi B* 2000429. https://doi.org/10.1002/pssb.202000429

b. B. Badamchi, **A.-A. A. Simon**, M. Mitkova, and H. Subbaraman, "Chalcogenide Glass-Capped Fiber-Optic Sensor for Real-Time Temperature Monitoring in Extreme Environments," *Sensors*, vol. 21, no. 5, p. 1616, Feb. 2021.

Chapter 7: A summary and conclusion of the work is presented in this chapter.

CHAPTER TWO: EXPERIMENTAL

Glass Synthesis

The bulk chalcogenide glasses were synthesized by the standard melt quenching technique. Pure 5N elements were weighed accurately and the required amount was loaded into a fused silica ampule and then sealed under vacuum (~10^{-4} mbar). The glass synthesis was carried out in a programmable tube furnace for 168 hours (one week) at the peak temperature of 750°C. The furnace was programmed (at different rates, depending upon the composition) to reach 750°C within the first 24 hours of synthesis. The ampules were kept at the highest temperature for 144 hours. There was an important reason for the long duration of the synthesis – good glass homogenization. Usually, it is assumed that holding the glass melt at a temperature 20-50°C above the highest melting phase temperature for several hours would homogenize the melt. However, at equilibrium presented in the phase diagrams, glass-forming compositions are usually bordered by congruently melting crystalline phases [61], which can nucleate as melts are quenched to produce microscopic heterogeneities [62]. The continued reaction leads to these crystalline phases to dissolve and local structures characteristic of melts/glasses to emerge [62]. Avoiding the formation of microscopic heterogeneities leads to slow aging of the glasses, which is a warranty for the stability of their parameters, the structure/composition of the films produced from them, and particularly their crystallization temperature.

Thin Film Preparation-Thermal Evaporation

The ChGs and Aluminum were evaporated on silicon substrates in a Cressington 308R thermal evaporation system at 10^{-6} mbar pressure, using a semi Knudsen cell crucible. The thickness of the films was in the range of 100-200 nm. A quartz crystal microbalance was used to estimate the thickness of the films *in situ*. For device preparation, the evaporation was done on oxidized (SiO_2 thickness 100-150 nm) Si wafer or optical fiber tip. For material characterization, evaporation was done on single crystalline Si (100) substrate. A hard mask was used during Aluminum evaporation for electrodes.

Ball Milling

The ink formation starts with wet milling of ChG. Before milling, the bulk glasses were crushed into smaller particles by agate mortar. For wet milling, 14g of ChG, 3g of ethylcellulose and 50ml of cyclohexanone were mixed and were introduced into the milling jar. The ball mill is not built for continuous production, so it was programmed to mill for 30 min, then a 30 min pause and repeat. It has the provision to control the temperature during milling. Using that, temperature was kept below 50°C. Milling of ChG was done with 2 mm stainless milling balls. Retsch High Energy Ball Mill Emax was used for ball milling. It is a state-of-the-art milling system that can mill at 300-2000 rpm and produce nanoparticles < 80 nm. It is programmable, and at a time, two different materials can be milled. The milling rpm was set at 1100 rpm after optimizing by trial and error.

Ultrasonication

For ultrasonication, a QSONICA ultrasonicator (500W) was used. The ultrasonicator's electronic generator transforms AC line power to a 20kHz signal that drives a piezoelectric transducer. The vibration is then amplified, which transmits down the length of a probe. The tip submerged into the sample expands and contracts. Due to the rapid vibration of the tip, it causes cavitation, the formation and collapse of minuscule bubbles in the liquid. The breakdown of thousands of bubbles releases tremendous energy in the liquid. Objects and surfaces within the liquid are thus "processed". The probe tip diameter dictates the amount of sample that can be effectively processed. Smaller tip diameters (Microtip probes) deliver high-intensity sonication, but the energy is focused within a small, concentrated area. Larger tip diameters can process larger volumes. The ink test tube was put in an ice bath during ultrasonication to prevent heating of the sample. The sonicator parameters were ON/OFF time = 2 sec/4 sec at 50% power.

Centrifugation

For centrifugation, a Thermofisher centrifuge system was used at 4500 rpm (maximum) for 1-2 hours. It should be stated that when a mixture is placed inside the centrifuge slot, an approximately equally weighted test tube filled with water or any inert material must be placed in precisely the opposite slot of the mixture. It is required to keep balance and stable centrifugation.

DLS

NanoBrook Omni DLS utilizes light scattering to measure particle size. For the experiment, pure cyclohexanone was poured in a vendor-recommended glass cuvette.

Then only a tiny drop of ink was dropped and mixed with the cyclohexanone. DLS needs the light to pass through the cuvette, so it is necessary to use a dust-free cuvette and the amount of ink should be as low as possible.

Viscosity

A Brookfield AMETEK DV3T Rheometer was used to measure the viscosity of the inks. For final adjustment of the ink viscosity, cyclohexanone and ethylcellulose were added to the milled mixture to prepare a compatible ink. The optimal concentration was found to be 0.15-0.3 g/ml chalcogenide glass and 0.03-0.05g/ml ethylcellulose in cyclohexanone. The viscosity of the prepared inks was measured and was found to be 10-12 cP, which satisfies the requirements of the DMP-2850 printer.

Contact Angle

The contact angle of the ink on oxidized silicon was measured using an Attention tensiometer. All three ChG compositions showed contact angle 10-15°, which is suitable for surface wettability. For improvement of the adhesion, the substrate was plasma cleaned.

Dip-coating

The fiber-tips were dipped in ink under vacuum at room temperature. After 24 hours, the tips were carefully taken out of the ink. Then the tips were further cured using a hot chuck in a two-step process: (1) the coated fiber was heated at 50 °C for 2 h to slowly dry the solvent, cyclohexanone, without creating cracks in the film, and (2) the fiber tips were placed in a tube furnace heated at 350 °C for 1 hour to decompose the surfactants in ink, ethylcellulose. Once cooled, the fiber tip was dip-coated with spin-on-glass for isolation of the tip from an oxygen-containing ambient. After drying at room

temperature for 24 hours, the coated fiber was heated at 300 °C for 3 hours to cure the spin-on-glass.

Thin Film Preparation- Inkjet Printing

ChG layer was printed using a Fujifilm DMP-2800 Dimatix inkjet printer. AutoCAD and LibreCAD were used to design printing patterns. The cartridge parameters had to be optimized to have uniform drop speed from the enabled nozzles. In the DMP-2850 printer, the printing was done using 3-5 nozzles. Nozzle voltage was between 20-30 volts. The drop separation was set at 20µm. Under such conditions, 100µm resolution was achieved. For characterization, 10 layers of 5cm x 5cm thin films were printed.

Electrode Printing- Screen Printing

Nickel electrodes were printed on top of oxidized films and ChG layer using an SPM 7189 screen-printer.

Thin Film Sintering

After printing, the printed films are wet, and the nanoparticles are mixed with the surfactant. The printed films were dried for two days in a vacuum chamber at room temperature for the initial slow solvent evaporation to avoid crack formation. Once dry, the thin films were annealed in an inert atmosphere at 350°C (the decomposition temperature of ethylcellulose) for 2-3 hours. During this time, the particles are sintered and the features are hardened to form solid printed films.

Annealing of the Thin Films & Ellipsometry

The evaporated thin films were heated in a specially designed hot stage THMSEL600 by Linkam Scientific, which is compatible with J. A. Wollam's M-2000 Ellipsometer for *in situ* measurement. The stage was purged with nitrogen gas to create

an inert environment. The thin films were heated at a rate of 10 K/min and while they are being heated, ellipsometric data (psi, ψ and delta, Δ at wavelength: 600 nm to 1688 nm) were obtained at an incident angle of 70°. Then the thin films were cooled in the same system under nitrogen flow. Measured data were analyzed and modeled in *CompleteEASE*, a modeling tool that comes with M-2000 to get refractive indices (n) and extinction coefficients (k).

Differential Scanning Calorimetry (DSC) of the Bulk Glasses

The crystallization temperatures of the bulk glasses were obtained by differential scanning calorimetry (DSC) on a Netzsch STA 449 F5 Jupiter® DSC/TG machine in alumina (Al_2O_3) crucibles under 20ml/min nitrogen flow at the following heating rates: 10K/min; 15K/min; 20K/min; 25K/min; 30K/min.

High Energy XRD

The high-energy x-ray diffraction experiments were carried out at the bending magnet beamline BL04B2 [63] of SPring-8 with a two-axis diffractometer for disordered materials [63]. The incident photon energy of 61.7 keV, obtained from a bent Si (220) crystal, was used for the experiment. The measurements were performed in transmission geometry. The intensity of the incident x-ray was monitored by an ionization chamber filled with Ar gas and the scattered x rays were detected by a CdTe solid-state detector. The collected data sets were corrected for the absorption, the background, and the polarization. Details of the data correction and the normalization procedures are given in [64].

X-ray Diffraction (XRD)

XRD was employed to investigate the crystalline phases of the annealed thin films, and the measurement was conducted on a Rigaku MiniFlex600 (λ=1.5406Å) at 40 kV and 15 mA. The data were collected in a range of 2θ = 10–90° by a scanning rate of 10°/min at room temperature.

Raman Spectroscopy

Raman analysis was performed to identify any changes in the bonding and physical structure of the materials occurring during crystallization. Raman studies were performed with Horiba Jobin Yvon T64000 Raman Spectroscopic System in backscattering mode, using a parallel-polarized 442 nm He-Cd laser, focused to a spot of 100 μm, with a power of 85 mW. The samples were placed in a chamber and brought to a 10^{-3} mTorr vacuum and temperature of 100 K. The low power, vacuum and temperature prevent the occurrence of photoinduced effects caused by the laser light, which is within the absorption edge of some of the materials.

Energy Dispersive Spectroscopy (EDS)

Energy Dispersive Spectroscopy (EDS), used to confirm the exact composition of the produced films, was conducted using an FEI Teneo Scanning Electron Microscope (SEM) with an Oxford Instruments Energy + EDS system. A line scan of each sample was done at a length of 1500μm for the collection of an accurate average value and the standard deviation.

Atomic Force Microscopy

Surface roughness was characterized via atomic force microscopy (AFM) using a Bruker Dimension FastScan system operating in PeakForce Tapping mode. A ScanAsyst-

Air probe with a nominal 2 nm radius of curvature and a 0.4 N/m spring constant was used to capture a pair of 5 μm x 5 μm topography images at two different locations on each sample surface. The raw images were then processed with a first-order XY plane fit to remove sample tip and tilt using Bruker's NanoScope Analysis software package (Version 2.0) before calculating the root mean square (RMS) surface roughness data presented here.

Electronic Device Characterization

The devices were characterized with a semiconductor parametric analyzer (Agilent 4155B). I-V characteristics were measured from 0-3 V at a resolution of 30mV/step. To achieve phase change of initially amorphous active material, the devices were kept for 15 sec at each temperature, including the onset of crystallization temperature. Crystallized devices were pulsed with a Pulse Generating Unit (PGU) at different duration for amorphization with square wave amplitude 10-15V, period 7μs, and ON time: 50-80ns.

Thin Film Fiber Tip Temperature Sensors Preparation and Characterization

The ChG thin films on the tip of the fibers were prepared by thermal evaporation in a Cressington 308R coating system at 10^{-6} mbar vacuum at evaporation rate 0.3Å/s. The fibers were not specifically heated during the film preparation. The thickness of the deposition on the fiber tips was estimated using the output from a quartz crystal microbalance. Their composition was studied with Energy Dispersive Spectroscopy.

Optical Fiber Device Characterization

The fabricated sensor devices' performance was characterized by injecting a 1550 nm wavelength light from a tunable laser source into the fiber sensor through a circulator.

The light power reflected from the fiber sensor was analyzed using an optical spectrum analyzer (Anritsu MS9740A). The ChG-capped fiber tip itself was placed inside a high temperature-controlled tube furnace (Eurotherm 2116 controller). The furnace temperature was increased from room temperature (~25 °C) and 650 °C in 10 °C/min steps. For evaluation of the sensor's real-time response, the temperature inside the furnace as a function of the time was tracked as well.

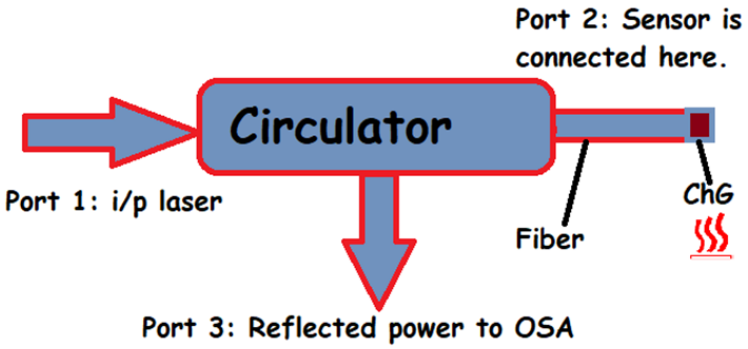

Figure 2.1 Schematic of fiber-tip based sensor testing.

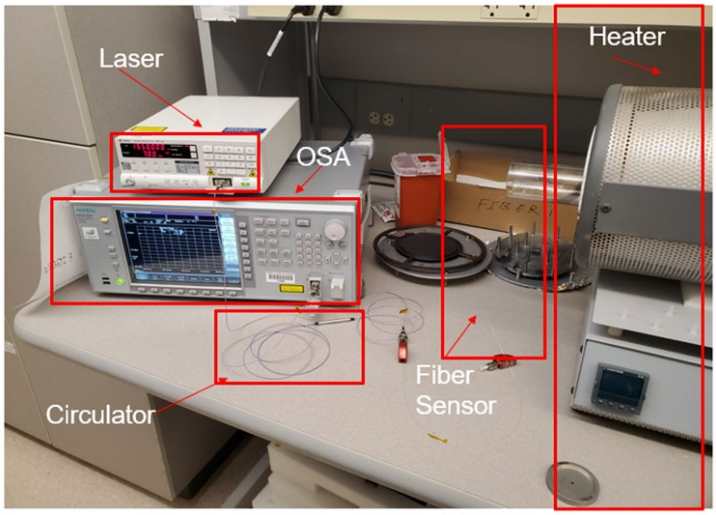

Figure 2.2 Experimental setup for fiber-tip based sensor testing.

The reflected data was normalized with a blank fiber data at the same temperatures to extract the effect of the ChG alone.

Ion Irradiation

ChG thin films were irradiated with xenon (Xe^{+}) with three different energies 100, 200, 600, 500, 700, 1000 keV and fluence $10^{14}cm^{-2}$. The total effect of the non-ionizing radiation is 5 and 10 displacement per atom (DPA). A detailed calculation is added in Appendix B.

Plasmonic Device Characterization

The lensed optical fiber focuses the incoming light to the waveguide end-facet. The lensed fiber reduces the beam spot size to 2-3 µm at which the mode field size of the SMF is about 8µm. Another lensed fiber is used as a detector fiber at output stage to collect the transmitted power at the output. The output power can be measured using power meter or OSA. Fiber tip and waveguide edge under microscope are precisely aligned using piezo controller and stepper motors. The waveguides are placed in a hot stage to measure real time effect of the temperature.

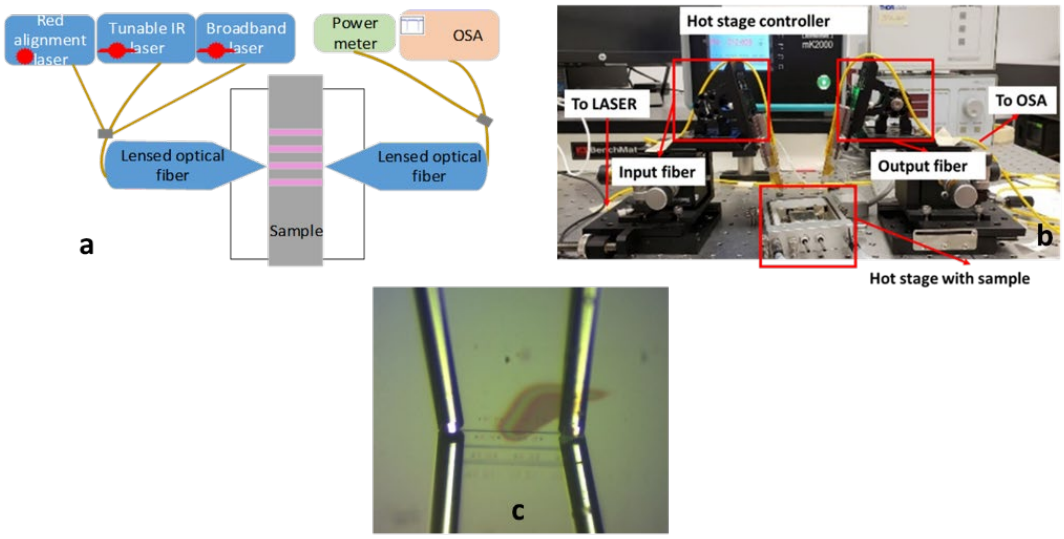

Figure 2.3 a) Plasmonic sensor testing schematic, b) Experimental setup and c) Device testing.

CHAPTER THREE: STRUCTURE, OPTICAL PROPERTIES AND CRYSTALLIZATION KINETICS OF CHALCOGENIDE GLASSES

The application of chalcogenide glasses for phase change memory devices was the first sign of the vast functionality potential which these materials offer [65]. Later chalcogenide glasses were applied for phase change optical media storage [28], inorganic photoresists [66], and programmable metallization cell memory, also called CBRAM [67], to name a few. The studies related to these applications revealed that the significant flexibility of the chalcogenide glass structure is based on the availability of lone pair electrons [68] on the chalcogen atoms and their low coordination [69]. The chalcogenide glasses can be formed with stoichiometric compositions and a continuous variety of compositions maintaining the short-range order and the chemical valence states requirements of the participating atoms [70] without the existence of the medium and long-range order. This leads to the formation of several structural building blocks, including the chalcogen elements and the other participating atoms [71], which makes the structure three-dimensional. All structural units have well-established and extensively studied Raman signatures [72], [73], which allow detailed structural characterization of the investigated materials. The other methods used to characterize the structure of the studied materials are high energy x-ray diffraction, x-ray diffraction spectroscopy and the crystallization kinetics of the studied glasses have been investigated using Differential Scanning Calorimetry (DSC). The results of these studies are presented in this chapter, starting with details of the molecular structure, followed by the data related to the

crystallization kinetics and the structural characterization of the initial amorphous phases and the crystals formed after they have been crystallized.

Selenium-rich $Ge_{30}Se_{70}$, stoichiometric $Ge_{33}Se_{67}$ and Ge-rich $Ge_{40}Se_{60}$ are studied since, to the best of our knowledge, we could not find well-established data for their crystallization kinetics and glass crystallization temperature. Non-isothermal glass crystallization analysis has been conducted in which the bulk sample is heated from room temperature at a fixed rate and the heat flow is recorded as a function of temperature. For sensor calibration purposes using Differential Scanning Calorimetry (DSC), T_g, T_o and T_c were obtained at five different heating rates and the data have been used to calculate the crystallization activation energy. The dependence of the refractive index and the extinction coefficients as a function of temperature are measured using hot stage assisted ellipsometry. Raman spectroscopy revealed the crystal formation out of the disordered glass matrices, and the molecular composition and structure of the crystalline phases are studied with X-ray diffraction (XRD).

To understand the molecular structure of the chalcogenide glass, precise x-ray diffraction measurements using high-energy x-rays of synchrotron radiation were carried out for Ge_xS_{100-x} ($10 \leq x \leq 40$) network glasses. An excerpt from our peer-reviewed journal discussing the results is presented here to describe the molecular structure of Ge-S glasses, which is analogous to the structure of Ge-Se glasses. Moreover, the collection and modeling of ellipsometry data from thin film ellipsometry of ChGs are also described in Appendix A.

Structure of Ge-S(Se) Chalcogenide Glass

Among various amorphous chalcogenides, Ge-S (Se) glassy binary alloy is one of the most studied materials because of its simplicity, in which the system is composed of only two elements and its structural variations. The Ge-S (Se) system has a good glass-forming ability in a wide composition range [74], [75]. The network structure is built up by fourfold-coordinated Ge atoms and twofold-coordinated S (Se) atoms. The nature of the network is considered to change with increasing Ge or S (Se) content. Phillips [30] regarded the number of constraints per atom, NCO, and provided the optimum concentration for glass-forming ability in the Ge_xSe_{1-x} system as $x = 1/6$. The network is under constraint for $x < 1/6$, while it is over constraint for $x > 1/6$. At $x = 1/6$, the mean coordination r should be $r_p = 2.33$. Thorpe [33] referred to $x < 1/6$ as a "floppy" region in which the network is like a polymeric glass, while he referred to $x > 1/6$ as "rigid," in which the network is like an amorphous solid. There should be a rigidity percolation (RP) transition in the system. After 17 years from their suggestions, Thorpe and Phillips and their related researchers, more specifically Boolchand, pointed out that there can also be a narrow third region around RP, what they call the "intermediate phase," where the network is rigid, but stress-free [34], [36], [76]–[78]. Overall, these possibilities indicate varieties in the network system in Ge-S(Se) alloys.

So far, the microscopic "molecular-like" structure in the glassy Ge-S(Se) system has been mainly investigated by Raman spectroscopy. At $x = 0.33$ [$GeS(Se)_2$], there are $GeS(Se)_{4/2}$ tetrahedral units which also exist in $GeS(Se)_2$ crystal. The presence of the units is confirmed by the Raman peak, assigned to the breathing mode of methanelike $GeS(Se)_{4/2}$ molecules (for corner-sharing tetrahedra) [79], [80]. SiO_2 glasses have only

such corner-sharing tetrahedra $SiO_{4/2}$. However, Ge-S(Se) glasses also have edge-sharing tetrahedra. Furthermore, Ge-S(Se) glasses can have homopolar Ge-Ge and S-S (Se-Se) bonds, whereas SiO_2 glasses have only Si-O heteropolar bonds. In the Raman spectra, the Ge-Ge bonds can be found from the vibrational mode of $S(Se)_3$-Ge-Ge-$S(Se)_3$ ethane-like unit [81]. The diffraction study can provide important information on the local and the medium-range structure. Systematic x-ray diffraction measurements were performed by Fueki et al. for $10 \leq x \leq 40$ [82]. However, the measured Q range was limited up to 13.5 $Å^{-1}$ because of the used x-ray source generated by the Mo target. Detailed discussion on the pair distribution functions would be difficult due to the limitation of the Q range. In recent years, excellent works have been done on the structure of Ge-S binary glasses using synchrotron radiations and neutron sources for the S-rich glasses by Bychkov et al. [83] and for the Ge-rich glasses by Bytchkov et al. [84]. However, the analysis has not been done in a unified way through the whole glass-forming range, including S-rich and Ge-rich regions. For this, we performed precise measurements of x-ray diffraction of Ge-S binary glasses for a wide Ge-composition region, $10 \leq x \leq 40$, using the synchrotron radiation at SPring-8 and compare the result with systematically measured Raman spectra. Based on the results, we have discussed the structural variations in the glasses in terms of the shortrange, medium-range, and nanoscopic orders, and explain the composition dependence of the physical properties of Ge-S glasses. In these glasses, S_8 ring molecules are embedded in the network and can assemble to form crystals. This would be the biggest difference compared to the Ge-Se system.

Figure 3.1 shows the pair distribution functions of Ge_xS_{100-x} (x = 10, 20, 30, 33, 40) glasses. The peaks in the pair distribution functions are compared to the interatomic

distances in the crystals with the stoichiometric compositions (x = 0, 33, and 50): α-sulfur [85], the high-temperature phase of GeS_2 crystal [86], and GeS crystal [87]–[90]. The S-S bond length in an S_8 ring in α-sulfur is 2.06 Å [85]. The Ge-S bond length in the GeS_4 tetrahedral unit in the high-temperature phase of GeS_2 crystal is 2.22 Å [86]. The Ge-S bond length in the GeS crystal is 2.44 Å [88], [90]. The first peaks, ranging from 1.8 to 2.8 Å, are attributed to these bonds. In $Ge_{30}S_{70}$ and $Ge_{33}S_{67}$, there is a small peak at 2.9 Å. This indicates the Ge-Ge distance in the edge-sharing tetrahedra (2.91 Å) [91].

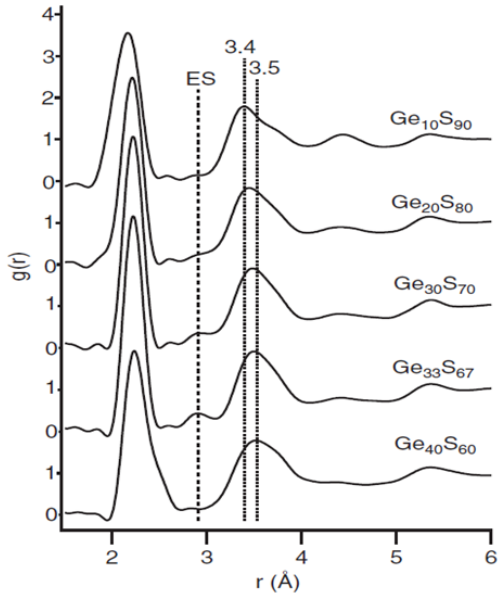

Figure 3.1 Pair distribution functions of Ge_xS_{100-x} (x = 10, 20, 30, 33, 40) glasses. The broken line, indicated by "ES," shows the position where the peak associated with the Ge-Ge distance between two neighboring edge-sharing GeS_4 tetrahedra, at 2.9 Å [92].

The second peak, ranging from 3.1 to 4.0 Å, can be related to several types of inter-atomic distances. The second-neighbor S-S distance in S_8 ring molecules is estimated to be 3.34 Å, according to the bond length and the bond angle [85]. Even when an S_8 ring molecule opens to a helical chain, the second neighbor distance can be preserved. The atomic correlations can contribute to the second peak in S-rich Ge-S

glasses. The distance between neighboring S atoms in GeS_4 tetrahedron is estimated to be 3.62 Å, according to the bond length and the bond angle [86]. The Ge-Ge distance in corner-sharing tetrahedra is 3.41 Å, according to the simulations of glassy GeS_2 [91]. These atomic correlations impact on the second peak for all Ge compositions. Overall, the local structure obtained from the pair distribution functions is consistent with the previous picture on the structural transformation of molecular-like units, established by Raman spectroscopy [79], [93].

Next, we will discuss the crystallization of the glasses with their optical properties. A description of ellipsometry modeling and data collection to obtain optical properties are described in Appendix A. Our contribution in this aspect is establishing the changes of the optical properties caused by increasing the temperature of the materials and their crystallization.

Crystallization Kinetics, Crystalline Phase and Optical Properties of Chalcogenide Glasses

A detailed study was done to study the crystallization kinetics of Ge-Se glasses, their crystalline phase, and optical properties. Two major characteristics of chalcogenide glasses are their glass transition temperature (T_g) and the peak crystallization temperature (T_c). T_g is related to the onset of fluidity, i.e., by reaching this temperature, the glass overcomes the cohesive forces, which give the glass its solid-state condition. In other words, at this temperature, the network is destroyed up to some extent and the building blocks are macroscopically mobile. Consequently, while searching for material with high T_g one must look for materials with high coordination number and high bond or cohesive energy between the elements of the glass. Based on the Vogel-Fulcher correlation related

to viscosity, De Neufville et al. [94] gave a mathematical equation of these dependencies accordingly to which

$$\boldsymbol{T_g = T_0 + \frac{\delta(<CN>-2)E_g}{32.2k_B}} \quad \textbf{(3.1)}$$

Where 32.2 = ln($m(T_g)/m_0$). The T_0 and δ are system-related parameters and m is the viscosity for which the authors assume that it has a fixed value of m(T_g) ~10^{13} Poise [95]. Although T_g usually shows proportional dependence upon the coordination of the glasses and covalent bond strength, other factors like connectivity and degree of polymerization relate to the formation of flexible or rigid phases, which are involved in the process of glass transition and crystallization. With the increase of coordination with enriching the composition with Ge, T_g rises and goes very close to the crystallization temperature of the material. Hence, a decrease in glass-forming ability (K_{gl}) and thermal stability of the glasses is seen since they depend upon the onset of crystallization T_o, T_g and glass melting temperature T_m [96].

$$\boldsymbol{k_g = \frac{T_o - T_g}{T_m - T_o}} \quad \textbf{(3.2)}$$

Results

The DSC curves of the three studied compositions are shown in Figure 3.2 (a-c). In these graphs, the T_g is defined as the first point of inflection of the low-temperature endotherms. T_c is the exothermic peak and T_o is the onset of crystallization. For further considerations, the heating rate of 10°C/min is accepted as a standard heating rate and all individual data like Raman spectra, XRD data, etc., are obtained from samples heated at 10°C/min. As can be seen, the T_g, T_o and T_c of the three compositions are pretty much different. The maximum value of T_g, T_o and T_c is found for the stoichiometric

composition and lower values were obtained for $Ge_{30}Se_{70}$ and $Ge_{40}Se_{60}$. All these data are presented in Appendix A, Table A.1.

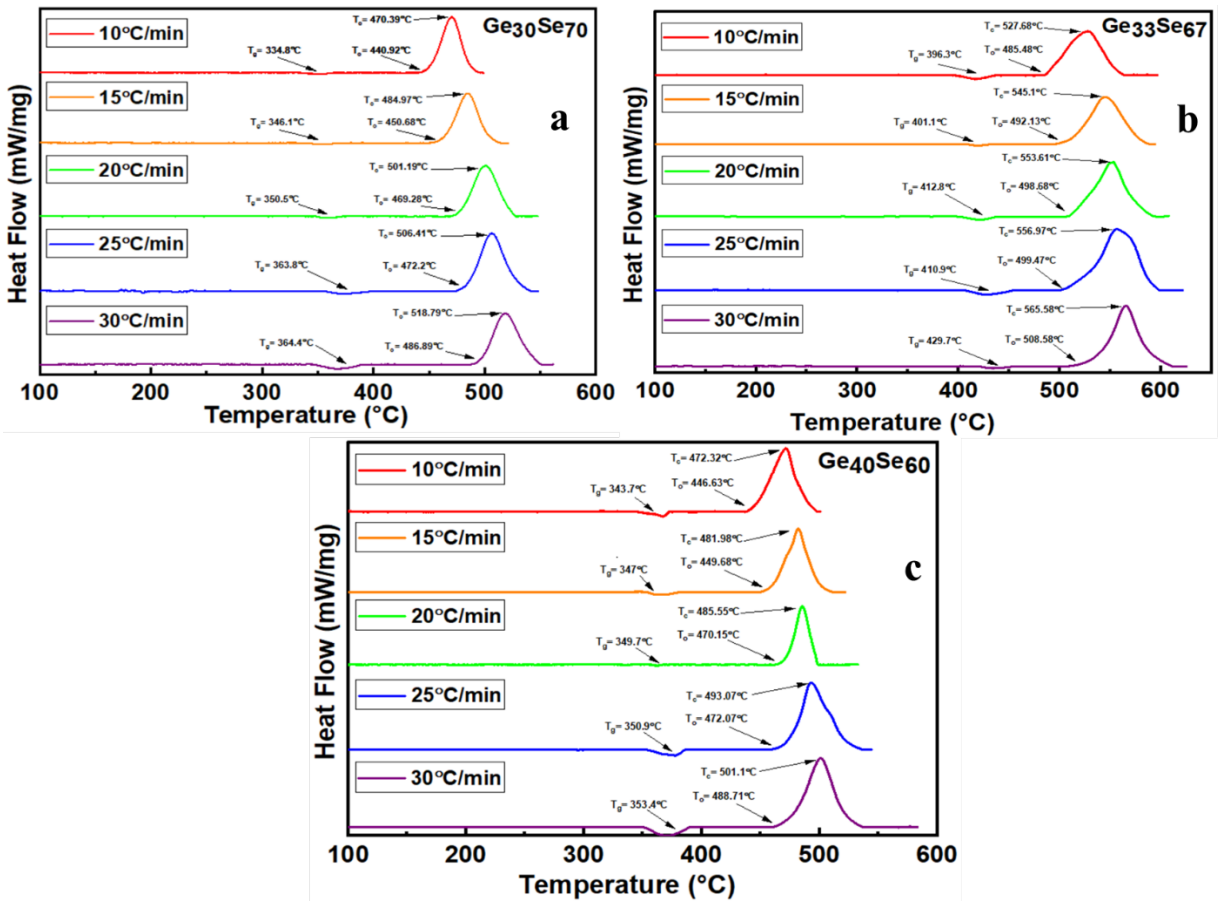

Figure 3.2 DSC curves for Ge_xSe_{100-x} at different heating rates; a) $Ge_{30}Se_{70}$; b) $Ge_{33}Se_{67}$; c) $Ge_{40}Se_{60}$

The data summarizing the characteristic temperatures of the materials as a function of the heating rate are presented in Figure 3.3. They demonstrate that in general, all these data are depending upon the heating rate, excluding T_g of the $Ge_{40}Se_{60}$ samples, which is less reliant on the heating rate compared to the T_g of the two other compositions.

The structural data for the synthesized glasses and their crystalline counterparts, obtained through Raman spectroscopy, are shown in Figure 3.4 (a-c). As expected, the $Ge_{30}Se_{70}$ glass is built predominantly by CS and ES tetrahedra, which possess high-

frequency bands A_1 and A_1^C at 200 cm^{-1} (CS) and 219 cm^{-1} (ES) respectively, as well as Se chains with vibration spectra at 230-250 cm^{-1} [97], [98]. These modes for the $Ge_{33}Se_{67}$ composition have a very weak redshift due to the small compositional difference [99]. The Raman spectra of the $Ge_{33}Se_{67}$ and $Ge_{40}Se_{60}$ vibrational band A_G at 180 cm^{-1} demonstrate the Ge-Ge bond belonging to the ETH $Ge_2(Se_{1/2})_6$ building blocks, which dominates the structure of the $Ge_{40}Se_{60}$ films [100]. The vibrational band in the range of 270cm^{-1} to 310cm^{-1} has been fitted with one Gaussian, which implies one type of structural unit. There are several options for the interpretation of vibrational bands around 270cm^{-1}. Usually, they are described as asymmetric vibrations of $(GeSe_{1/2})_4$ ES tetrahedral units, but they could also be asymmetric vibrational mode T2 of ETH units and probably Se–Se stretching vibrations in Se chains [30, 31]. Indeed, the appearance of Se-Se stretching vibrations in the area of 270 cm^{-1} has been confirmed in the zeolite matrix containing chalcogenide glasses [101], [102] and *ab initio calculations* proved that Se-Se vibrations could extend even to 287 cm^{-1} [103]. Bearing that in mind, along with the composition and the size of the vibrational mode, we suggest that it is unrealistic to connect it to the vibrations of Se-Se chains. It is more likely that this vibration is related to asymmetric vibrations of tetrahedral structures containing Ge and Se.

The formation of some Se-Se wrong bonds is not completely excluded, although their appearance is energetically not preferable [104]. Based on these hypotheses, there is an expectation that the Ge-rich glasses are quite phase-separated due to the dominating presence of ETH structures in them, which can form stable clusters in the tetrahedral matrix of this composition [98].

Heating up to the crystallization temperature of $Ge_{30}Se_{70}$ glasses leads to the appearance of the A_1 band near 199 cm^{-1} (low-temperature phase, LT) and near 212 cm^{-1} (high-temperature phase, HT), representing vibrations of CS $GeSe_2$ tetrahedra.

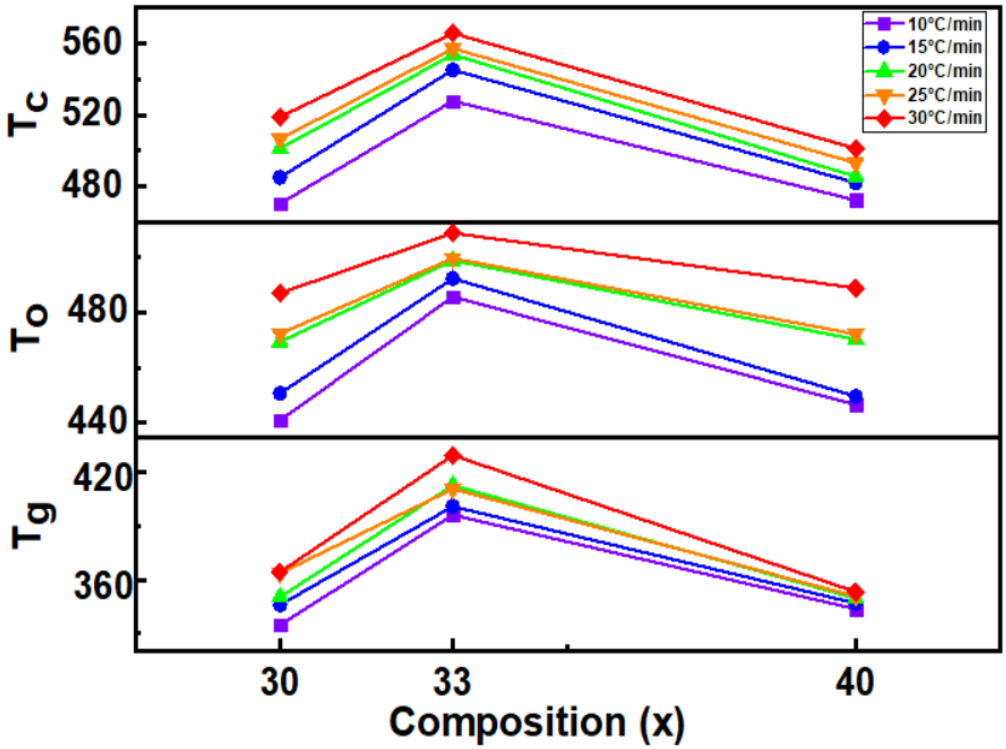

Figure 3.3 T_g, T_o and T_c variation with composition Ge_xSe_{100-x} and heating rate.

In the HT phase, very close to this mode near 218 cm^{-1}, there appears an A_1^C mode representing an in-phase vibration of ES $GeSe_2$ tetrahedra [105]. Raman spectra confirmed that a mixture of LT and HT $GeSe_2$ is present in the crystallized thin films of $Ge_{30}Se_{70}$.

In the amorphous thin films, there are also vibrational modes at 190 cm^{-1} and 275 cm^{-1} which could be related to the appearance of the so-called "wrong bond" Ge-Ge and Se-Se, modes arising due to the disordered organization of the materials which are not completely arranged in crystalline structure since no annealing has been conducted to allow crystal growth and further organization of the crystalline structure.

The Raman spectrum of the crystallized phases of $Ge_{33}Se_{67}$ shows the formation of the low-temperature form of $GeSe_2$ because of the strong dominance of the CS peak. Increasing the amount of Ge in the glass composition to 40% leads to the formation of a crystalline phase at which, simultaneously with the A_G vibrational band, an additional peak is well established and is related to the formation of a new type of crystal structure. The site of the asymmetric tetrahedral units has quite high areal intensity without strong organization in crystalline structures.

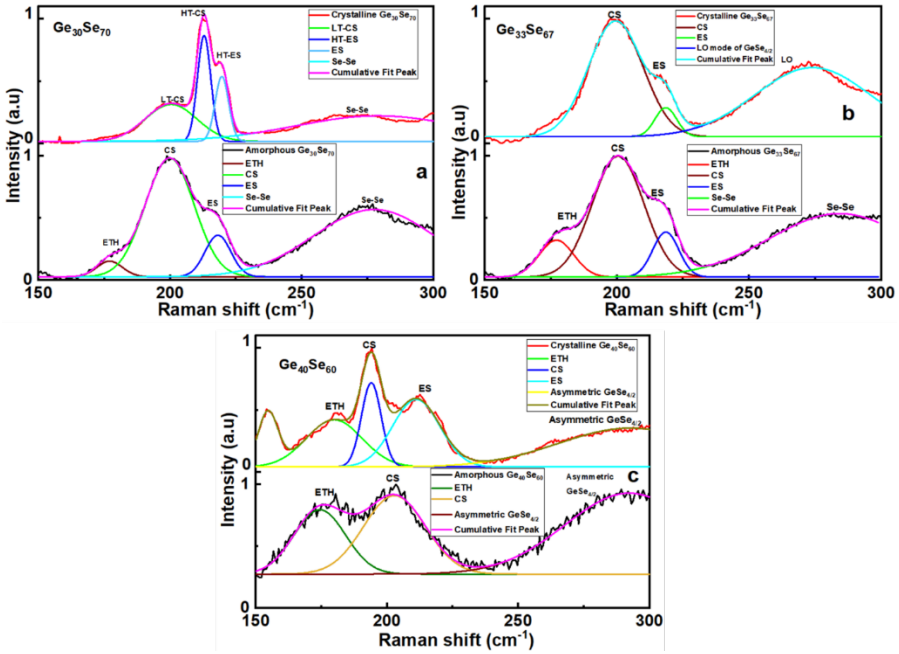

Figure 3.4 Raman spectra of amorphous and crystalline Ge_xSe_{100-x} of a) $x_a = 30$, b) $x_b = 33$ c) $x_c = 40$

The XRD spectra of the crystallized phases are presented in Figure 3.5. There is a well-established dependency of the crystalline phases upon the composition of the glass from which they appear. On the XRD patterns of $Ge_{30}Se_{70}$, in agreement with the Raman spectra showing a mixture of HT (α) and LT (β) phase of $GeSe_2$, XRD confirms the presence of *monoclinic* $GeSe_2$ (LT) and *orthorhombic* $GeSe_2$ (HT) [106], as well as a small size Se crystallites, which are identified at 2θ of 46.16° and 61.92°. Analysis of the

XRD data reveals predominantly *orthorhombic* $GeSe_2$, appearing after crystallization of the $Ge_{33}Se_{67}$ samples. The XRD spectra confirm this type of crystal as the only crystallized phase. The XRD pattern of the crystallized $Ge_{40}Se_{60}$ samples shows the dominance of low-temperature *orthorhombic* α-GeSe [107] with quite small *orthorhombic* and *monoclinic* $GeSe_2$ crystals and a trace of Se at 61.52°. The plurality of crystalline structures appearing from the Ge-rich glasses indicates their phase-separated structure from which different types of crystals are formed. From the normalized data, $Ge_{33}Se_{67}$ has the least amount of Se crystals (0.02219), then $Ge_{40}Se_{60}$ (0.03236) and as expected, the Se-rich composition $Ge_{30}Se_{70}$ has the highest amount of Se crystals (0.06221). Since the stoichiometric composition $Ge_{33}Se_{67}$ consists mostly of $GeSe_2$ tetrahedra, it doesn't have much free Se hence the lowest Se crystalline phase. From Raman, it has been deduced that $Ge_{40}Se_{60}$ is the most phase-separated among the three, but since $Ge_{30}Se_{70}$ is a Se-rich composition, it has more Se crystals than $Ge_{40}Se_{60}$ which supports our interpretation of the Raman band in the area of 270 cm^{-1} and the suggestion that phase separation is occurring in this composition.

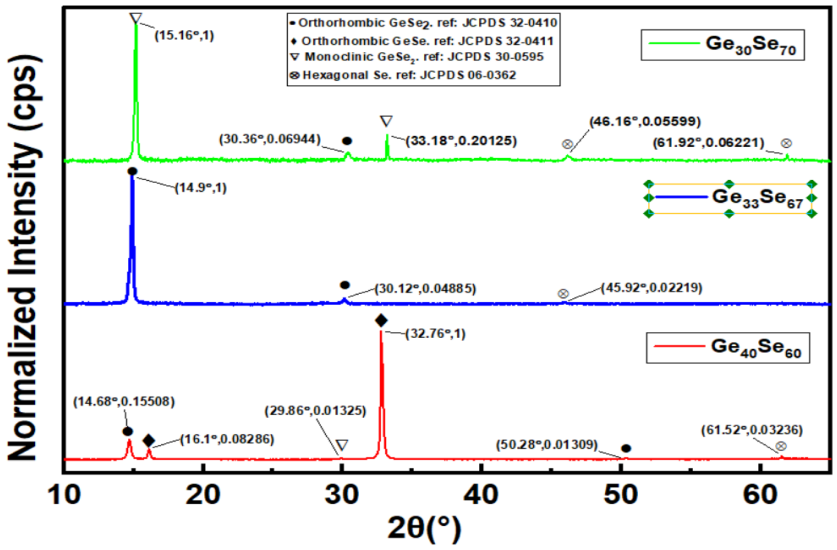

Figure 3.5 X-ray diffraction pattern of crystalline Ge_xSe_{100-x} thin films.

The microscopic images of the obtained crystals are shown in Figure 3.6 (a-c). The Se-rich phases are characterized by two phases - filamentary type of crystals – this is the major phase and a low amount square-shaped darker in color crystals. To be in agreement with the XRD data, we suggest that the filamentary type of crystals is related to Se chains crystallites and the others are the crystallized $GeSe_2$ compositions. This comes in a good accord with the crystallization occurring in the stoichiometric compositions where the crystalline $GeSe_2$ obtains shape and position in the space. The microscopic image shows a homogeneous distribution of similar types of crystalline formations with a well-developed shape, which is a sign of a fast-growth process. In Ge-rich glasses, crystallization starts with the formation of small GeSe or $GeSe_2$ spheroids whose subsequent growth enriches the surrounding material in Se or Ge, respectively [108]. So, in $Ge_{40}Se_{60}$, the result is spheroids formed by a mixture of the two phases, as shown in Figure 3.6.

Figure 3.7 (a-c) shows data about the refractive index of the studied samples obtained at different temperatures. For the Se and Ge-rich samples, the refractive index decreases gradually with temperature until phase change occurs. The refractive index of the crystalline phases is much higher. During heating, defects are removed and as a result of this, scattering inside the thin films is reduced. This makes them more transparent. Also, the thermal expansion would decrease the density, which would lower the refractive index further, as shown in Figure 3.7 (a). When the phase change occurs, due to the presence of long-range order and higher density, the refractive index increases. The data from films with stoichiometric composition $Ge_{33}Se_{67}$ infer a lack of difference in the refractive index for crystalline phases because of the absence of structural changes

between the amorphous and crystalline phases – Figure 3.4 (b), while the Ge-rich films $Ge_{40}Se_{60}$ show anomalous dispersion within the relevant wavelength range – Figure 3.7 (c).

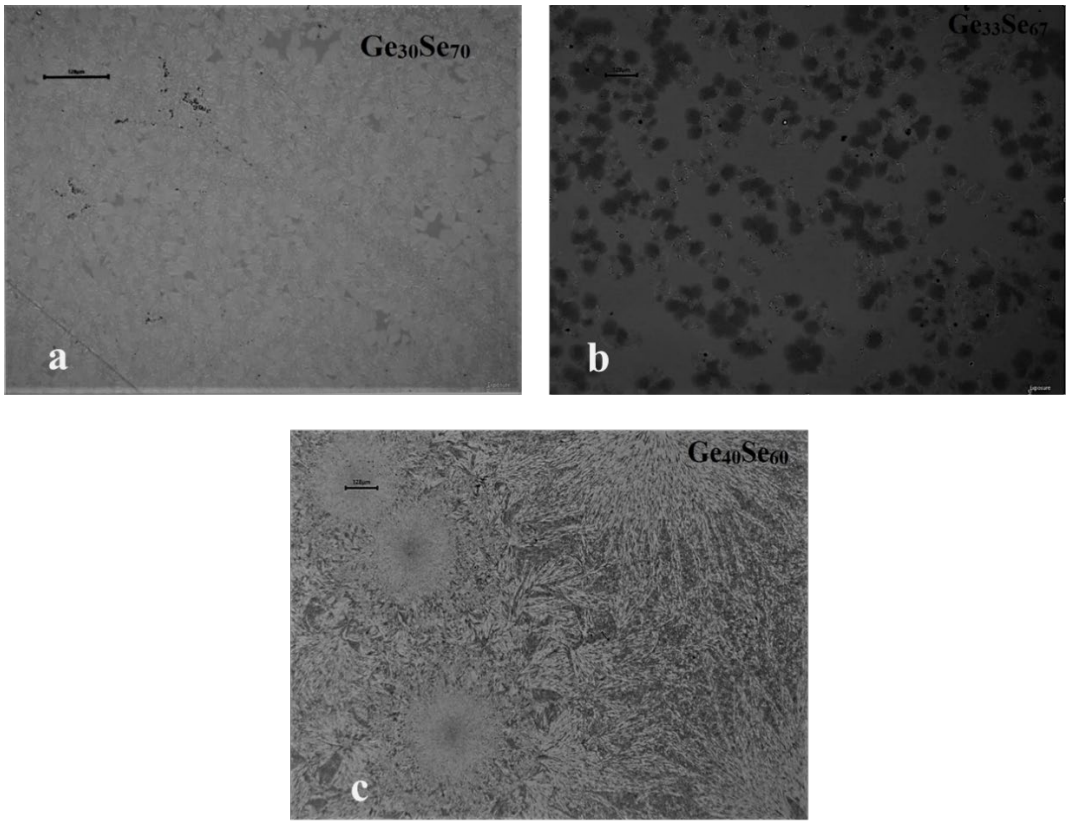

Figure 3.6 Microscopic images of crystallized Ge_xSe_{100-x} thin films a) x=30, b) x=33, c) x=40.

The crystallization of $Ge_{40}Se_{60}$ leads to a substantial increase of the refractive index and can easily be utilized for temperature threshold monitoring, although not following the tendency presented in the previous cases. We suggest that a reason for this is the structural specifics in Ge-rich glasses, which contain ETH structural units, including Ge-Ge bonds. The introduction of external energy to such structure leads to dissociation of these bonds and structural rearrangement – forming new ES building blocks with some of the Se-Se wrong bonds. Such structural rearrangement and opening

of the structure have also been reported after irradiation with γ rays of Ge-rich compositions [109]. Indeed, our Raman spectroscopy results support such a hypothesis, showing significant structural reorganization at crystallization – reduction of the areal intensity of the ETH structures and formation of new ES building blocks.

Discussion

The obtained results are a good foundation for further explanation of the crystallization process in the studied materials. On the other hand, understanding the effects is of vital importance for the photonic temperature sensor relying on phase change. One of the important factors to get stable results from the sensor is the glass stability which is defined as the resistance of glasses towards devitrification upon reheating (especially near or somewhat above the T_g) [110]. A quantitative measure of glass stability is the difference between the onset of crystallization/peak crystallization temperatures and glass transition temperature [111].

Here, both the onset ($\Delta T_o = T_o - T_g$) and peak crystallization temperature ($\Delta T_c = T_c - T_g$) were used to study the stability of the studied glasses. From Figure 3.8, it is seen that ΔT_c is decreasing with Ge introduction in the glassy alloys. This is mainly initiated by the increase of T_g, which follows such dependence upon the rise of the coordination in the glass. Such an effect can also occur due to changes in the dihedral angle between the Se atoms by the increase of cross-linking and rigidity [112]. This indicates that the stability of the stoichiometric glass is expected to be lower due to the relatively high Ge concentration [113], [114]. ΔT_o, on the other hand, shows a different pattern by being minimum for $Ge_{33}Se_{67}$ and having almost equal values for $Ge_{30}Se_{70}$ and $Ge_{40}Se_{60}$. ΔT_o could signify how easy it is to form nuclei in the material during melt quenching.

$Ge_{33}Se_{67}$ being the stoichiometric composition, has the highest tendency to crystallize during melt quenching [115], [116].

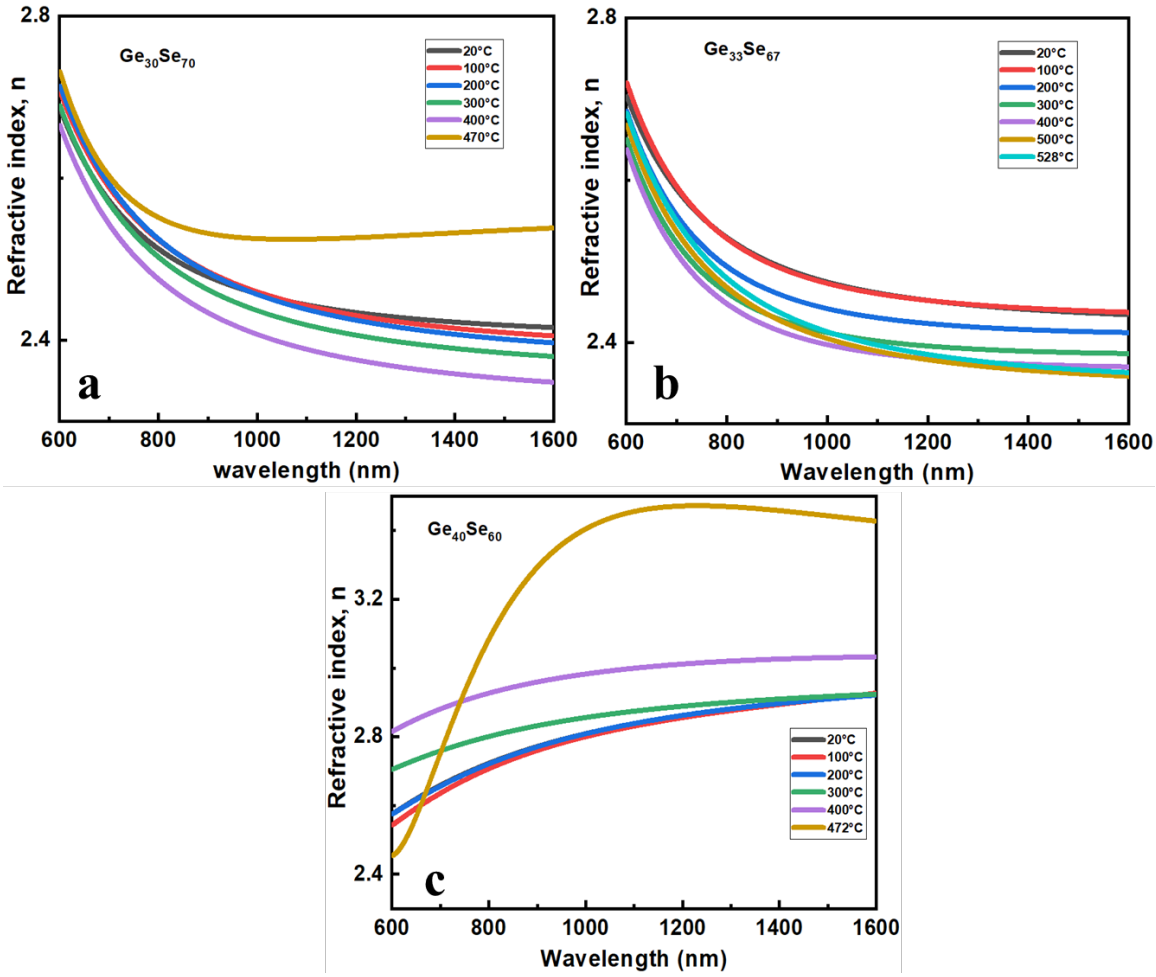

Figure 3.7 Refractive index of Ge_xSe_{100-x} thin films at different temperatures a) x=30, b) x=33, c) x=40.

Having the lowest ΔT_o indicates that during melt quenching, the probability of forming a crystallized fraction in $Ge_{33}Se_{67}$ is higher. This is related to the existence of bigger structural formations indicating crystals clustering, because of the expected homogeneity of the structural organization of this composition, although the formation of homopolar bonds has been established as well [117]. Based on the data, it is assumed that initiating crystallization would be the easiest in the stoichiometric composition, $Ge_{33}Se_{67}$.

But the probability of forming stable crystalline forms grows with increasing concentration of Ge starting from the Se-rich glass. In this aspect, it is important to go further into more details to understand the major driving force in the crystallization process – the nucleation or the crystal growth.

The result about the glass-forming ability should be closely related to the crystallization energy for different compositions, which was calculated applying the Kissinger (3.3) [118], Ozawa (3.4) [119] and Augis-Bennett (3.5) [120] equations

$$ln\left(\frac{T_c^2}{\beta}\right) = -\frac{E_c}{RT_c} + constant \quad (3.3)$$

$$ln(\beta) = -\frac{E_c}{RT_c} + constant \quad (3.4)$$

$$ln\left(\frac{\beta}{T_c^2}\right) = -\frac{E_c}{RT_c} + \ln K_o \quad (3.5)$$

Here, β = Heating rate, E_c = Activation energy of crystallization, K_o= Frequency factor.

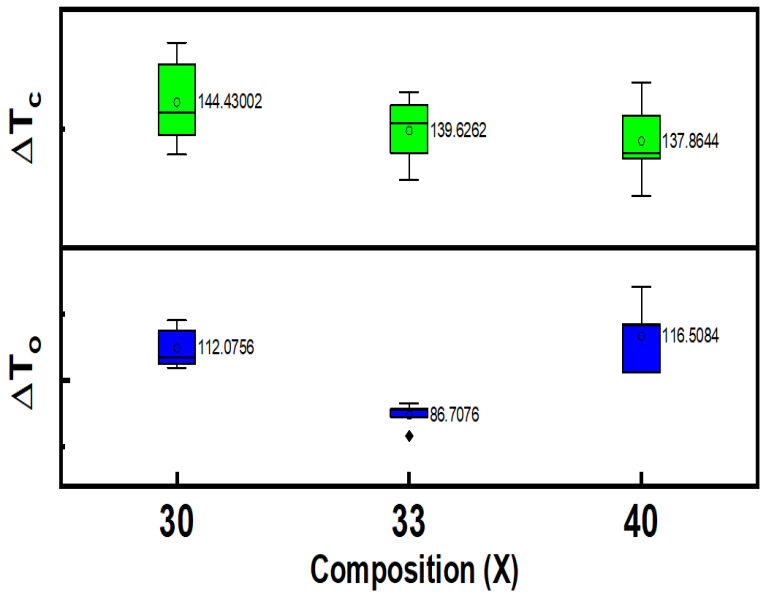

Figure 3.8 Glass formation stability of the Ge-Se studied compositions.

Applying the Augis-Bennett equation (3.5), one more factor – the frequency factor K_o can be calculated. These equations show the dependence of the activation energy upon the peak/onset of crystallization temperature as they change with the heating rate. Figure 3.9 shows the plots of the Kissinger, Ozawa and Augis-Bennett equations. The data about the activation energy obtained by these methods for the studied glasses are presented in Appendix A, Table A.2.

Activation energy calculated using T_c decreases with increasing Ge at%, which contradicts the initial assumption that $Ge_{33}Se_{67}$ would be easiest to crystallize (Figure 3.9). Although there are some small differences in the calculated activation energy due to different initial conditions, the activation energy for the onset of crystallization is the highest for the stoichiometric composition, which is the stark opposite of the expectation. The explanation of such discrepancy was found from Raman spectroscopic data. It is known [97] that in the range $15<x<31$, the number of Ge and Se containing tetrahedra increases with x. The tetrahedra are connected by either ES or CS structural organizations. As the network becomes increasingly saturated with ES and CS tetrahedra, the nanoscale phase separation between them and Se-Se bonds decreases. A new ETH phase initiates near $x>31$ and the ETH units are chemically decoupled from the tetrahedral network. ETH structures are characterized by the formation of the Ge-Ge bond. The Ge-Ge bond has the lowest energy and easily dissociates, making it an important factor for the crystallization process.

So, the dissociation of the Ge-Ge bond helps to form new tetrahedral units by reaction with Se from the Se-Se chains, which crystallize as $GeSe_2$. As a result, the intensity of the Se-Se vibrations reduces to some extent. At $x=33$, the nanoscale phase

separation between tetrahedra and ETH becomes a dominating factor [98] (Figure 3.4 (b)). However, because of the presence of some Se-Se bonds and the availability of ETH, the formation of tetrahedral clusters is possible, which later crystallize as $GeSe_2$. Indeed, as shown in Figure 3.4 (b), the structural reorganization of $Ge_{33}Se_{67}$ is very small upon crystallization. And the Raman spectra in amorphous and the crystalline condition reveal similar structure with the only difference – lack of ETH structural units in the crystalline phase. Because of the homogeneity of the amorphous and crystalline phases, the nucleation process is easy to start, but it is not leading to further fast growth due to a lack of defects or other specific places where the crystals can grow. This explains the results of the glass stability, as shown in Figure 3.8.

The role of the Ge-Ge bonding existing in the ETH structures for Ge-rich glasses due to their high population contributes to the formation of a new nanophase even at a temperature below the T_g, as demonstrated by Wang et al. [98]. The fact that the structural reorganization starts in this case at a temperature below T_g is why the low variability of T_g upon the heating rate is presented in Figure 3.3. Here is the moment to recall the new phase, occurring on the Raman spectrum of the crystalline phase of the Ge-rich glass (Figure 3.4 (c)), which is indeed crystallized GeSe, as shown in the XRD data (Figure 3.5).

The phase separation [98] in the structure of chalcogenide glass manifested in the Raman data has an important effect on crystallization. Crystallization develops in two steps, the initial nucleation of the crystal and the growth of the nuclei by the addition of atoms.

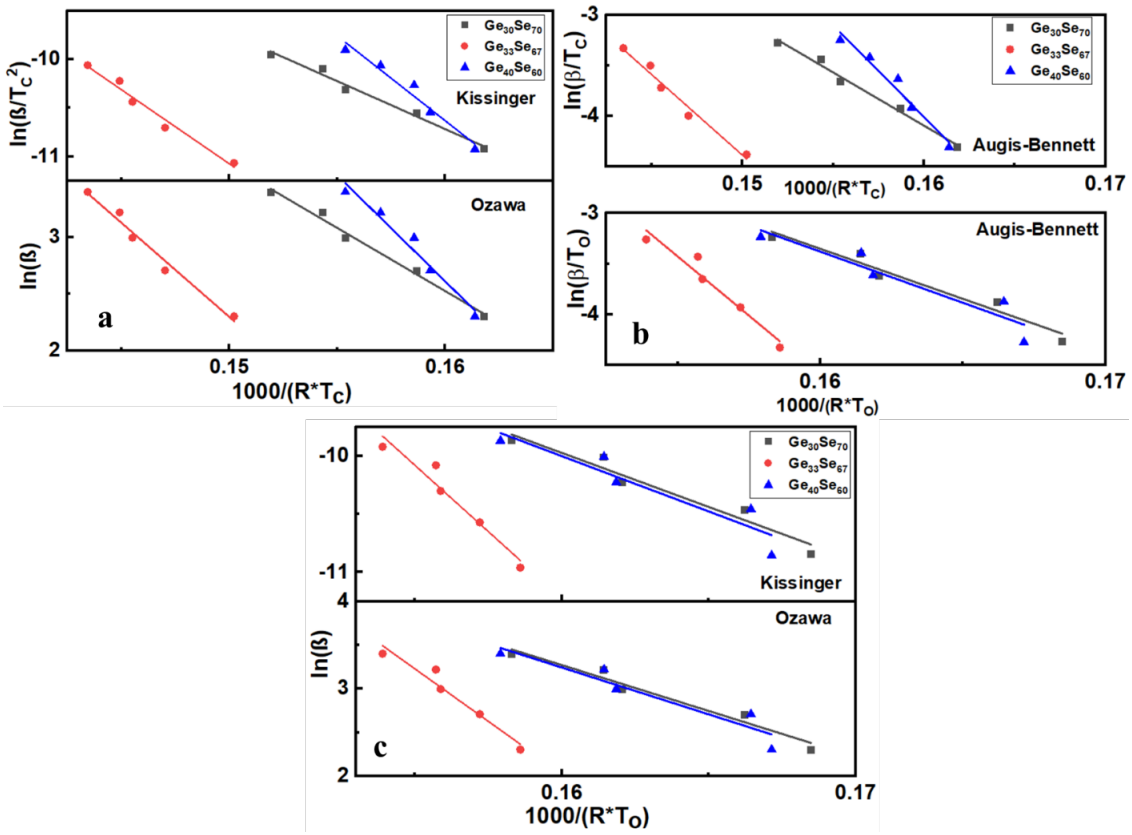

Figure 3.9 Calculation of E_{ac} and E_{ao} using Kissinger, Ozawa and Augis-Bennett methods a) With peak Crystallization Temperature T_c, Kissinger: x = 30: R^2 = 0.9858 Slope = -98.7 ± 6.8 kJmol^{-1} , x = 33: R^2 = 0.9730 Slope = -152.6 ± 14.7 kJmol^{-1}, x = 40: R^2 = 0.9621 Slope = -174.5 ± 20 kJmol^{-1}, Ozawa: x = 30: R^2 = 0.989 Slope = -111.4 ± 6.8 kJmol^{-1}, x = 33: R^2 = 0.977 Slope = -166.6 ± 14.7 kJmol^{-1}, x = 40: R^2 = 0.967 Slope = -187.2 ± 20.0 kJmol^{-1} , b) With peak Crystallization Temperature T_c, x = 30: R^2 = 0.9875 Slope = -105.1 ± 6.8 kJmol^{-1}, x = 33: R^2 = 0.9751 Slope = -159.4 ± 14.7 kJmol^{-1}, x = 40: R^2 = 0.9647 Slope = -180.8 ± 20.0 kJmol^{-1} , With Onset of Crystallization T_o, x = 30: R^2 = 0.9563 Slope = -98.9 ± 12.2 kJmol^{-1}, x = 33: R^2 = 0.9449 Slope = -234.1 ± 32.6 kJmol^{-1} , x = 40: R^2 = 0.8845 Slope = -101.1 ± 21.1 kJmol^{-1}, c) With Onset of Crystallization T_o, Kissinger: x = 30: R^2 = 0.9505 Slope = -92.8 ± 12.2 kJmol^{-1} , x = 33: R^2 = 0.9419 Slope = -227.7 ± 32.6 kJmol^{-1} , x = 40: R^2 = 0.8709 Slope = -95.0 ± 21.1 kJmol^{-1}, Ozawa: x = 30: R^2 = 0.9611 Slope = -105.0 ± 12.2 kJmol^{-1}, x = 33: R^2 = 0.9477 Slope = -240.5 ± 32.6 kJmol^{-1} , x = 40: R^2 = 0.8962 Slope = -107.3 ± 21.1 kJmol^{-1}.

The nucleation can occur by a spontaneous nucleus formation in a melt or glass, this process is called “homogeneous nucleation”. If the nucleus appears on a preexisting surface or an interface, the nucleation is heterogeneous [52, 53]. In essence, the crystalline phase is the one with the lowest enthalpy, compared to the amorphous one, so

that the systems tend to reduce their free energy when crystallizing. The change of free energy during homogeneous nucleation depends on several factors.

$$\Delta G = V\Delta G_v + A_s\gamma \quad (3.6)$$

V is the volume of the crystal nucleus, ΔGV is the bulk free energy change, AS is the particle's surface area, and γ is the surface energy of unit area [46], [121]. Obviously, to achieve stable nucleation and growth, the size of the nuclei has to be larger than a critical value by which the surface energy-related factor is suppressed and requires high bulk energy G_v. In heterogeneous nucleation, because of the preexisting interface in the form of phase separation or other structural units where the crystals can nucleate and grow, the surface factor is reduced and the process requires much lower energy for crystallization. Because of this, heterogeneous nucleation requires less energy than homogeneous nucleation[46], [121] and can result in relatively fast growth, as specifically demonstrated in the case of $Ge_{40}Se_{60}$ composition.

In $Ge_{33}Se_{67}$, the major building block are the CS Ge-Se tetrahedra. Although there is evidence of wrong bonds in this composition [97], [122] the chemical bonding in it is pretty well organized. The Raman spectra of the crystallized phase are much similar to those of the amorphous phase, i.e., there is not a heterogeneous transition for the formation of a new type of structural organization during the crystallization process. Hence, the homogeneous type of crystallization in the $Ge_{33}Se_{67}$ material is the main reason for the highest energy for the onset of crystallization. This result is also supported by the XRD data (Figure 3.5), which demonstrates the formation of only one type of crystalline phase for this material- the *orthorhombic* $GeSe_2$. It is the homogeneous type of crystallization that governs the crystal formation in this case. In this process, the

structural organization of crystals is to a great extent formed in the amorphous condition and its three-dimensionality is preserved in the crystals as demonstrated by the Raman spectra. Indeed, homogeneous crystallization seems to be the reason behind the stability of the refractive index during the crystallization process of $Ge_{33}Se_{67}$. The chemical order before and after crystallization is pretty much the same, due to which the optical properties do not change (Figure 3.7 b). This is not the case for Se-rich and Ge-rich compositions, where phase separation in the glass leads to heterogeneous crystallization and formation of new crystallization products - Se and GeSe, respectively, along with the $GeSe_2$. The formation of completely new phases after crystallization is demonstrated by the XRD data (Figure 3.5 (a, c)). Consequently, there is a substantial change in the refractive index after crystallization (Figure 3.7 (a, c)).

In the case of $Ge_{30}Se_{70}$, the crystallization temperature is very close to the α-to-β transition of the $GeSe_2$ crystals, due to which both phases do exist after crystallization. The *monoclinic* phase dominates due to the relatively higher crystallization temperature of this material.

To further understand the crystallization mechanism, the local Avrami exponent *n(X)* is calculated since the nucleation and growth do not always remain the same during the crystallization process. The Avrami exponent *n* is calculated using Matusita (3.7,3.8) [123] and Blazquez (3.9) [124] equations. Both equations are for non-isothermal processes derived from the Johnson-Mehl-Avrami (JMA) equation [125]–[127], which gives the relation for a process similar to the subject of this study. Figure 3.10 shows the calculation of *n(0)*, which is the value of *n* at the onset of crystallization.

The overall non-isothermal crystallization activation energy E can be obtained using the Matusita equation [123].

$$\ln[(-ln(1-X)] = -ln\beta - 1.052\frac{mE}{RT} + constant \quad (3.7)$$

Where *m* is an integer that depends on the dimensionality of the crystals**.** At constant temperature T, equation (7) reduces to

$$\ln[(-ln(1-X)] = -ln\beta + constant \quad (3.8)$$

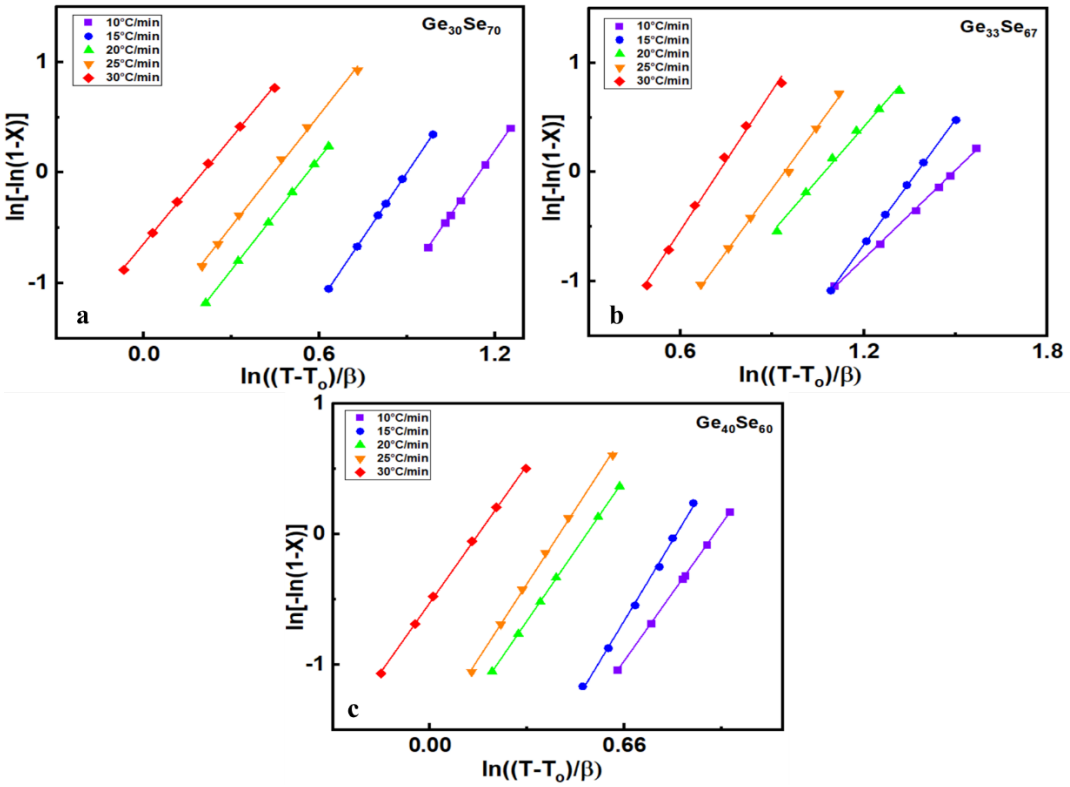

Figure 3.10 Blazquez plots of the GexSe100-x at different heating rates. a) 10°C/min: Slope, n = 3.8 ± 0.0 R^2 = 0.9999 15°C/min: Slope, n = 3.9 ± 0.0 R^2 = 0.9999 20°C/min: Slope, n = 3.4 ± 0.0 R^2 = 0.9999 25°C/min: Slope, n = 3.4 ± 0.1 R^2 = 0.9981 30°C/min: Slope, n = 3.2 ± 0.1 R^2 = 0.9993 b) 10°C/min: Slope, n = 2.7 ± 0.1 R^2 = 0.9989 15°C/min: Slope, n = 3.8 ± 0.1 R^2 = 0.9998 20°C/min: Slope, n = 3.2 ± 0.1 R^2 = 0.9930 25°C/min: Slope, n = 3.8 ± 0.1 R^2 = 0.9981 30°C/min: Slope, n = 4.3 ± 0.2 R^2 = 0.9955 c) 10°C/min: Slope, n = 3.2 ± 0.1 R^2 = 0.9999 15°C/min: Slope, n = 3.7 ± 0.1 R^2 = 0.9978 20°C/min: Slope, n = 3.3 ± 0.0 R^2 = 0.9999 25°C/min: Slope, n = 3.5 ± 0.1 R^2 = 0.9988 30°C/min: Slope, n = 3.2 ± 0.1 R^2 = 0.9995 .

X is the volume fraction of crystal precipitated in the glasses at uniform heating rates, while n and m are the order parameters, which depend on nucleation and growth mechanisms.

To determine how the value of *n* changes during crystallization, the Blazquez [124] equation, which assumes isokinetic crystallization, has been applied.

$$\boldsymbol{n(X) = \frac{1}{1+\frac{E_a}{RT}\left(1-\frac{T_o}{T}\right)} \frac{d\ \ln[(-\ln(1-X)]}{d\ \ln[\frac{T-T_o}{\beta}]}} \quad \textbf{(3.9)}$$

The Avrami exponent *n* can be expressed as [128].

$$\boldsymbol{n = a + bc} \quad \textbf{(3.10)}$$

where *a* is the nucleation index (a = 0 for zero nucleation rate; 0 < a < 1 for decreasing nucleation rate; a =1 for constant nucleation rate and a > 1 for increasing nucleation rate), b is the dimensionality of the growth (b = 1, 2, and 3 for one, two and three-dimensional growth, respectively), c is the growth index (c = 0.5 for diffusion and c = 1 for interface-controlled growth). Avrami exponent calculation plots for the studied glasses at different heating rates is shown in Figure 3.11.

It is seen that all n(X) vs. X curves show a similar tendency. n(X) gradually decreases as the crystallization fraction increases. In $Ge_{33}Se_{67}$ at the beginning, $1.5<n_{33b}(X)<2.25$, which means that the crystallization is initiated by diffusion-controlled one-dimensional growth with a decreasing nucleation rate. With further crystallization, the local exponent decreases and n(X) stays below 1.5 during almost the entire crystallization process.

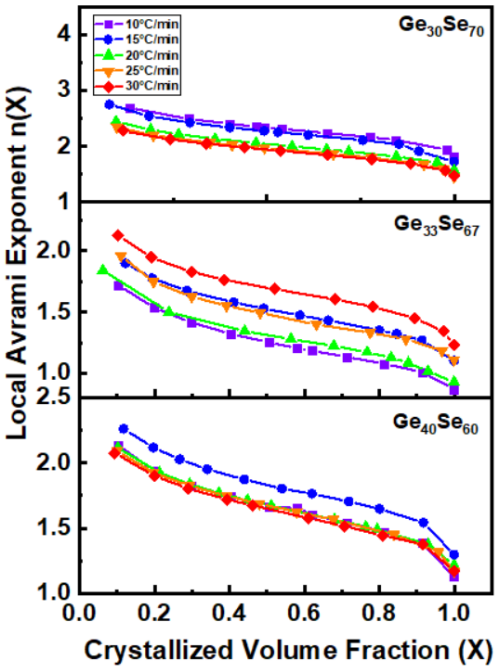

Figure 3.11 Local Avrami exponent calculation plots of the Ge_xSe_{100-x} at different heating rates.

This indicates that the nucleation is saturated and there are lots of crystal nuclei growing in any one dimension. However, the initial expansion in nuclei formation suggests homogeneous crystallization. The microscopic image – Figure 12 (b), demonstrates a large number of relatively small crystals, also confirmed by calculating their intensity from the XRD data (Figure 3.5 (b)), which do not introduce a considerable change to the refractive index (Figure 3.7 (b)).

For $Ge_{40}Se_{60}$ and $Ge_{30}Se_{70}$, the starting values of *n(X)* are larger than the value for $Ge_{33}Se_{67}$. But still smaller than 2.5 for all cases under the same conditions. It can be inferred that the crystallization mechanism is dominated by the growth of primary crystal type and the nucleation rate decreases with time. Further crystallization drops *n(X)* below 1.5, indicating that the concentration of preexisting nuclei has saturated and the three-dimensional growth dominates. These data also confirm the heterogeneous character of the crystallization. It is known that during heterogeneous crystallization, once the nuclei

are formed on a preexisting specific position, their number stays almost constant and the crystal growth is the dominant process. This effect is strongly pronounced for the $Ge_{40}Se_{60}$ glass, where the big size of the formed crystals – Figure 3.5 and Figure 3.6 (c), contributes to a substantial change in the refractive index (Figure 3.7 (c)).

From Matusita's equation, the calculated n values (Figure 3.12) are larger than those calculated by the previous method $n_{30m} = 4.27$, $n_{33m} = 2.39$ and $n_{40m} = 3.98$ (average of the calculated values). We can round the numbers to $n_{30m} = 4$, $n_{33m} = 2$ and $n_{40m} = 4$. For $Ge_{33}Se_{67}$, the mechanism behind the crystallization cannot be different, so Matusita's equation gives a higher rate of nucleation. It means that at the beginning, $a>1$ for a very short time. From Matusita's equation, n values clearly show that $Ge_{33}Se_{67}$ has the lowest nucleation rate by calculating one parameter. However, it does not explain how n changes during crystallization.

$\ln[-\ln(1-X)]$ vs $1000/(R*T)$ plot gives the total activation energy of crystallization in the form of slope = $-1.052*m*E_c$ ($kJmol^{-1}$) – Figure 3.13. Here, $n=m+1$ when the quenched glasses are nuclei free and n=m for preheated glass, which contains a large number of nuclei [123]. In other words, $n=m$ for isothermal crystallization and $n=m+1$ for non-isothermal crystallization. But for this analysis, n must be an integer. So, considering $n_{30m} = 4$, $n_{33m} = 2$ and $n_{40m} = 4$, gives $m_{30} = m_{40} = 3$ and $m_{33} = 1$. This means that for x=30 and x=40, the growth of the crystals develops three-dimensionally, whereas in $Ge_{33}Se_{67}$ the growth is in one dimension, which agrees with the Blazquez equation.

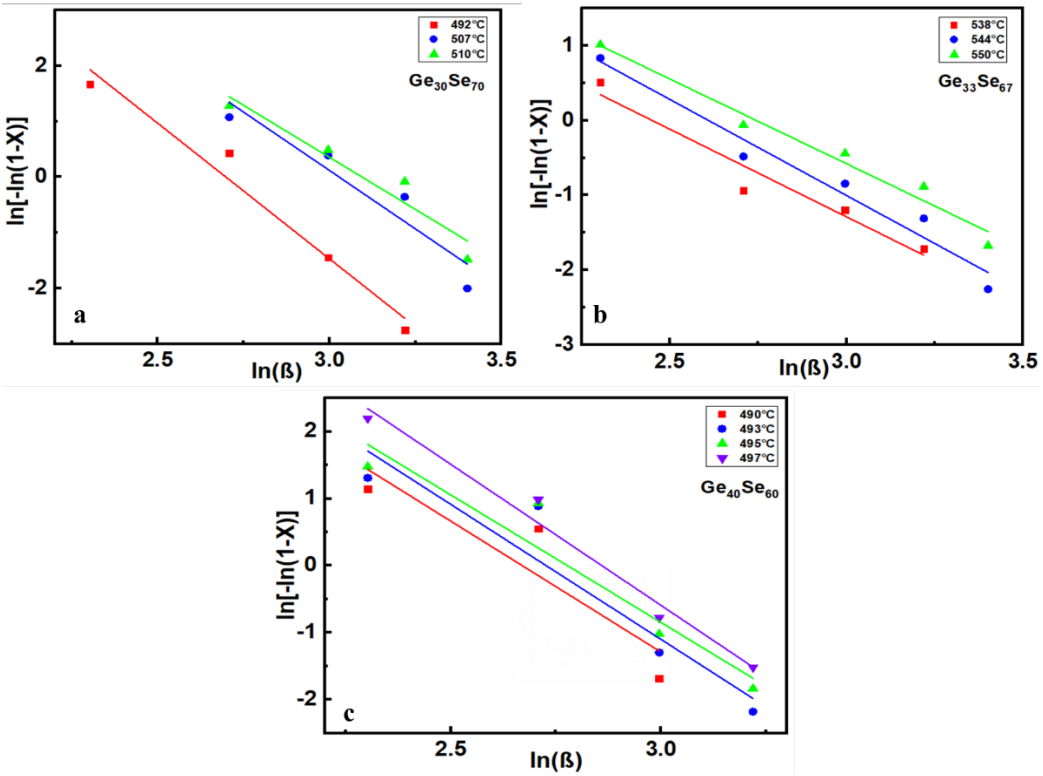

Figure 3.12 ln[-ln(1- X)] vs ln(β) plots for n value of the Ge_xSe_{100-x} at different temperatures a) 492°C: R^2 = 0.9703 Slope = -4.9 ± 0.6 507°C: R^2 = 0.8999 Slope = -4.2 ± 1.0 510°C: R^2 = 0.9257 Slope = -3.7 ± 0.8 b) 538°C: R^2 = 0.9452 Slope = -2.3 ± 0.4 544°C: R^2 = 0.9629 Slope = -2.6 ± 0.3 550°C: R^2 = 0.9728 Slope = -2.3 ± 0.2 c) 490°C: R^2 = 0.8338 Slope = -3.9 ± 1.7 493°C: R^2 = 0.8940 Slope = -4.0 ± 1.0 495°C: R^2 = 0.9170 Slope = -3.8 ± 0.8 497°C: R^2 = 0.9786 Slope = -4.2 ± 0.4 .

The results from Matusita's equation are tabulated in Table A.3. It is seen that the activation energies for different compositions calculated from the Matusita equation are not close to the average activation energy calculated using Kissinger, Ozawa and Augis-Bennett equations. The difference between the values could be attributed to various assumptions each theory is based upon. However, activation energy calculated from Matusita's equation shows a similar pattern – Figure 3.13, like, the activation energy of $Ge_{33}Se_{67}$ is much higher than the rest of the two compositions. So, the effect of phase-homogeneity is best observed in Matusita's equation.

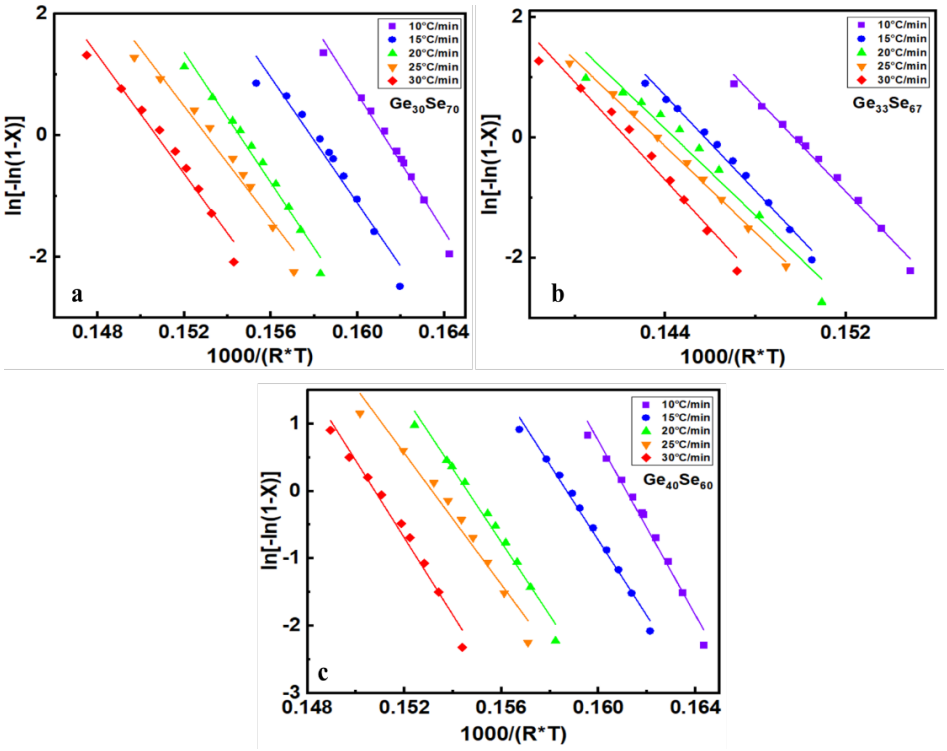

Figure 3.13 ln[-ln(1-X)] vs 1000/(R*T) plots for Ec calculation using Matusita equation of the Ge_xSe_{100-x} at different rate. a) 10°C/min: R^2 = 0.9821 Slope = -564.9 ± 27.0 $kJmol^{-1}$ Intercept = 91.1 ± 4.4 15°C/min: R^2 = 0.9540 Slope = -518.5 ± 40.3 $kJmol^{-1}$ Intercept = 81.8 ± 6.4 20°C/min: R^2 = 0.9807 Slope = -536.8 ± 26.6 $kJmol^{-1}$ Intercept = 83.0 ± 4.1 25°C/min: R^2 = 0.9665 Slope = -467.6 ± 32.9 $kJmol^{-1}$ Intercept = 71.6 ± 5.1 30°C/min: R^2 = 0.9704 Slope = -489.3 ± 32.3 $kJmol^{-1}$ Intercept = 73.7 ± 4.9 b) 10°C/min: R^2 = 0.9894 Slope = -391.5 ± 14.3 $kJmol^{-1}$ Intercept = 58.6 ± 2.2 15°C/min: R^2 = 0.9896 Slope = -396.0 ± 14.3 $kJmol^{-1}$ Intercept = 57.7 ± 2.1 20°C/min: R^2 = 0.9558 Slope = -360.0 ± 29.3 $kJmol^{-1}$ Intercept = 52.0 ± 4.2 25°C/min: R^2 = 0.9957 Slope = -358.7 ± 9.0 $kJmol^{-1}$ Intercept = 51.5 ± 1.3 30°C/min: R^2 = 0.9764 Slope = -406.6 ± 23.9 $kJmol^{-1}$ Intercept = 57.8 ± 3.4 c) 10°C/min: R^2 = 0.9830 Slope = -646.7 ± 30.1 $kJmol^{-1}$ Intercept= 104.2 ± 4.9 15°C/min: R^2 = 0.9902 Slope = -560.8 ± 19.7 $kJmol^{-1}$ Intercept = 89.0 ± 3.1 20°C/min: R^2 = 0.9826 Slope = -544.2 ± 25.6 $kJmol^{-1}$ Intercept = 84.1 ± 4.0 25°C/min: R^2 = 0.9664 Slope = -487.2 ± 34.3 $kJmol^{-1}$ Intercept = 74.6 ± 5.3 30°C/min: R^2 = 0.9816 Slope = -573.0 ± 29.6 $kJmol^{-1}$ Intercept = 86.4 ± 4.5 .

Conclusion

The collected data revealed significant information in understanding the nature of the effects occurring and what to expect if different compositions are embedded as active films of a temperature sensor based on optical monitoring of phase change. The Se-rich materials crystallize in a hetero-crystallization process with many phases occurring,

which requires relatively low crystallization energy. Their XRD patterns have demonstrated the presence of a variety of crystals. This crystallization variability also brings a significant change in the optical properties at the crystallization temperature, which can be used for reading the effect, applying optical methods. The stoichiometric glasses show incredibly similar Raman spectra of the amorphous and crystalline phases, which is an indication that the glassy phase has a good structural organization with a very low number of defect configurations. It is for this reason that the stoichiometric material crystallizes in only one phase by homogeneous crystallization. Homogeneous crystallization requires higher energy than heterogeneous and $Ge_{33}Se_{67}$ shows no changes in the optical parameters because of limited differences in the structure of the amorphous and crystalline phases. The Ge-rich phases crystallize in heterogeneous crystallization due to the high number of structural defects demonstrated on the Raman spectra and most importantly, due to the presence of ETH units. They release Ge atoms, capable of reacting with the wrong Se-Se bonds. Therefore, a substantial non-linear change of the optical properties of these films as a function of temperature at the phase change point provides the basis for monitoring phase change effects as a function of temperature by optical methods.

CHAPTER FOUR: RADIATION HARDNESS OF CHALCOGENIDE GLASSES

This chapter describes the study of the radiation hardness of ChGs. Gamma, neutron and Xe ion irradiated thin films were characterized using various methods.

Radiation Hardness of Chalcogenide Glasses

Due to the lack of order, a high number of defects and availability of lone-pair electrons on chalcogenide atoms, the chalcogenide glasses are radiation hard. This is because the intrinsic defects and the defects caused by irradiation [127] populate in very close proximity and recombine rapidly. More details in this aspect are given in the Introduction chapter, where the reasons for the stability of the electrical properties of the material are explained. This effect is manifested at the performance of many types of devices based on chalcogenide glasses which demonstrate stable operation under irradiation with visible light [129], high-intensity X-rays [130], gamma irradiation [131], as well as irradiation with 50 MeV protons [132] and low-intensity Ar^+ [133]. We studied the interaction of the thin films of glasses with neutrons, a combination of neutrons and gamma rays, and Xe ions. The Xe ion's choice is based on the fact that Xe is chemically inert, non-radioactive and one of the typical fission products, offering a cost-effective and safer alternative to neutron irradiation. Moreover, since the thermal neutron cross sections of naturally abundant Ge, Se, Al and Ni isotopes used in the sensor are quite low (Ge 0.4, Se 0.61, Al 0.231 and Ni 4.6) [7], the possibility of nuclear transmutation is low and so this study is focused on ion-induced damage only. The other advantages of ion

irradiation are: higher damage rate (10^4 times) compared to reactor irradiation reducing the experimental duration to days instead of decades; the irradiated samples are not radioactive, so post-irradiation characterization cost is reduced; ion irradiation experiments can be controlled better to some extent (e.g., temperature, damage rate, damage level) than reactor irradiation and there's the provision to observe the damage in-situ. However, emulation of neutron irradiation using ion is a new idea and the experiments must be tailored according to the materials and higher control of parameters is needed. This chapter could be used as a guideline for material testing by emulating reactor irradiation with well-controlled ion irradiation.

Results

To study neutron and gamma-induced change in the amorphous ChG, thermally evaporated thin films were irradiated with neutron and gamma-ray and their structure studied.

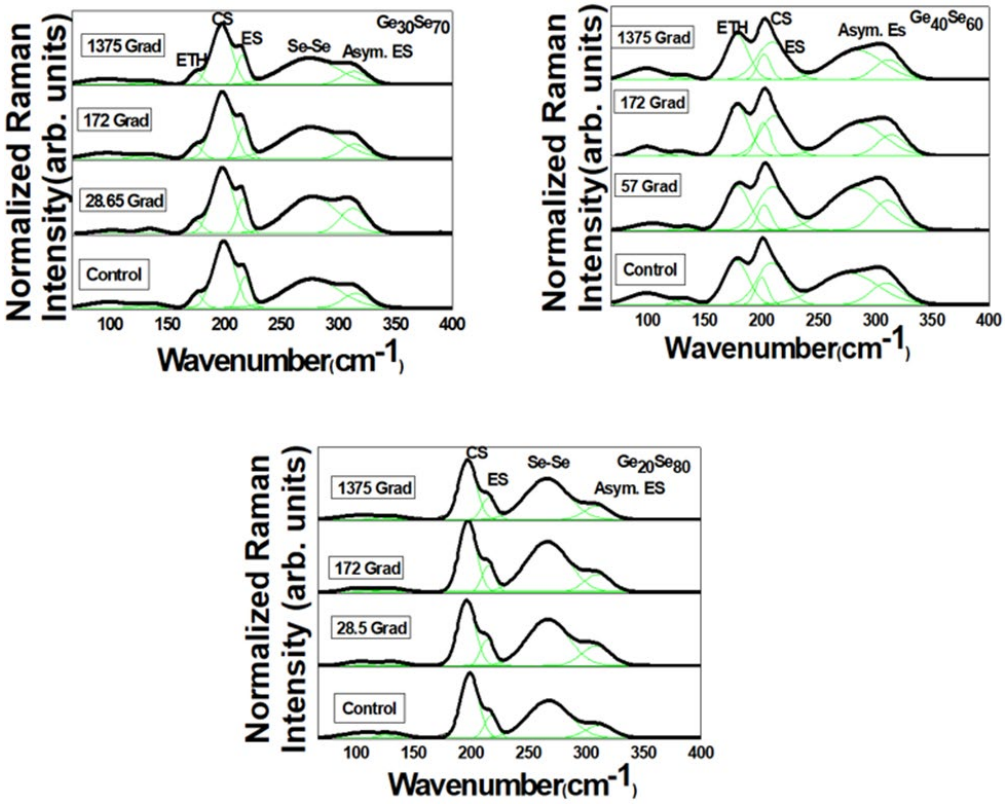

Figure 4.1 Raman spectra of neutron irradiated ChG thin films $Ge_{30}Se_{70}$, $Ge_{40}Se_{60}$ and $Ge_{20}Se_{80}$.

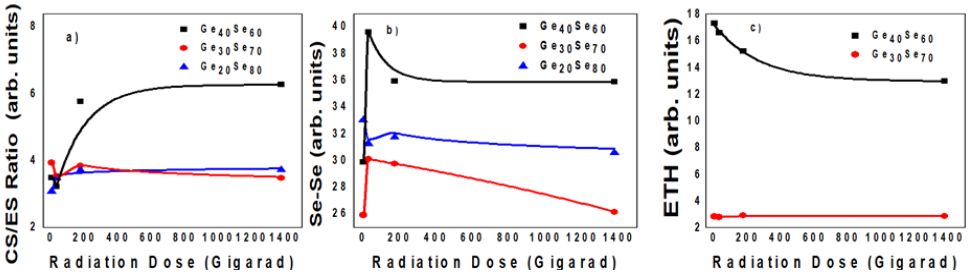

Figure 4.2 Raman relative structural units analysis due to neutron irradiation for different composition of Ge_xSe_{100-x} films.

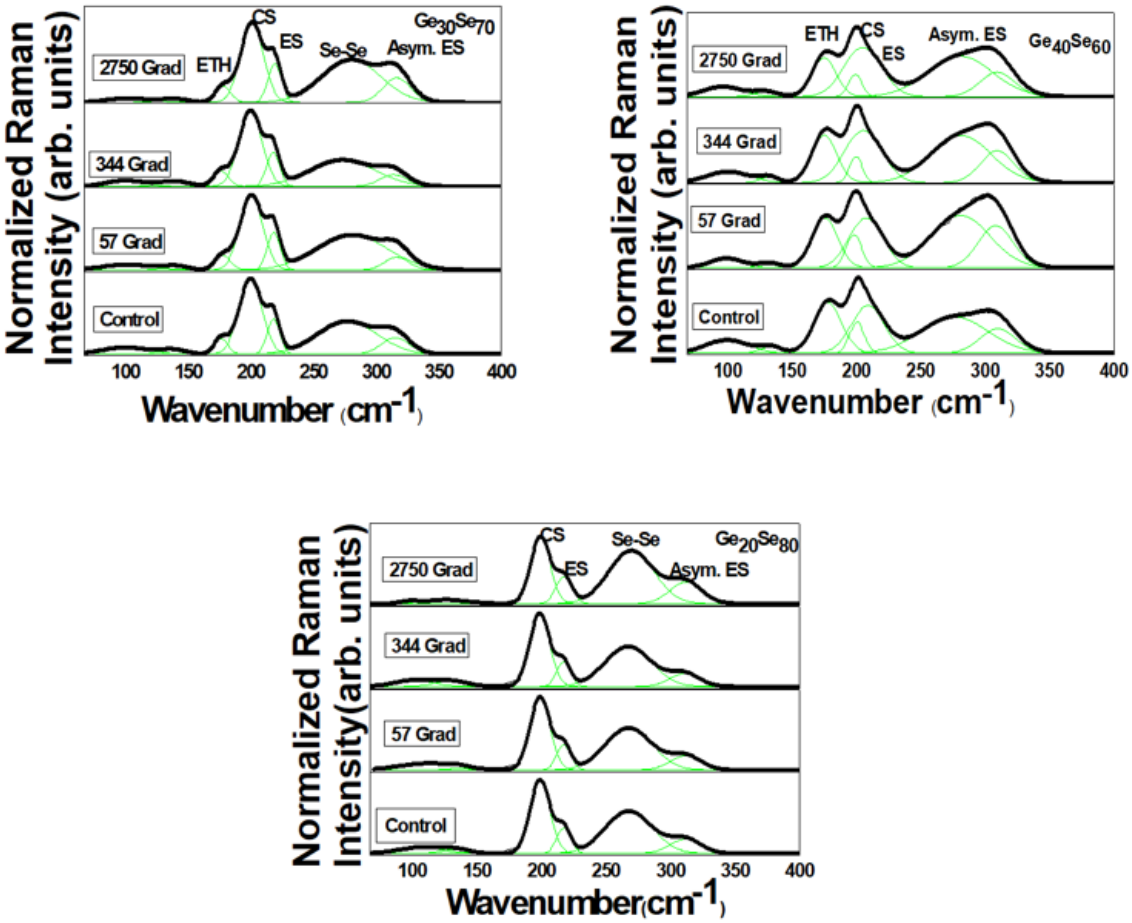

Figure 4.3 Raman spectra of neutron and gamma irradiated ChG thin films $Ge_{30}Se_{70}$, $Ge_{40}Se_{60}$ and $Ge_{20}Se_{80}$.

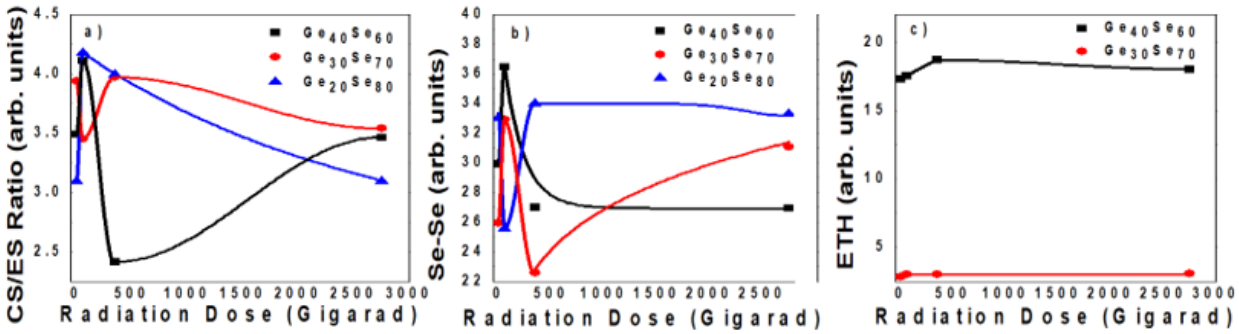

Figure 4.4 Raman relative structural units' analysis due to neutron and gamma irradiation for different composition of Ge_xSe_{100-x} film.

The thin films were irradiated with 100, 200 and 1400 Gigarad dose of radiation. In Figures 4.2 and 4.4, changes in structural units are analyzed. Structural areal intensity are calculated from the data in Figures 4.1 and 4.3, respectively, by Gaussian deconvolution. Here, CS/ES is the ratio of the areal intensity of corner-sharing to edge-sharing, Se-Se is the selenium-selenium bond and ETH is the ethane-like structure. Under irradiation in the presence of γ rays, all the structures except for ETH (which is absent at x = 20) for all compositions show significant changes for low dose radiation, but the changes become less responsive to radiation as the dose increases. After prolonged exposure without a filter, i.e., in the presence of γ rays, the number of structural units is found to be very close to that of the unexposed thin films. It is seen that with neutron only irradiation, the CS/ES ratio goes higher for $Ge_{40}Se_{60}$ and $Ge_{20}Se_{80}$. Except for ETH units, $Ge_{30}Se_{70}$ (closest to stoichiometry with less homopolar bonds) does not show much change in structures. As $Ge_{30}Se_{70}$ has the lowest density, this behavior was expected. Even though neutron irradiation induces some change at a lower dosage, the number of each unit has been found to be close to the initial value after longer exposure.

For the reliable operation of the sensors, the devices must maintain the SET status under irradiation. The crystalline structure has long-range order, which could get disrupted by neutron-induced damage. Since neutron-irradiated samples have residual radiation, they are difficult to characterize. To emulate neutron-induced damage, ion irradiation is a cheaper and safer alternative [134]. To have a qualitative idea, crystallized thin films were irradiated with Xe ions of 200, 600 and 1000 keV, fluence $10^{14}cm^{-2}$. This estimates to 5 displacements per atom (DPA). All calculations are presented in Appendix B.

As mentioned before, it is expected that during irradiation, microstructural deformation and defects will recombine up to some extent. Raman spectroscopy of the amorphous thin films confirms this hypothesis. It is seen that the $Ge_{30}Se_{70}$ glass in Figure 4.5 (a), is built predominantly by CS and ES tetrahedra and Se chains (CH). The presence of such structural units is proved by the high-frequency bands A_1 and A_1^C at 200 cm^{-1} (CS) and 219 cm^{-1} (ES), respectively. The occurrence of Se chains is demonstrated by the vibration spectra at 230-280 cm^{-1} [97], [98]. After irradiation with 200 keV, the Raman spectra demonstrate an increased areal intensity of the Se-Se chain mode and breaking of the ES building blocks, which at higher irradiation are restored and at irradiation with 1000 keV their aerial intensity related to the areal intensity of the CS units is close to the initial one before irradiation although their absolute values are smaller - Figure 4.5 (a). The crystalline structure- Figure 4.5 (b), firmly demonstrates phase change and crystalline structure characteristic for the low temperature (LT) polymorph form of $GeSe_2$ [135]. However, this crystal structure loses stability after irradiation, the Raman modes undergo a low energy shift, which is characteristic of the modes arising from a more disordered structure. With the increase of the irradiation energy, the formation of ES breathing mode becomes more prominent, which indicates crystallization of the high temperature (LT) polymorph form of GeSe.

In addition to CS, ES and Se-Se peak, $Ge_{33}Se_{67}$ thin films exhibit a distinct peak in Figure 4.6 (a), around 178cm^{-1}, which indicates vibrations of Ge-Ge bonds representing the formation of ethane-like structure $Ge_2(Se_{1/2})_6$ (ETH) [100]. After irradiation, a reduction of both Ge-Ge and Se-Se aerial peak intensity is seen along with an increase in ES peak intensity, suggesting structural reorganization and consuming the

wrong bonds to form ES structures. The Raman spectra of as-prepared crystallized films in Figure 4.6 (b) exhibit only well-expressed CS vibrations, characteristic for the HT $GeSe_2$ polymorph form.

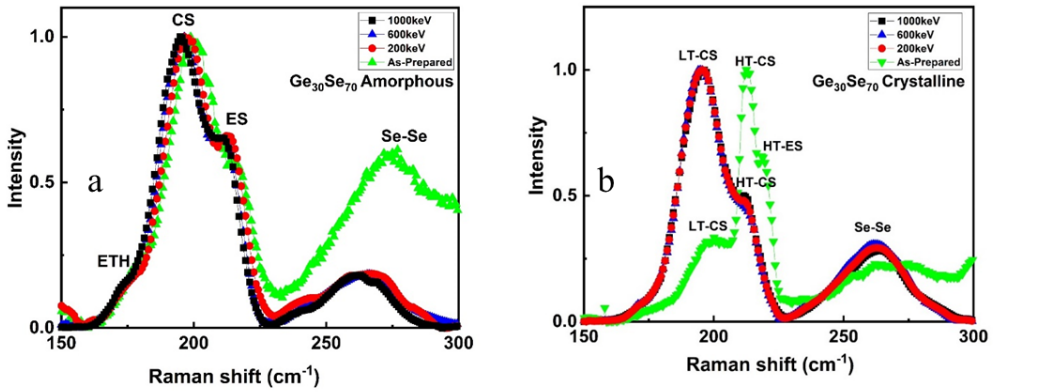

Figure 4.5 Raman spectra of $Ge_{30}Se_{70}$ under different irradiation. a) Amorphous b) Crystalline.

After irradiation, structural transformation occurs by which the formation of ES vibrations is well shaped on the Raman spectra, indicating crystallization of LT GeSe. This effect is accompanied by a decrease in the areal intensity of the Se-Se chain mode.

As expected, the ETH structure dominates in the Raman spectra of the $Ge_{40}Se_{60}$ films in Figure 4.7 (a). Moreover, the vibrational band in the range of 270 cm^{-1} to 310 cm^{-1} can be fitted with one Gaussian, which implies the presence of only one type of structural unit. The size of the vibrational mode and the composition suggest that it is unrealistic to consider that this vibrational band is occurring from Se-Se chains which are energetically not favorable [104]. It is more logical to consider this vibration related to asymmetric vibrations of tetrahedral structures containing Ge and Se. So, we suggest that these vibrations are related to asymmetric ES breathing mode. Based on this hypothesis, the Ge-rich glasses are anticipated to be quite phase-separated. Up to 1000 keV energy,

these films keep their basic structure. However, at irradiation with 1000 keV, the structure is destroyed, representing only CS and ES vibrations simultaneously with a substantial decrease of the areal intensity around 267 cm^{-1}.

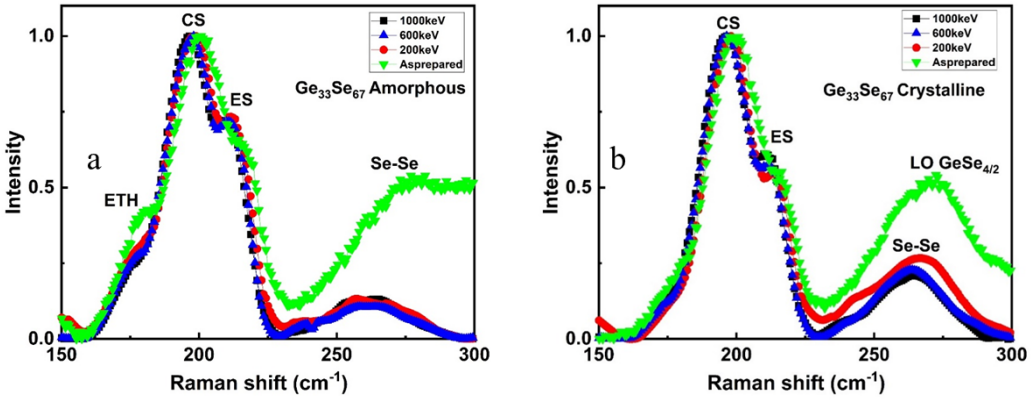

Figure 4.6 Raman spectra of $Ge_{33}Se_{67}$ under different irradiation. a) Amorphous b) Crystalline.

The non-irradiated crystals suggest the formation of the LT $GeSe_2$ in Figure 4.7 (b). After irradiation, there is a growth of the areal intensity at lower energy, which suggests a strong development of CS and ES structural units, leading to the formation of the LT GeSe.

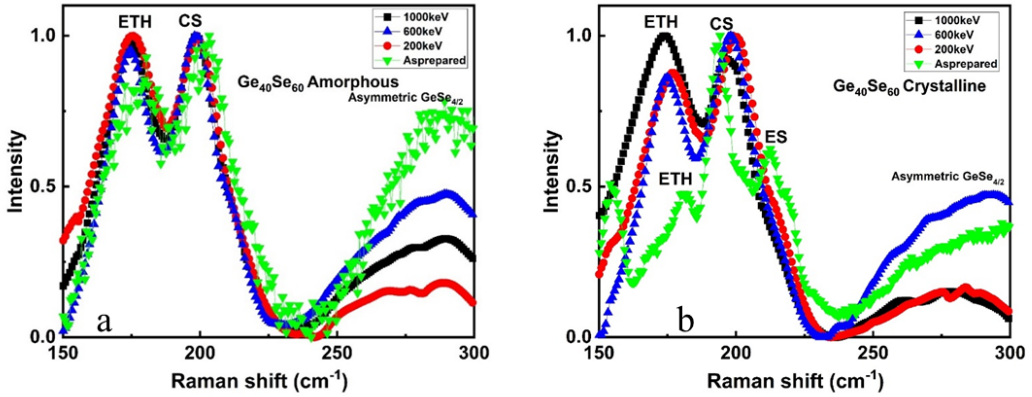

Figure 4.7 Raman spectra of $Ge_{40}Se_{60}$ under different irradiation. a) Amorphous b) Crystalline.

The XRD spectra of the crystallized thin films are presented in Figure 4.8 (a-c).

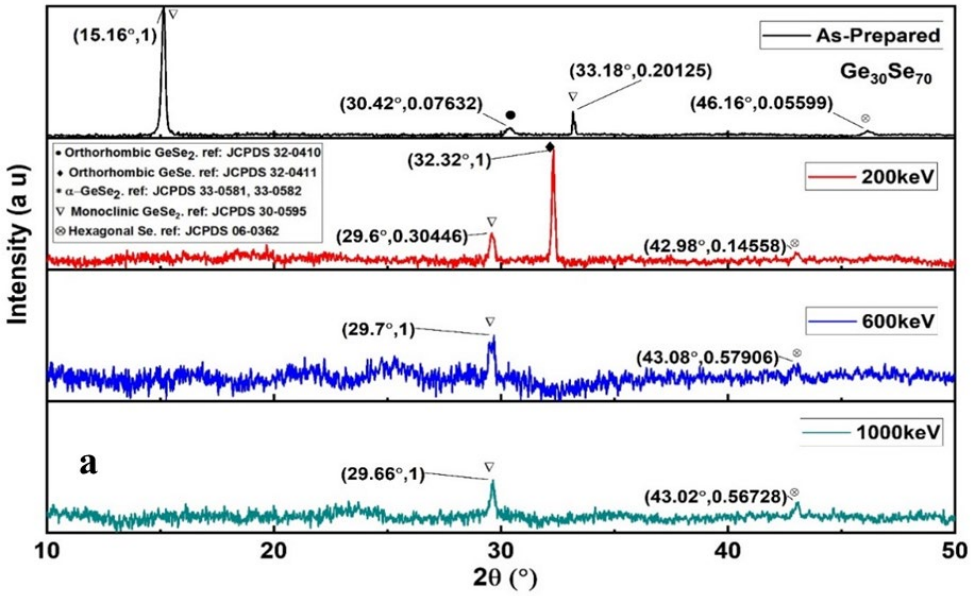

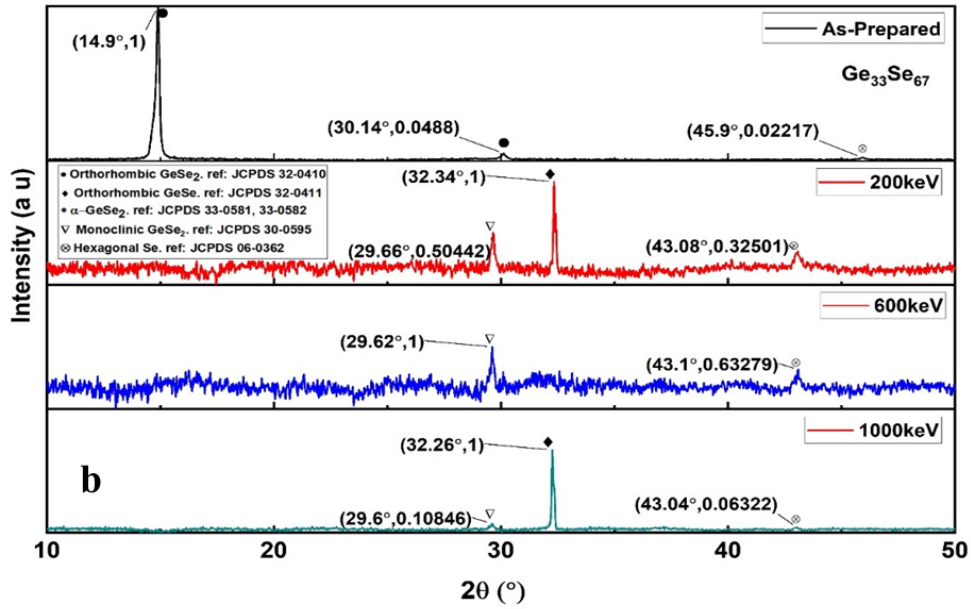

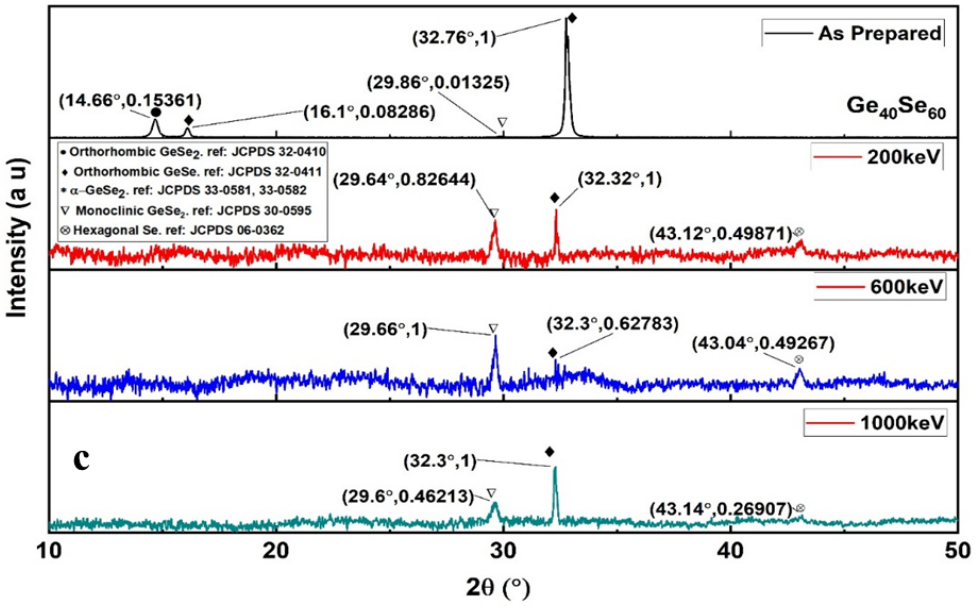

Figure 4.8 XRD of irradiated and as-prepared crystallized thin films. a) $Ge_{30}Se_{70}$ b) $Ge_{33}Se_{67}$ c) $Ge_{40}Se_{60}$.

The XRD data confirm the Raman results in this that they demonstrate a presence of the LT $GeSe_2$ phase at the initial crystallization, which then is transformed into an LT GeSe phase. Hexagonal Se is present in all thin films and its crystal size is related to the availability to form wrong bonds after irradiation. In many cases, GeSe crystals are also present and although their appearance seems to be very sporadic, it needs in-depth discussion. In $Ge_{30}Se_{70}$, GeSe is not present in the as-prepared film. It only emerges after 200 keV irradiation and after 600 and 1000 keV, the GeSe peak is missing - Figure 4.8 (a). In $Ge_{33}Se_{67}$, the GeSe peak emerges after 200 keV irradiation and is missing only for 600keV – Figure 4.8 (b). In $Ge_{40}Se_{60}$, all three peaks are present for each condition – Figure 4.8 (c). But for 600keV, the GeSe peak suggests the formation of crystals with the smallest size.

Discussion

Regarding the interaction of the films with a mixture of neutrons and γ rays, we suggest that the sensitivity of the material is a function of the creation of some electron-hole pairs by electromagnetic irradiation, which affects the material's structure. This effect is accelerated when neutrons are present, which contributes to a very close proximity of all formed defects that recombine fast and the structure of the films relaxes in a condition close to the initial one. Traveling through solids, ions interact/collide with stationary atoms and change their initial trajectory. While traveling, they also lose energy in radiative processes. Since the radiative processes like bremsstrahlung and Cherenkov radiation are very limited for ions, they can be neglected. In addition, ions can pick up electrons from various shells and become a very slow-moving ion going through cascade collisions and ultimately stop. So, there are two types of energy transfer mechanisms involved i) elastic scattering: collision of nuclei, and ii) inelastic collision: excitation and ionization of atoms. Typically, when ion energy is below 10keV/amu, elastic scattering dominates [136].

TRIM simulation showed the penetration range of the Xe ions in different compositions. The TRIM simulation of the Xe ions interaction, an example of which is shown in Figure 4.9 for $Ge_{40}Se_{60,}$ demonstrates that at the chosen fluence, ions with energy 200 keV (1.53 keV/amu) penetrate only in the chalcogenide glass film, the ions with energy 600 keV (4.58 keV/amu) reach the SiO_2 film and stop close to the interface ChG/SiO_2 and those with 1000 keV (7.65 keV/amu) energy penetrate the SiO_2 substrate. It should be noted here that Figure 4.9 shows both the range of the ions (d) and actual depths (a-c).

This is characteristic for all studied compositions with small variations in the particular penetration depth, which depends upon the density of the chalcogenide glass (Figure 4.10 [137]) which is one other factor to be considered.

The simulation shows that the longitudinal penetration range increases with ion energy and decreases with the density of the material. The peak damage rate calculated from TRIM shows an opposite to the penetration pattern in Figure 4.11. Damage goes lower with energy and is proportional to the density. We suggest that with more energy, the ions penetrate further and more interaction happens at the interface or in the substrate. Also, ions interact more with denser materials, since they come in contact with a higher number of atoms, hence higher damage rate in $Ge_{40}Se_{60}$. Another important factor here is the size of the atoms compared to the ions. The Xe^{+} ion (1.08 Å) is smaller than Ge atoms (1.25 Å) but similar to Se atoms (1.03 Å) [138]. The effect is clear from the simulation in Figure 4.12, which shows that only for Ge-rich glass $Ge_{40}Se_{60}$, Ge target vacancy was higher than for Se. This phenomenon plays an important role in irradiated crystalline films. Due to the amorphous nature of the glassy films, the effect of irradiation is not so prominent. But the crystalline films showed the effect of the irradiation clearly. Since Se can be displaced more than Ge due to the ion/atom size equality, it was expected that the Se-rich composition $Ge_{30}Se_{70}$ would be most affected by the irradiation. For this composition, two important factors interplay during the interaction with ions. On one hand, the structural stability of the Se-rich $Ge_{30}Se_{70}$ amorphous films – Figure 4.5 (a,b). This is mainly based on their floppiness [31], which allows an easy arrangement of the structural units during external stimuli by changing the angles under which the tetrahedra are organized without affecting the basic ratio of the structural units. On the other hand,

the cation-cation distance, in this case, is smaller than in the stoichiometric composition as revealed by XPS studies [139] and so the interaction with the Xe ions will be much stronger compared to the one with smaller ions, like Kr ions for example [140].

Figure 4.8 (a) shows that a very dominant peak of *orthorhombic* GeSe is present after irradiation with 200 keV ions. This is an indication of the formation of Se deficient structure. However, the GeSe peak is missing at irradiation with 600 and 1000 keV. In addition to having the smallest size of GeSe crystals compared to the other two compositions, this could also mean that the GeSe crystals form near the glass-substrate interface, and since higher energy ions penetrate further, these crystals are affected. The Raman spectra at these conditions exhibit well expressed ES structure formation. This indicates the presence of crystals with structure combining CS and ES building blocks, which is characteristic of the LT polymorph form of GeSe [135], [141]. It indeed has been registered on the XRD spectra (Figure 4.8 (a)) with growing crystal size as a function of the irradiation energy.

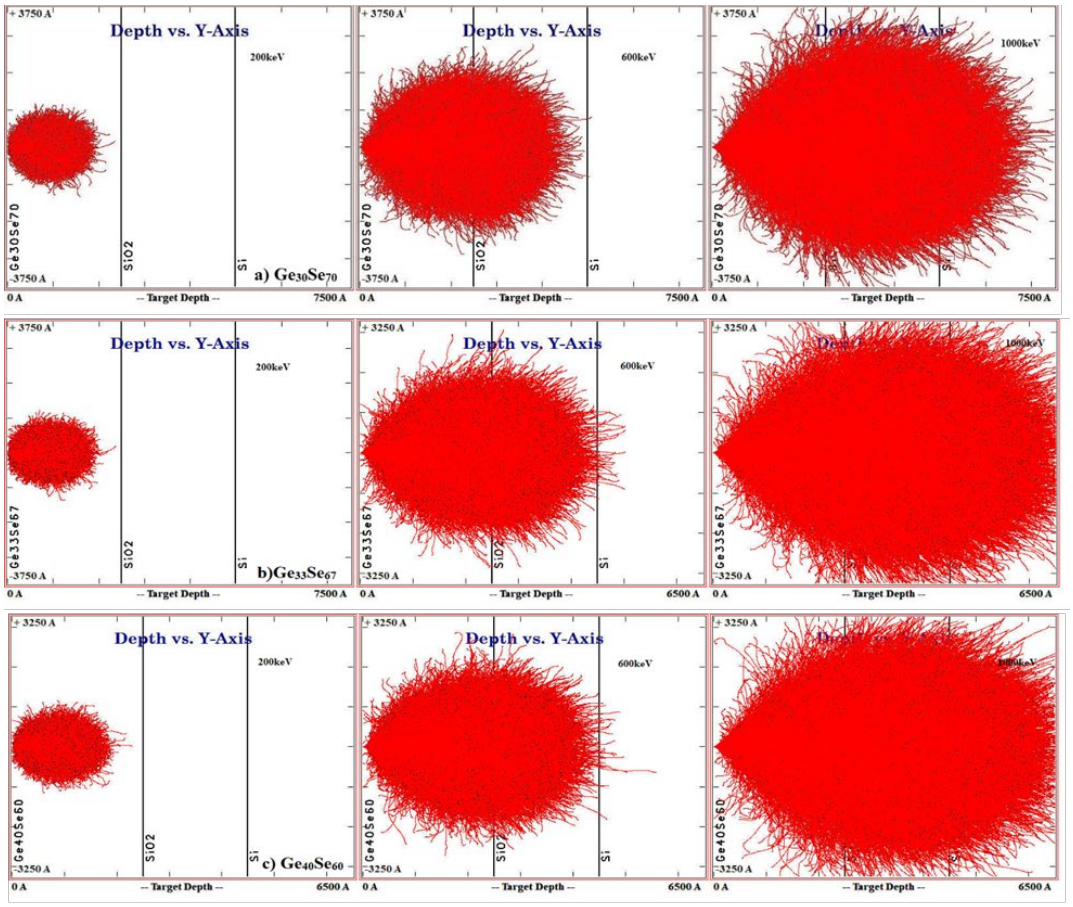

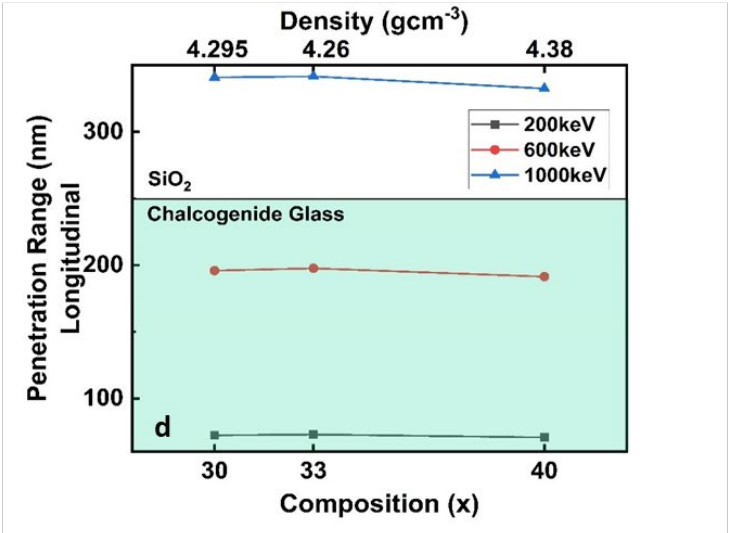

Figure 4.9 Ion penetration depth in chalcogenide glass (a-c) actual from simulation, (d) range.

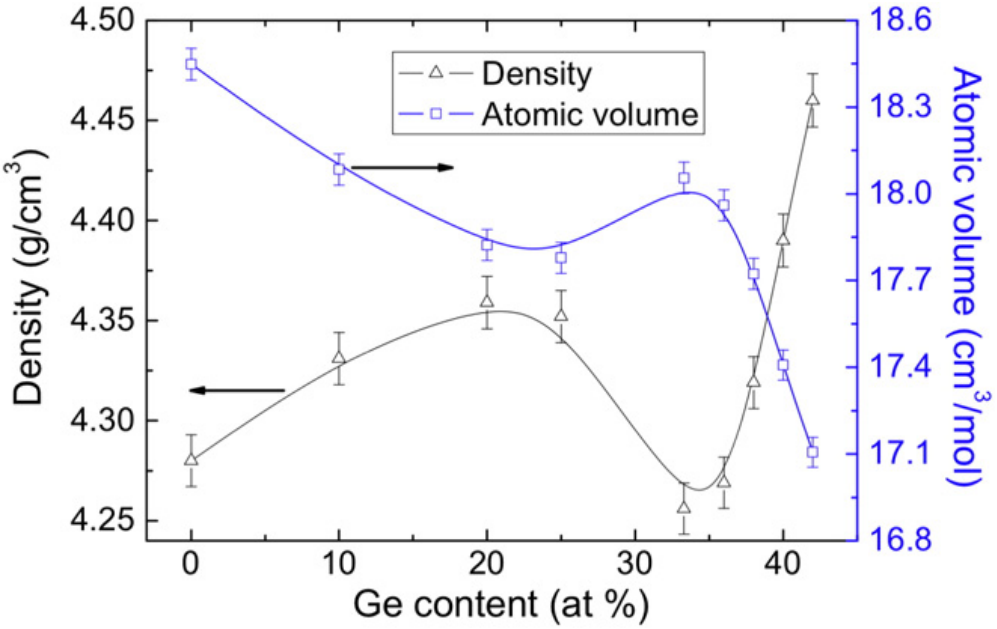

Figure 4.10 Composition vs density and volume [137].

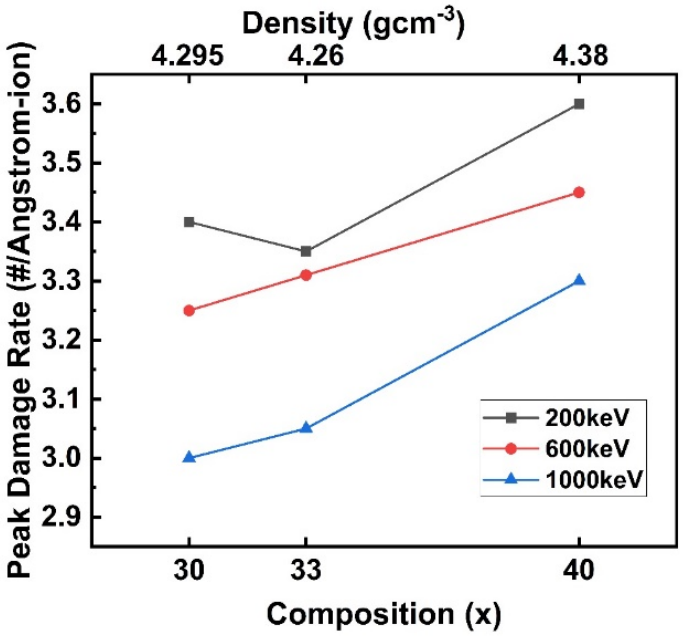

Figure 4.11 Peak damage rate vs. composition.

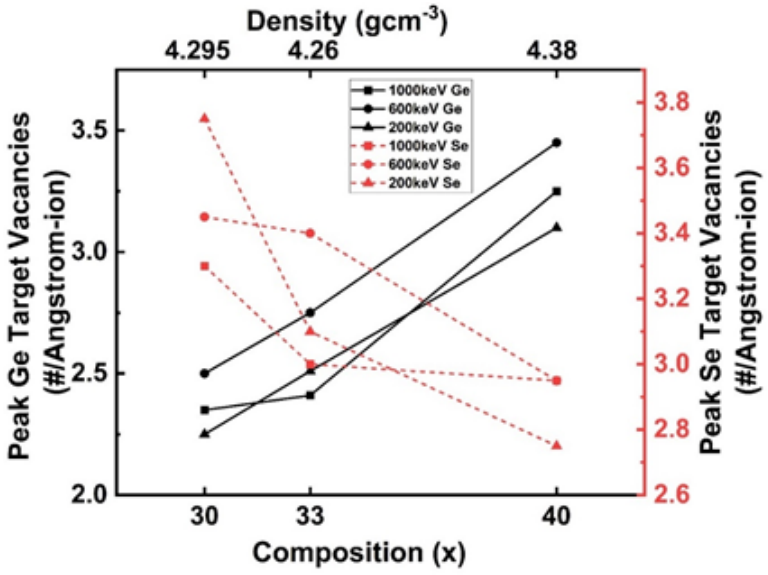

Figure 4.12 Vacancy produced in Germanium and Selenium atoms.

Regarding the $Ge_{33}Se_{67}$ composition, the interaction with the Xe ion affects mainly the Ge-Ge bonds (bond enthalpy 263.6 kJ/mol) [142] in the ETH structure and facilitates the reaction of the newly formed Ge dangling bonds with Se atoms from the Se chains. The irradiation with higher energy leads to phase separation and redshift of the tetrahedral breathing modes, giving rise to the appearance of the A_1 breathing mode at 200 cm^{-1}, characteristic for the LT phase of $GeSe_2$, [141] and well expressed Se-chain mode. It is important to note that in the crystalline phase, the A_1^C mode appearing at 218 cm^{-1}. Figure 4.6 (a) indicates the presence of ES tetrahedra and this structure is preserved during the irradiation. The predominant formation of hetero-bonding in the network explains the structural stability of this composition after irradiation, as presented in the Raman data – Figure 4.6 (b). Indeed, due to the Ge/Se ratio, which in the ideal case would lead to the formation of a particular number of only CS and ES tetrahedra, the structure of both – the amorphous and crystalline phases remain very stable during the irradiation with Xe ions after the Ge-Ge bonds collapse. This new structure occurring

after irradiation brings about formation after crystallization of LT GeSe – Figure 4.8 (b). We suggest that the formation is due to the interaction of the Ge-Se network with the Xe ions. Xe replaces some of the Se atoms and depletes the Ge-Se matrix of selenium as discussed for the Se-rich composition. A similar effect has been registered in [143] with increasing Ge concentration in the films. Here one more phenomenon needs explanation – the lack of formation of GeSe at irradiation with 600 keV. We suggest this is due to the reasons already explained about the $Ge_{30}Se_{70}$ composition, but in this case, there is a clear appearance of GeSe crystals at 1,000keV irradiation. The stoichiometric composition $Ge_{33}Se_{67}$ is the least dense among all the studied glasses - Figure 4.10. Nevertheless, its density is still higher than that of SiO_2 (2.27g/cm^{-1}) and Si (2.33 g/cm^{-1}) [144], [145]. So, there would be massive penetration of Xe ions which reach the Si substrate where repulsion of charged species can occur. It is for this reason that the Raman spectrum at the highest irradiation energy shows biggest damage of the amorphous structure – Figure 4.6 (b) and consequently forms Se-depleted GeSe crystals - Figure 4.8 (b).

The amorphous Ge-rich composition $Ge_{40}Se_{60}$ displays big structural stability, although the expectation was that the interaction with the Xe ions would be the strongest due to its closest packaging and highest density. However, Wang et al. [146] gave evidence that the Ge-rich structure is quite phase separated. As revealed by TRIM simulation – Figure 4.12, in Ge-Ge bonding, the interaction with the incoming ions would be limited because of the bigger size of Ge atoms and hence the lower density seen by the Xe ions. The networks beyond the chalcogenide film (the SiO_2 film and the Si substrate) reached by the ions with the energy of 600 keV and 1000 keV, respectively, provide channels for these ions because of their lower density. Hence, Xe ions interact only with

the higher density clusters in the chalcogenide glass matrix and escape to the lower density regions (SiO_2 and Si), affecting the chalcogenide network only at the highest energy used. Similarly, in the crystalline phase, unstable crystalline organization before irradiation is seen. But after irradiation, the structural organization is left unbroken even at the highest irradiation energy giving rise to LT GeSe crystalline in accordance with the results reported by Wang et al. [98]. Figure 4.12 shows that for this composition, the number of the Ge vacancies is much higher than the number of Se-vacancies which is an exception compared to the other compositions. Although from the chemical point of view, we consider $Ge_{40}Se_{60}$ as Ge-rich, from the atomistic point of view, there are more Se than Ge atoms in all regarded compositions. Moreover, Se is heavier than Ge, and it would have been more intuitive if Ge showed more vacancies at even $Ge_{33}Se_{67}$. We propose that for $x \leq 33$, the damage/vacancy is "size-dependent" and for $x \geq 33$, the damage is "mass-dependent". From - Figure 4.12, it is also evident that with higher density, we get higher damage. So, the whole ion-matter interaction is a multivariate, multiphysics problem that becomes much more complex when it comes to irradiating crystalline materials. In addition to all of these phenomena, surprisingly, the crystalline materials have been known to change to a different crystal phase after irradiation [147]–[149], and such transition is observed in our case. Experiments suggest that ion irradiation is also a stabilizing process for such a phase transition [150]. In this case, the main reason for this stability is that the ES structure requires less energy to form and their formation opens the structure [151], which reduces the opportunity for crystal damage by the incoming Xe ions.

Conclusion

Combined interaction with neutrons and γ rays creates some defects at low energies, which are not noticeable at high energies since due to fast recombination, the material keeps its initial structure. The effect of neutrons-only irradiation is subtle due to the reduced defects formation. The collected data presented here draw a complete picture of the application of Ge-Se chalcogenide glasses in a high-radiation environment as a temperature sensing material. From TRIM simulation, ion irradiation parameters are chosen to study the effect of chalcogenide glass, glass/insulator interface and Si substrate. This study reveals that irradiation with Xe ions, although introducing some small changes in the structure of the studied amorphous phases, they remain stable even at high irradiation energies. More expressed structural changes occur in the crystalline phases, which in the course of irradiation change their structure from LT $GeSe_2$ to LT GeSe. This stabilizes it and opens up the structure reducing the damaging effects in it. From XRD data, evidence of ion-irradiation induced crystal-crystal phase change in crystalline Ge-Se thin films is found. The emergence of Se-depleted *orthorhombic*-GeSe transition has been attributed to a complex interaction of Xe ion size, energy, density and temperature.

CHAPTER FIVE: ADDITIVE MANUFACTURING OF CHALCOGENIDE GLASSES

Additive manufacturing is one of the fastest developing industries since it offers compelling technology and an efficient device production process [152], [153], enabling roll-to-roll fabrication, which does not require cleanroom, photolithography and vacuum machinery. Moreover, the ability to print on any substrate type, including flexible substrates [154], [155], increases its application across electronics like the internet-of-things (IoT), wearables, sensing, and energy market. One other advantage of printing is that it can produce any arbitrary shape from a design file and the fabrication process is digitally controlled. So, printing is especially applicable to fabricate glass structures at a scale and complexity that were never possible before. However, most works utilizing such an advantage are focused on printing fused silica glass [156]–[158]. There are other types of glasses, like chalcogenide glasses (ChGs), used as optical components and for their electronic properties. Among the published works on printing ChG, the most studied are filament molding type printing and dissolution-based inks [159]–[161].

Inkjet printing is one of the most widely used technologies in the field of printed electronics and it usually requires nanoparticle ink preparation that is compatible with a specific printer. We studied the complete ChG printing process from glass synthesis to nanoparticle ink formulation and printing using a DMP-2850 Dimatix inkjet printer. Due to the lack of order, the atoms can be connected in many different configurations without stoichiometric restrictions.

So far, conventional deposition techniques like thermal evaporation, sputtering, or chemical vapor deposition have been used to fabricate the ChG thin films. There are reports in the literature on solution-based ChG film deposition techniques, such as spin-coating [162]–[165]. However, this method does not allow the formation of devices with specific dimensions and shapes without expensive and complex photolithography. Furthermore, the solvents used in ChG solutions are usually amines [166]–[168], which are highly toxic, corrosive and reactive. Usually, traces of these compounds remain in the deposited films and affect their properties. Considering digital printing of patterns using these solutions is not convenient since the amines react with the polymer housing inside printheads. This limits the application of so-produced inks due to the need to modify printers and the requirement of a controlled environment for safe handling of the material. Nevertheless, some publications report devices printing with amine-based chalcogenide solutions [161] using custom-made printers or syringe dispensation. New avenues must be explored to discover a better solution for applying additive technology for producing a wide range of electronic and optical devices based on ChG. Additive manufacturing would open enormous opportunities for device production in space or other prospects like direct devices printing over particular surfaces. In this respect, inks containing nanoparticles of ChGs are an unrivaled solution. While there are some reports in that field [169], [170], these inks have not been used in printers so far, and there are no reports regarding their capabilities for the production of electronic/photonic devices by printing.

This chapter investigates nanoparticle ink formulation of three glasses, the Se-rich $Ge_{30}Se_{70}$, the stoichiometric $Ge_{33}Se_{67}$ and the Ge-rich composition $Ge_{40}Se_{60}$ of the Ge-Se

system, demonstrate the formation of thin printed films produced from the ink and determine their use in the fabrication of electronic and photonic temperature sensors. We report data regarding the dependence of the size of the nanoparticles from the milling process and the essential characteristics of the formed inks, like contact angle and viscosity. The properties and crystallization processes of the printed films are compared to thermally evaporated thin films and discussed based on their compositional specifics. The change in material properties due to phase transition is measured by collecting electronic or optical signals and interpreted as a function of the printed films' specifics.

Chalcogenide Glass Nanoparticle Ink Formulation

Nanoparticle inks are prepared by crushing bulk glasses into nanoscale particles. Ge_xSe_{100-x} (x= 30, 33, 40), bulk glasses are synthesized by the process described in our previous work [171]. Bulk glassy material is crushed into smaller pieces using wet milling and ultrasonication, respectively, to make nanoparticles. The ink is essentially built by ChG nanoparticles suspended in a liquid. Here the liquid medium is cyclohexanone. In addition, a surfactant, here ethylcellulose, is added into the mixture to prevent particle agglomeration. Ethylcellulose readily dissolves in cyclohexanone, and the boiling point of cyclohexanone is high enough (155.6°C) to avoid drying nozzle during printing. So, to form an ink, a mixture of cyclohexanone, ethylcellulose and ChG powder is milled, ultrasonicated and centrifuged, respectively. The milled mixture comes out as a highly viscous liquid. Cyclohexanone is added before ultrasonication to make it less viscous. Once the process is finished, the concentration of the cyclohexanone and ethylcellulose is adjusted to make the mixture viscosity compatible with Fujifilm Dimatix Material Ink-Jet Printer (DMP-2850) and then the mixture becomes an ink. Moreover, the

ink drop's contact angle on oxidized-silicon substrate is measured to estimate the resolution.

Particle size is an essential characteristic, closely controlled during ink preparation. A dynamic light scattering (DLS) system was used to measure the particle size distribution. The inks and printed film quality were characterized by their viscosity, i.e., their potential to be ejected by the printer, the ink surface tension, and the surface energy of the substrate the inks are deposited on. Figure 5.1 shows a flow chart that describes the nanoparticle ink formulation process.

Results

The process starts with ball milling. It has the provision to control the temperature during milling. Using that temperature was kept below 50°C. Temperature control is imperative during milling as it prevents undesired crystallization of the nanoparticles. Figure 5.2 demonstrates that about 80 hours of milling at 1100 rpm provides the optimum particle size (~ 200nm) out of the ball mill. Further milling increases the particle size (~ 250nm) as the milling and coalescence co-occur during extended milling. During milling, ethylcellulose reduces particle agglomeration rate and wastage of material by precluding particle adhesion to the milling jar and milling balls.

Increasing the ball milling's rotational speed might pin down the balls, reducing the effect of milling over particles. Also, high speed yields a high temperature that might crystallize the nanoparticles [172]. Although the ball mill temperature control is a helpful option, it controls the milling jar temperature rather than the temperature of the local nanoparticles. Moreover, milling balls might break, and the residues might contaminate the sample [173]. The trial-and-error studies demonstrated that for $Ge_xSe_{100-x,}$ an 1100

rpm rotation speed produces the best result. The final particle size was about 200 nm. After ball milling, the mixture comes out with paste-like viscosity. Another 50ml of cyclohexanone is added to the paste to prepare a less viscous solution.

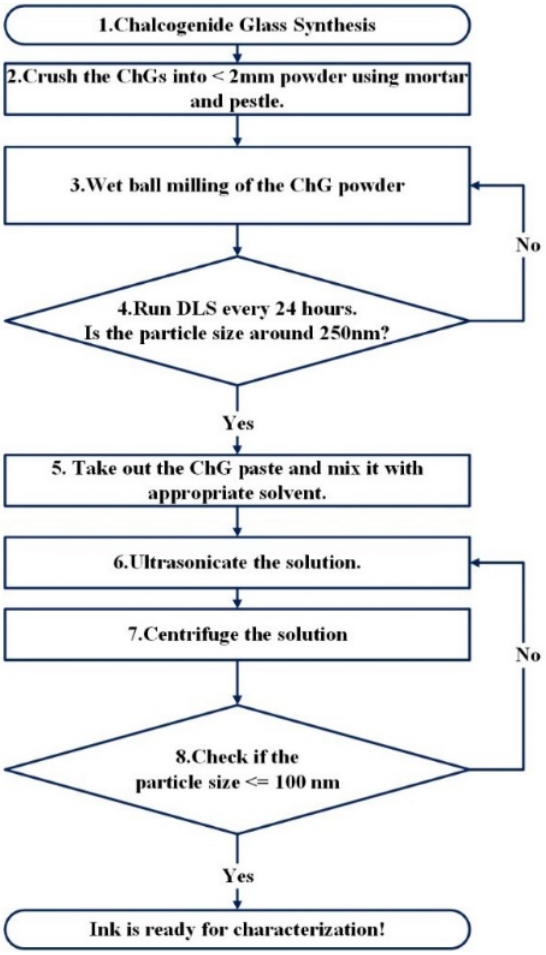

Figure 5.1 ChG nanoparticle ink formulation.

Ultrasonication is performed for 2.5 hours to reduce the particle size further and disperse chalcogenide glass in the mixture. As a result of ultrasonication, the DLS measurements demonstrated a considerable reduction in diameter to about 145 ± 20 nm.

Particle size uniformity in the mixture is achieved through centrifugation at 4500 rpm for 1.5 hours, leading to the segregation of particles with a diameter of about 100 nm.

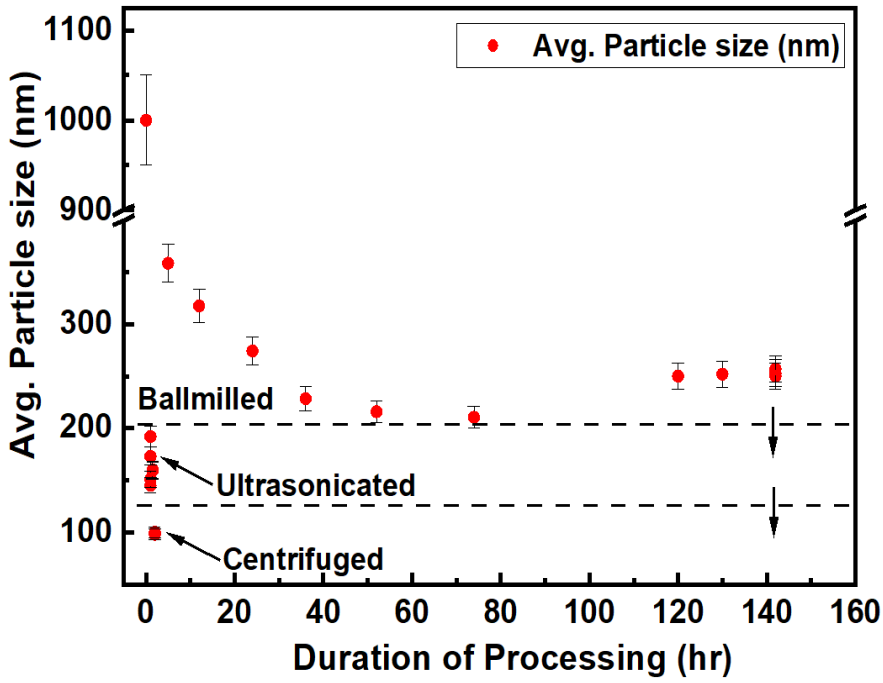

Figure 5.2 Particle size reduction of ChGs by combining Ball-Milling, Ultrasonication, and Centrifugation, respectively.

Once the particle size is around 100 nm, the viscosity of the mixture is measured. The viscosity of the mixture needs to be within 8-12cP to be compatible with the DMP-2850 printer. For final adjustment of the mixture viscosity, cyclohexanone and ethylcellulose were added to the milled mixture to prepare a compatible ink of viscosity 10-12cP.

After viscosity, the ink's contact angle with the substrate (oxidized Si) is measured, which is an indicator of the adhesion and the resolution that can be achieved with the ink. All three ChG compositions showed contact angle 10-15°, suitable for good surface wettability. The inks' final concentration was 0.15-0.3 g/ml ChG and 0.03-0.05g/ml ethylcellulose in cyclohexanone.

In the DMP-2850 printer, the printing was done using 3-5 nozzles. Nozzle voltage was between 20-30 volts. The drop separation was set at 20µm. Under such conditions,

100µm resolution was achieved. For characterization, 10 layers of 5cm x 5cm thin films were printed.

After printing, the printed films are wet and the nanoparticles are mixed with the surfactant. The printed films were dried for two days in a vacuum chamber at room temperature for the initial slow evaporation of cyclohexanone to avoid cracks formation. Once dry, the thin films were annealed at 350°C (the decomposition temperature of ethylcellulose) for 2-3 hours under nitrogen. Annealing sinters the particles and hardens the features forming solid printed films. After sintering, the printed films were characterized.

Printed Films Characterization

Surface roughness: The sintering duration and temperature causes macrostructural changes in the films and affects the films' surface roughness. The development of surface roughness as a function of the sintering time is presented in Figure 5.3. The surface roughness increases during the initial phase of sintering (30min of heating). However, further annealing does not influence the roughness much, and the curves display saturation, indicating that the sintering conditions are well satisfied. The curves in Figure 5.3 are produced by non-linear fit. R^2 values are for x=33 - 0.7551, x=30 - 0.74774 and x=40 - 0.7396.

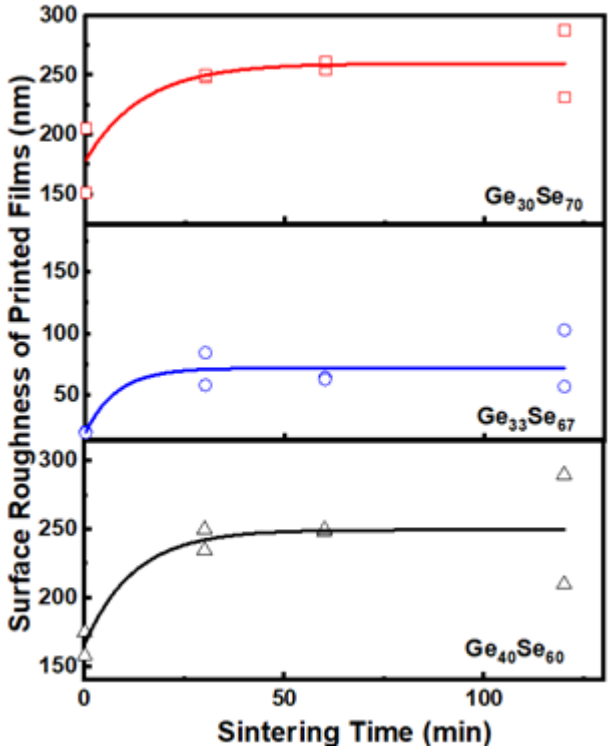

Figure 5.3 Average arithmetic roughness of the printed films as a function of sintering time.

Compositional analysis: Since the ink contains two components (Ge and Se) with different hardness, there is a concern about the films' composition and structural stability. Characterization of printed thin films by Energy Dispersion Spectroscopy (EDS) shows that, on average, the composition of 5 – 6μm thick films obtained by ten layers of printing is close to the source bulk glass compositions. Figure 5.4 presents EDS line scans data of the printed films. Although point EDS shows a 3-5% difference in composition compared to the bulk glass, the average of 500-1000 μm line scan has less than 1% difference in composition from the bulk material. The film's composition checked by line scans is close to the bulk material composition, which assures a good printed film composition control.

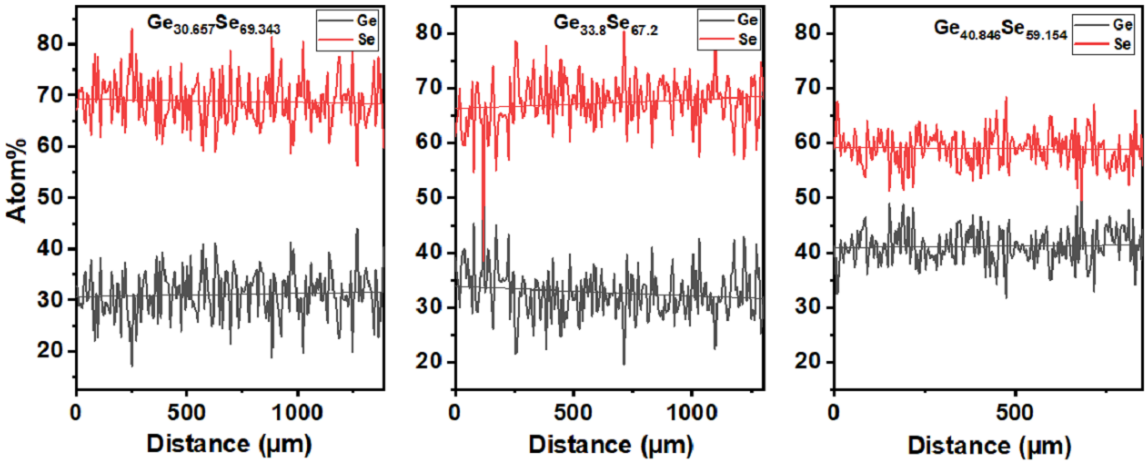

Figure 5.4 Line scan EDS of $Ge_{30}Se_{70}$, $Ge_{33}Se_{67}$ and $Ge_{40}Se_{60}$ printed films.

X-ray Diffraction Spectroscopy: Further film characterization has been done by X-ray diffraction spectroscopy (XRD). Although, films with 30 at.% and 40 at.% Ge were amorphous in nature before and after sintering, the stoichiometric films with 33 at.% Ge were crystalline before sintering.

After heating to their crystallization temperatures, the crystalline $GeSe_2$ phases appearing in printed films with x= 30 and 33 are difficult to distinguish. The strongest peaks are from either *orthorhombic*-$GeSe_2$ or *monoclinic*-$GeSe_2$. According to the JCPDS card 32-0410, *orthorhombic*-$GeSe_2$ shows the strongest peak near 14.93°, whereas the JCPDS card 30-0595 states that *monoclinic*-$GeSe_2$ shows the strongest peak at 14.99°. So, the *orthorhombic* peak is seen at a slightly lower angle than *the monoclinic.* In the printed films, in samples with x=30, the strongest peak was found at 14.96° and in those with x=33, at 15°. From the experimental results, it can be inferred that unlike thermally evaporated films [171], the x=30 thin films crystallize, forming *orthorhombic*-$GeSe_2$ and such with x=33 forms *monoclinic*-$GeSe_2$. However, a 0.04° difference in the

peak position could also be attributed to experimental error. Later the analysis of Raman data further enlightens the crystalline structure.

In addition, the samples with x=30 show the presence of GeSe crystals in the printed films, which could be due to phase separation occurrence since XRD also shows a well-documented presence of hexagonal Se crystals, as seen in Figure 5.5. On the other hand, the samples with x=40 display *orthorhombic*-GeSe, which agrees with the previous study [171]. As in the case for samples with x=30, for both printed and thermally evaporated films, for x= 33, 40 compositions, *hexagonal*-Se is present. XRD shows no evidence of GeO_2 or SeO_2. The latter is very volatile and if formed, it should evaporate during sintering which was carried out at a temperature higher than its melting temperature (315ºC) [174].

Raman Spectroscopy: The molecular structure of the films was studied by Raman spectroscopy – Figure 5.6 (a-c). The spectra of the printed films are compared to those of thermally evaporated (TE) films since it is known that the evaporated films closely resemble the Raman spectra of the bulk materials with the particular composition [175]. In essence, all electronic and photonic devices reported so far are based on thin films and in this aspect, comparison of TE and printed thin films data is a reasonable justification. Although all specific selenium and germanium containing tetrahedral structural groups (corner-sharing *CS*, edge-sharing *ES*, ethane-like *ETH*, and *Se-Se* chain) are present [97], [98], the Raman spectroscopy shows the difference in the structure of the printed, compared to thermally evaporated films. Since the samples with x=33 crystallized during milling-ultrasonication, they are discussed separately.

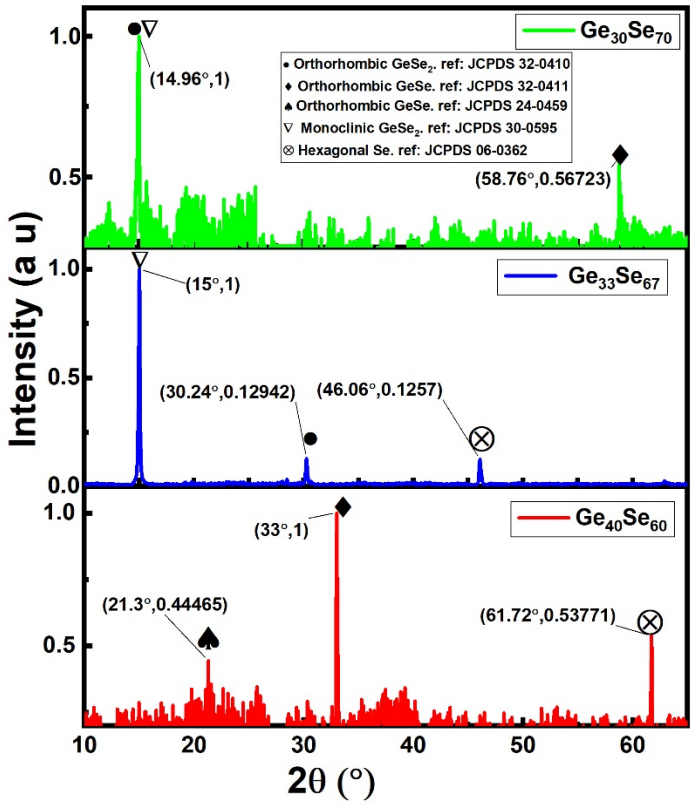

Figure 5.5 XRD of Crystalline phases appearing after annealing of the films to the glass crystallization temperature.

Printed films with x=30 show an increase in the *ES* structure, compared to the TE films– Figure 5.6 (a). Once they are sintered at 350°C for 30 min, printed films display similar structures as amorphous TE (a-TE) films. Further heating does not seem to affect their structural organization.

Compared to films with x=30, those with x=40 have shown better stability in terms of structural units – Figure 5.6 (c). As expected, printed films exhibit a lower number of *ETH* structures than TE films, and there is a considerable red-shift of the *CS* and *ETH* peaks. A critical aspect of the films with x=40 is that even the "as printed" films before further annealing have similar structures as a-TE film.

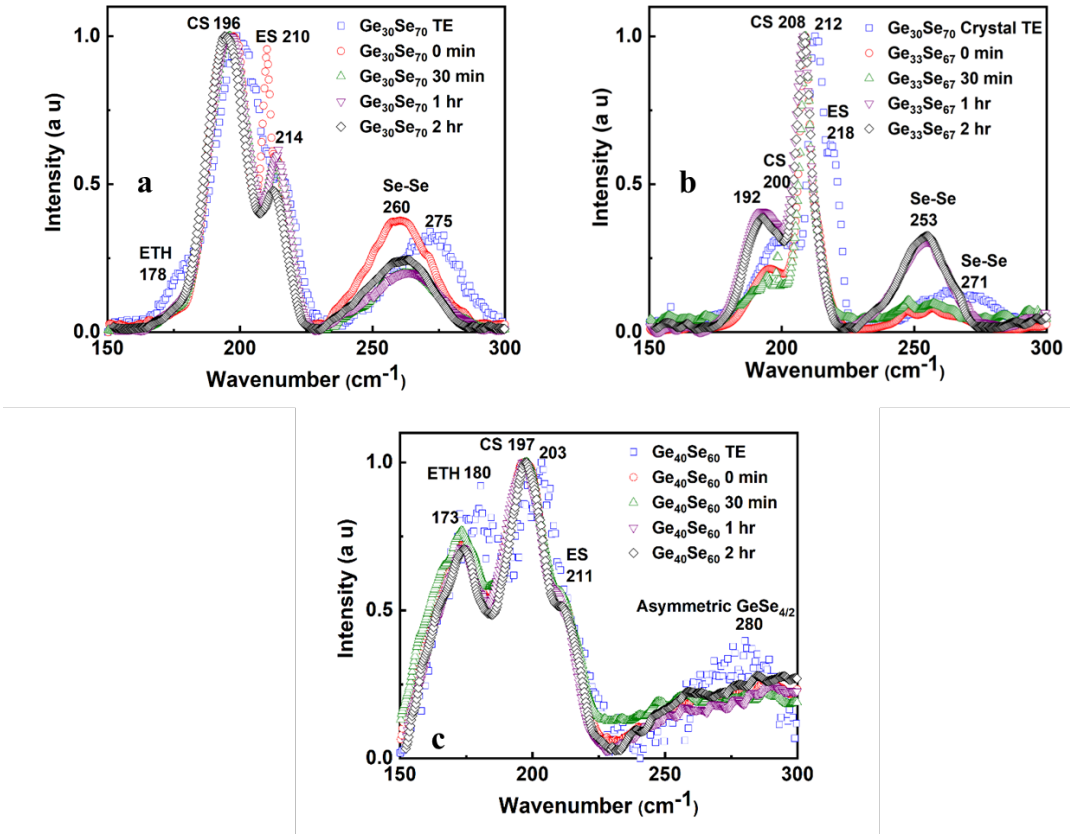

Figure 5.6 Raman Spectroscopy of Printed and Evaporated films a) $Ge_{30}Se_{70}$; b) $Ge_{33}Se_{67}$ c) $Ge40Se_{60}$.

Discussion

Surfactant-assisted ball milling has been studied in-depth to prevent particle agglomeration during milling [176]–[178]. Surfactants lower the surface energy of the fine particles during milling by forming a thin organic layer. The long organic tail of the surfactant prevents particles from coming in contact with each other. In this manner, it prevents the particles from agglomeration and cold welding that would substantially increase particle size during high-energy ball milling [179]. Concertation of the surfactant is an essential factor. For the ChG ink, 5% surfactant produces the best result. Although adding surfactant helps the milling, more than 5% concentration makes the thin films polymer-like and it reduces the adhesion to the substrate. Initially, the increasing of the

milling time reduces the particle size, as presented in Figure 5.2, any milling beyond 80 hours tends to increase it. These nanoscale particles have a high surface/volume ratio. The bigger surface area creates a high number of dangling bonds. The particles become highly chemically active. Such reactivity contributes to their interaction and formation of agglomerates. We suggest two additional reasons for the formation of larger particles after a longer milling process. First, the high collision frequency between particles and grinding media reduces the surfactant's molecular chain to an average shorter length, thus decreasing the steric hindrance. Second, the high collision activity of the particles induces cold welding during the high-energy milling. These two steps produce a large mean agglomerate size in long-time milling [180].

One of the significant challenges during the ink preparation-printing-sintering is the likelihood of oxides formation. However, their presence was not detected by the Raman and XRD studies, and they did not affect the performance of the device based on printed films. One can expect that the milling process as described could lead to particle crystallization. The temperature control of the ball mill can be better maintained by reducing milling speed and by intermittent milling. Since reducing milling speed will produce larger particles, intermittent milling was done (30min ON – 30min OFF). There are data [181], [182] that milling might further amorphize the material due to the mechanical stress over the crystalline structure. Besides, since the heat generation occurs fast and is localized, it might dissipate at an equal rate. Such a phenomenon emulates the "melt-quenching technique" that is used for glass formation. So, milling at the described conditions is expected to result in crystal-free glass nanoparticles as revealed by the Raman and XRD studies for the $Ge_{30}Se_{70}$ and $Ge_{40}Se_{60}$ samples. However, the crystalline

structure has been found in the as-printed films of stoichiometric composition $Ge_{33}Se_{67}$. Interestingly, as we found out in our earlier study [173], this material undergoes homogeneous crystallization, which requires more energy than the heterogeneous process characteristic for the non-stoichiometric compositions. The milling introduces enough energy for the crystallization to occur. Since, in this case, the number of the wrong Ge-Ge and Se-Se bonds is minimal, and the requirement for the lower enthalpy for this composition is critical, crystallization dominates. For this composition the lowest glass forming ability has been formulated as well [173].

Moreover, printed crystallized x=33 thin films show similar Raman spectra of thermally evaporated crystallized x=30 thin films. Ball-milling introduces phase separation in the nanoparticle, which in turn changes the crystallization kinetics of x=33 from homogenous to heterogeneous. In addition, Figure 5.4 shows x=33 thin films are slightly Se-rich. We suggest that both Se-rich nature and phase separation dominates the crystallization of printed x=33. As a result, the crystal phases are different than for TE thin films of x=33.

As pointed out in the XRD results – Figure 5.5, it is not easy to decide which polymorph form of $GeSe_2$ has crystallized. The Raman studies of the material with x=33 *CS* at 208-212 cm^{-1} indicate the formation of *orthorhombic*-$GeSe_2$ [98] and *CS* at 192-200 cm^{-1} suggests the formation of *monoclinic*-$GeSe_2$. So, from Raman spectroscopy, we can infer that the peak at 15° in samples with x=33 Figure 5.5 is from *monoclinic*-$GeSe_2$.

From an application point of view, printed features with a similar material structure as the bulk glass or thermally evaporated films are essential. The scope of this dissertation is confined to the study and comparison of printed and TE films. Although all

specific germanium-containing tetrahedral structural groups (CS, ES, and ETH) are present [171], the Raman spectroscopy shows two significant differences between printed and TE films. The first is related to the reduction or absence of *ETH* structural units around 178 cm^{-1} [97] in printed films before temperature annealing. ChGs are chemically disordered [183] materials, which means there is a presence of wrong bonds like Ge-Ge and Se-Se. Ideally, in samples with x=30, Se-Se bonds are expected since they are Se-rich. But the presence of Ge-Ge bonds is widely accepted for this composition as well due to the disordered character. However, Ge-Ge bonds are weakest compared to Ge-Se and Se-Se bonds. So, we suggest Ge-Ge bonds break during the milling.

Second, there is a red-shift of the *CS* and *Se-Se* peaks in the printed films. The effect is much more prominent in the *Se-Se* peak (almost 15cm^{-1}). *CS* peaks seem to undergo red-shift with sintering duration. Although ultrasonication uses sound waves of wavelength in cm scale, such stress causes change at Å scale. Adding mechanical stress and high pressure during milling introduces additional distortion of the bonding [184]. Compared to the TE films, in all printed films, all the peaks demonstrate a red-shift, which should be related to the material being Ge deficient [97] except *ES* in samples with x= 30. As Figure 5.3 shows, samples with x=30 and 40 are a bit Ge-rich than corresponding bulk materials. However, we suggest that there could also be another mechanism dominating the peak position other than the composition. It has been reported that when a material undergoes tensile stress, the chemical bonds might get elongated relative to their unstressed state [184]. As the bond length increases and the force constant remains the same, it is expected that the vibrational frequency will decrease. During nanoparticle formation from bulk, printing and sintering, the material is subjected

to various mechanical stresses. Stress in the material and composition effectively influences the Raman peak positions, causing a red-shift and is the reason for the difference in the crystalline phases occurring after annealing of printed films. This effect also demonstrates the multifaceted character of the mechanical interactions in ink formation during milling and printing, unlike the one-directional pressure effect, which compresses interatomic bonds and causes a blue-shift to the vibrational modes due to anharmonic effects [37].

The sintering time is also a factor influencing the films' structure. For example, the missing *ETH* structure, especially in the Se-rich films, stabilizes with increasing the sintering time. A similar effect is characteristic of the edge-sharing structures and selenium chains. The Ge-Ge bond has the lowest bond strength in the studied system, and its presence is mainly affected by the milling process. For this reason, the Ge-Ge bonds have a relatively limited appearance on the Raman spectra of the printed chalcogen-rich films. Regarding the stoichiometric composition, which initial crystalline structure is based mainly on *monoclinic* $GeSe_2$, the long-term annealing relaxes the material through phase separation by which wrong bonds Ge-Ge and Se-Se dominate the structure. The Raman spectra improve and manifest structure closer to one of the TE films with the increase in sintering time due to decomposition of all additives used to form the ink and structural relaxation. This brings the material to its equilibrium condition and stable structure. A similar result has been submitted by Slang et al. [185] for As-S films obtained through the dissolution of ChG. It should be noted here that the post-processing mechanism of spin-coated films, prepared using dissolved glass and nanoparticle ink printed films, is different, although they both involve annealing. Spin-coated films

require low-temperature annealing to evaporate the solvent, which has a low boiling temperature. In nanoparticle films, the sintering must be carried out at a higher temperature to decompose surfactants and, in some cases, to melt the nanoparticles. These specifics of the sintering have been reported for dissolved As-S glasses [164] and As-Se glasses [186], [187]. However, the sintering process negatively affects the films' surface roughness, as shown in Figure 5.3. We suggest that this results from particles' agglomeration and reduction of film thickness after evaporation of the solvents and decomposition of surfactant [188].

Conclusion

In summary, we describe a nanoparticle ink formulation method of chalcogenide glasses that is compatible with the DMP-2850 printer and can also be applied by dip-coating. The process has been successfully applied to produce 100 nm Ge_xSe_{100-x} nanoparticles and by modifying additives concentration, DMP-2850 compatible inks were prepared, which have been able to print as low as 100µm features. The printed thin films were characterized and it was found that $Ge_{33}Se_{67}$ nanoparticles crystallized during milling. $Ge_{30}Se_{70}$ and $Ge_{40}Se_{60}$ printed films have molecular structure and composition, like these of the thermally evaporated films. XRD showed, once crystallized, printed films with x=30 and x=40 form *orthorhombic* structures. The printed thin films will be used to fabricate temperature sensors, proving that the printed films' crystallization temperature is the same as the thermally evaporated films.

CHAPTER SIX: DEVICE FABRICATION AND CHARACTERIZATION

The previous chapters reported how Ge-Se ChG material properties change because of crystallization and their behavior under irradiation. Change in resistance due to crystallization/phase change is the basic mechanism of phase change memory devices (PCM). There are established SET/RESET using different electrical pulses. In the SET state, the devices exhibit higher conductivity and in the amorphous or RESET state, their conductivity is lower. The same change in conductivity can be utilized to measure temperature. In the sensor mode, the device will be SET by heating/ambient temperature, and using electrical pulses, the device will be RESET. Next are presented the device structure, operation and performance of such devices.

Electronic Devices

Thin Film Temperature Sensor-Lateral Structure

A schematic of an electrical temperature sensor is shown in Figure 6.1. The device has a very simple structure where an aluminum or nickel electrode is thermally deposited/printed over a thermally deposited/printed layer of ChG. The effective current path (~1mm) is exposed in this structure, so this structure is better suited to study the effect of irradiation on the electrical properties of the ChG. Once the devices are in SET condition, they can be RESET by using electrical pulses.

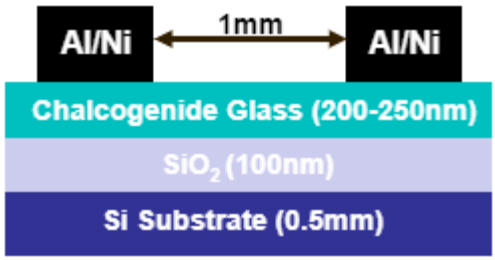

Figure 6.1 Temperature Sensor-Lateral Structure.

Operation

When T < T_c: Electrical resistance will be high since the material is in an amorphous state. So, when measured, the current will be low in this state.

When T > T_c: At this temperature, a drastic change in resistance will be observed. So, the device will go to the SET condition. Using electrical pulses, the device could be RESET.

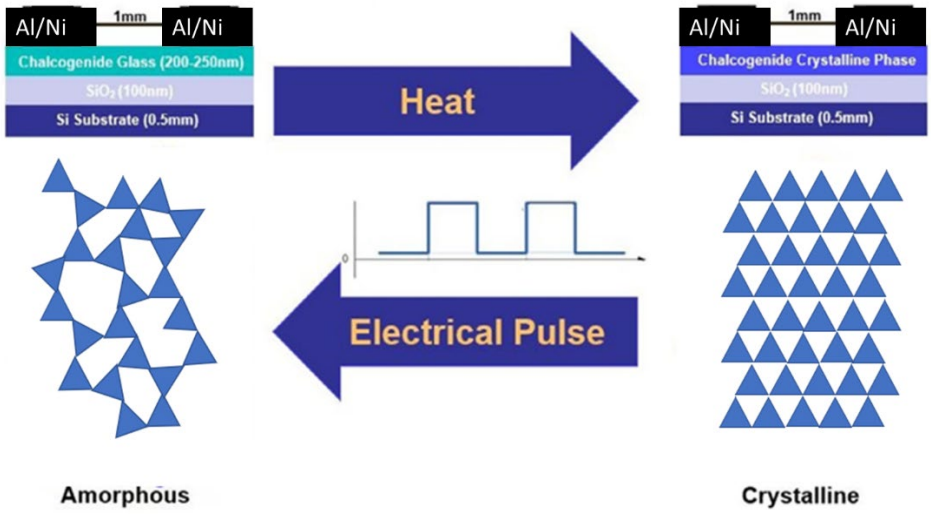

Figure 6.2 Lateral Structure Device Operation.

Thermally Evaporated Device

Device Characterization

Ge-Se devices were heated up to their crystallization onset temperatures to trigger the occurrence of a measurable current change at the onset. $Ge_{30}Se_{70}$ Device was heated up

to its crystallization onset 441°C and SET state was achieved. Up to 430°C, the amorphous devices didn't show any distinctive changes in current. In the amorphous state, the current is in 10^{-12} A and at the SET state current is in the 10^{-5} A range. With a 12 V voltage pulse for 10min, the device was RESET (Period 8µs, ON time 45ns).

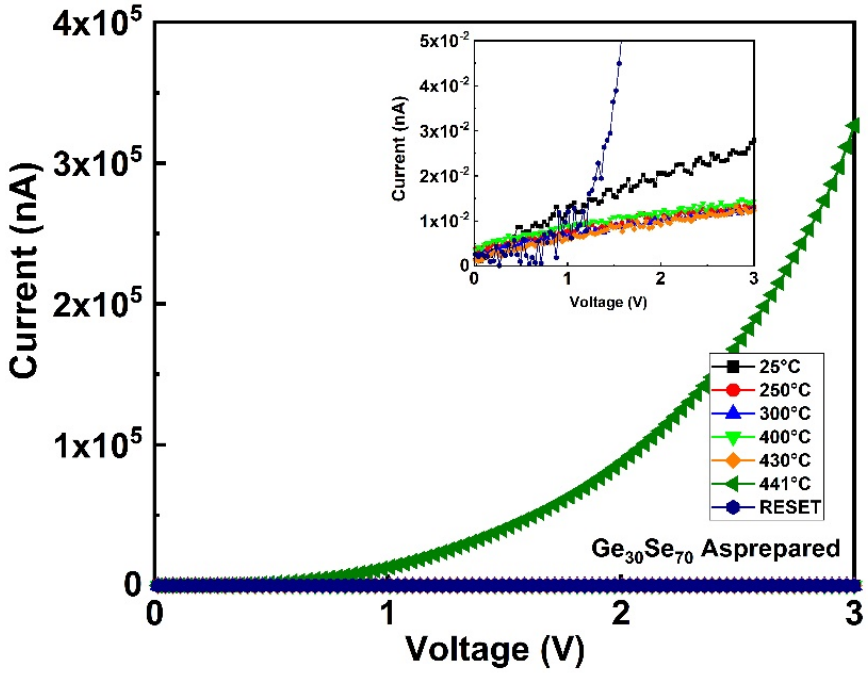

Figure 6.3 Performance of $Ge_{30}Se_{70}$ chalcogenide glass electrical sensor heated at different temperatures.

TEM studies confirmed the reversibility achieved by the pulsing. FIB lamella was prepared the ChG in between the electrodes. Small Area Electron Diffraction (SAED) demonstrates the presence of a crystalline structure. Figure 6.4 shows the amorphous nature of the as-prepared device, which is amorphous. Next, Figure 6.5 represents the SAED pattern of crystalline structure since the device was thermally crystallized.

The thermally crystallized device is considered to have completely crystallized material. For a such device, after electrical pulsing SAED, shows no existence of crystallinity (Figure 6.6).

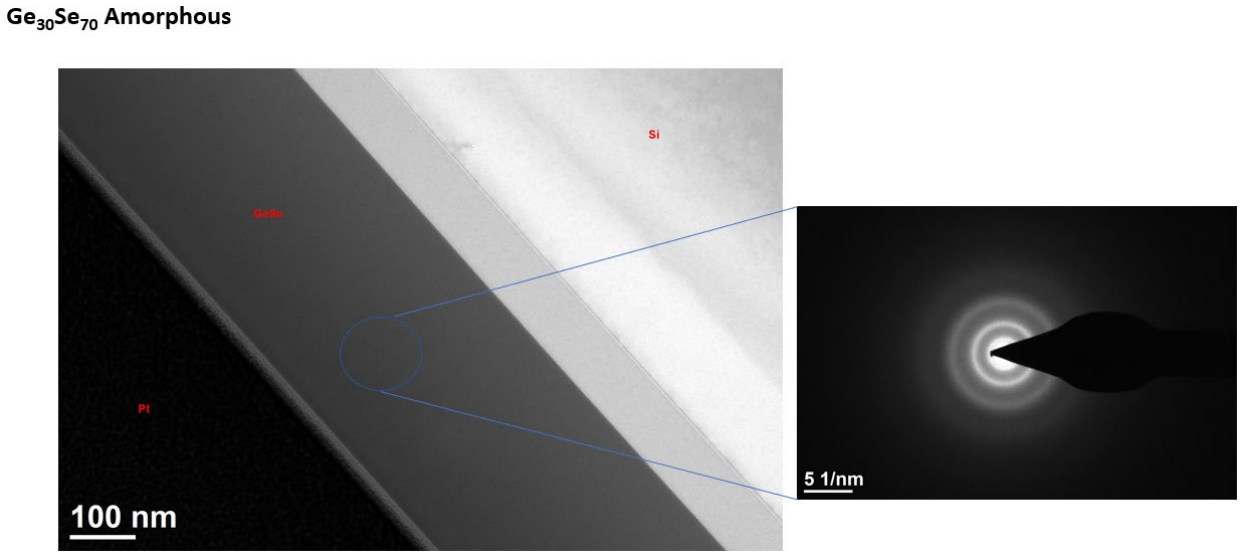

Figure 6.4 $Ge_{30}Se_{70}$ chalcogenide glass SAED in amorphous phase.

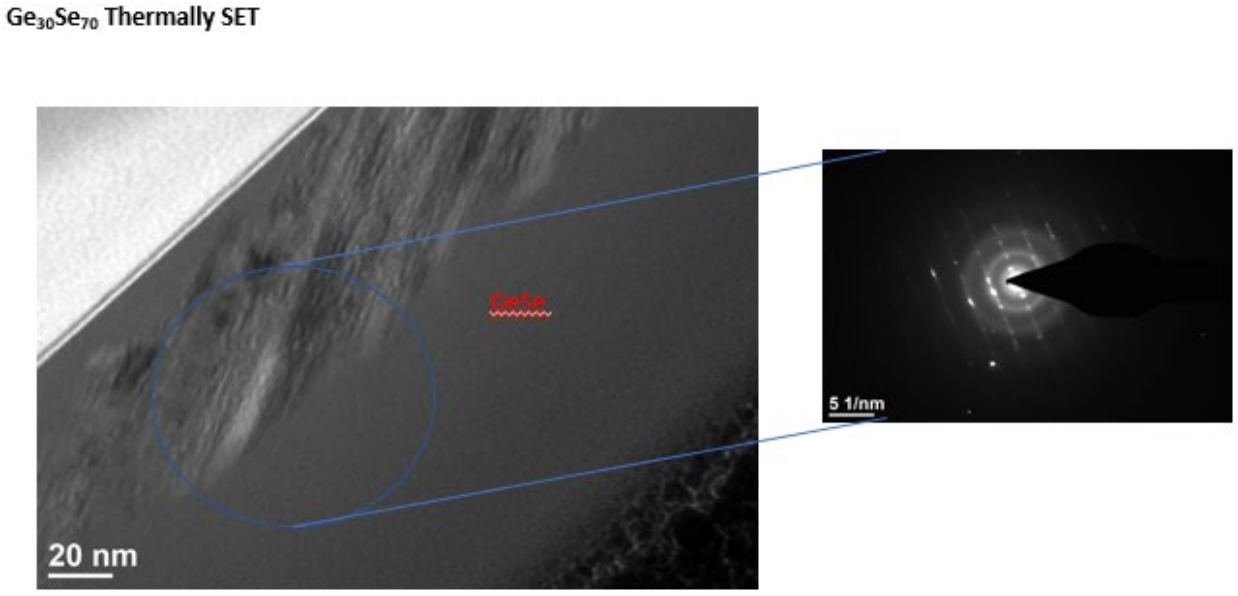

Figure 6.5 $Ge_{30}Se_{70}$ chalcogenide glass SAED after thermal crystallization.

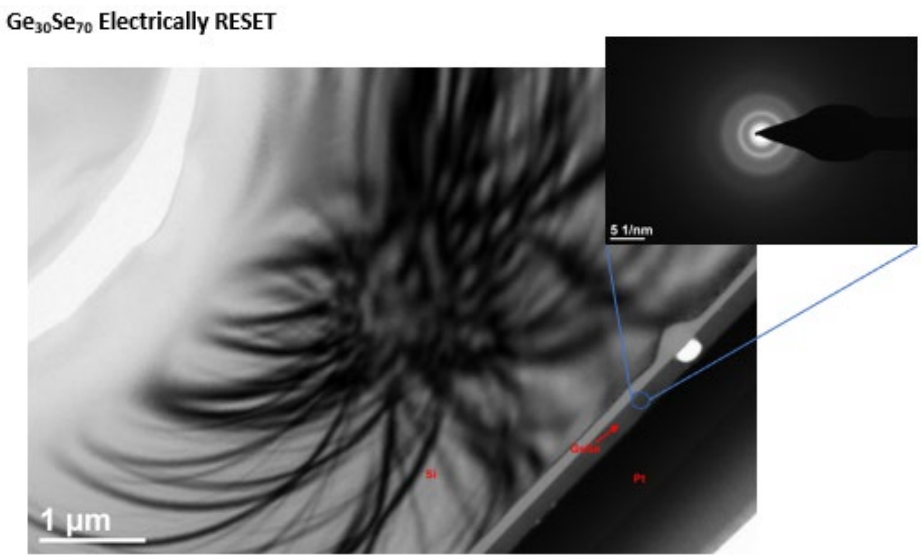

Figure 6.6 $Ge_{30}Se_{70}$ chalcogenide glass SAED after pulsing.

$Ge_{33}Se_{67}$ is the stoichiometric composition, so it has the least number of defects. This process also requires high energy for nucleation and growth since, in this case, a homogeneous crystallization occurs. So, when heated up to its onset temperature, the device didn't show much change in current. When it was heated to its peak crystallization temperature, the device was in the SET state and displayed a high current. Avrami exponent indicates that the crystallization process is much slower in this composition due to the homogenous crystallization. In the amorphous state, the current is in 10^3 nA and at the SET state current is in the 10 nA range.

After 20min of pulsing with different pulse-width and up to 20V, we failed to achieve reversibility. Among the three compositions, $Ge_{33}Se_{67}$ confirms the lowest current at the SET state. Since amorphization is based on the Joule heating of the material, due to its high resistivity even in the crystalline state, the material is difficult to amorphize.

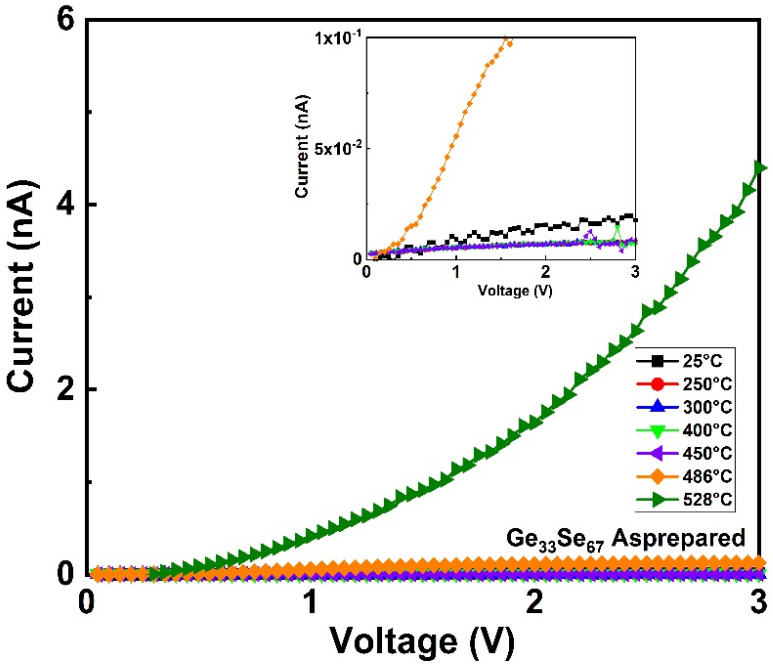

Figure 6.7 Performance of $Ge_{33}Se_{67}$ chalcogenide glass electrical sensor heated at different temperatures.

$Ge_{40}Se_{60}$ devices were heated up to their crystallization onset 447°C and low resistive state was achieved. Avrami exponent indicates that the crystallization process is fastest in this composition and heterogeneous crystallization occurs. In the amorphous state, the current is in 10^{-12} A and at the SET state current is in the 10^{-7} A range.

Unlike $Ge_{30}Se_{70}$ and $Ge_{33}Se_{67}$, $Ge_{40}Se_{60}$ devices exhibit a bit of crystallinity after pulsing, although after pulsing at 15V (Period 8µs, ON time 45ns) for 20 min, the I-V characteristic reveals that current has come down. As $Ge_{40}Se_{60}$ crystallizes in various Ge-Se phases, each phase may have a different thermal coefficient and melting temperature. So some form of crystallinity might be there even though the resistance has gone up.

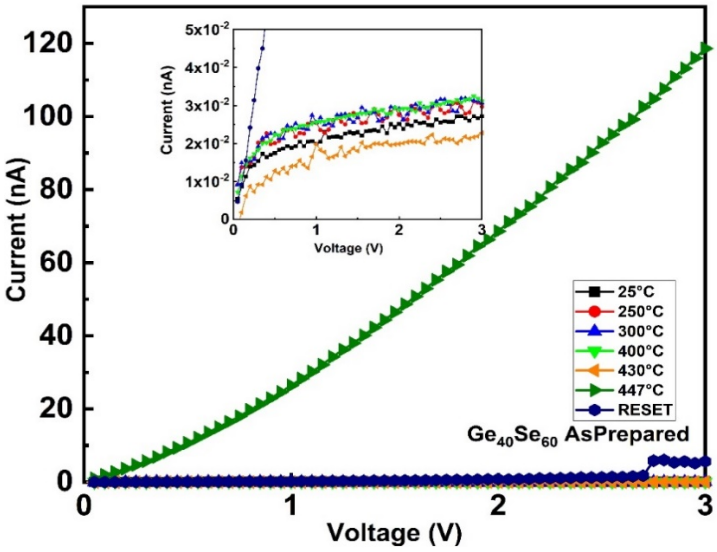

Figure 6.8 Performance of $Ge_{40}Se_{60}$ chalcogenide glass electrical sensor heated at different temperatures.

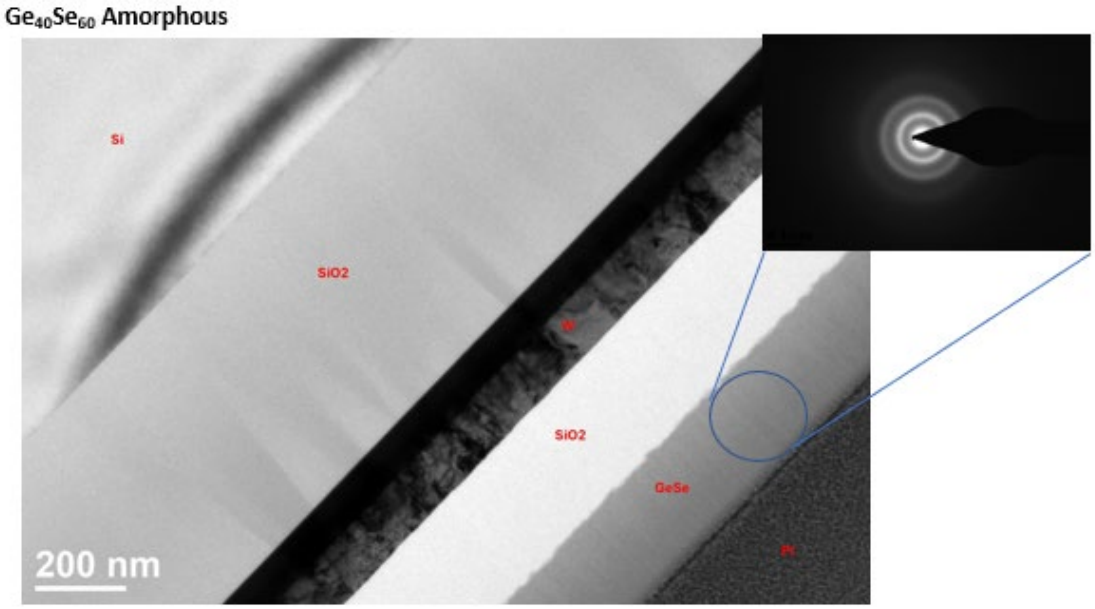

Figure 6.9 $Ge_{40}Se_{60}$ chalcogenide glass SAED in amorphous phase.

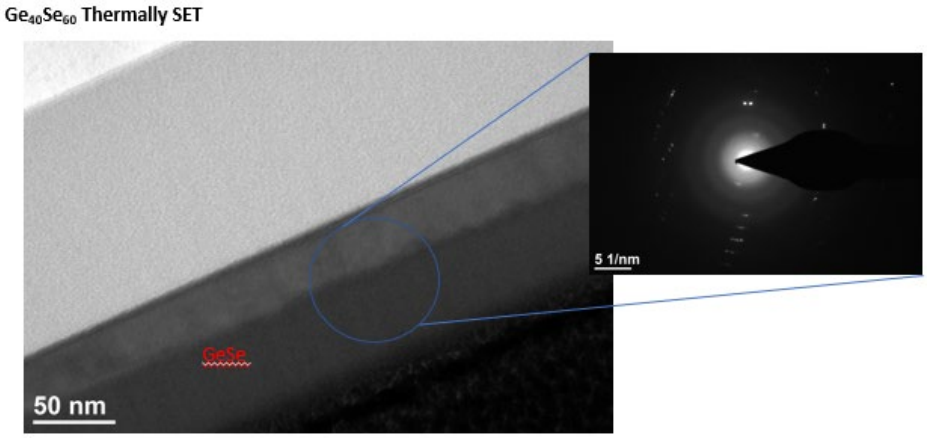

Figure 6.10 $Ge_{40}Se_{60}$ chalcogenide glass SAED after thermal crystallization.

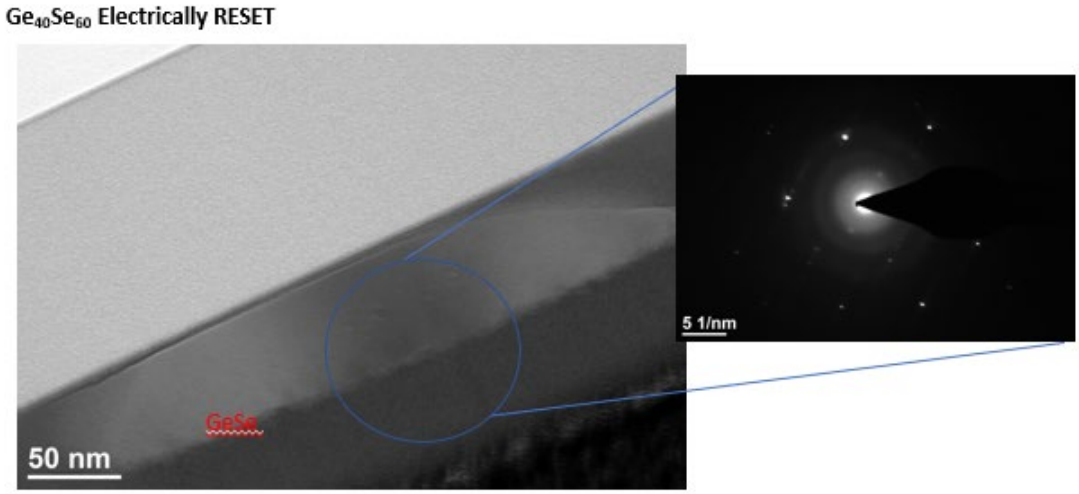

Figure 6.11 $Ge_{40}Se_{60}$ chalcogenide glass SAED after electrical pulsing.

Thermally Evaporated Device- Under irradiation

To study the effect of irradiation on the device performance, devices with Ge_xSe_{100-x} and Ge_xS_{100-x} (x=30,33,40) compositions were irradiated with Xe ions, similarly to the thin films irradiation to compare the devices response to iradiation. The effect of structural damage on the electrical properties of the devices in their amorphous phase and their SET state. After irradiation, amorphous devices were heated up to their corresponding SET

temperatures to see the effect of crystallization. Once they are SET, electrical pulses were used to RESET the devices.

Device Characterization

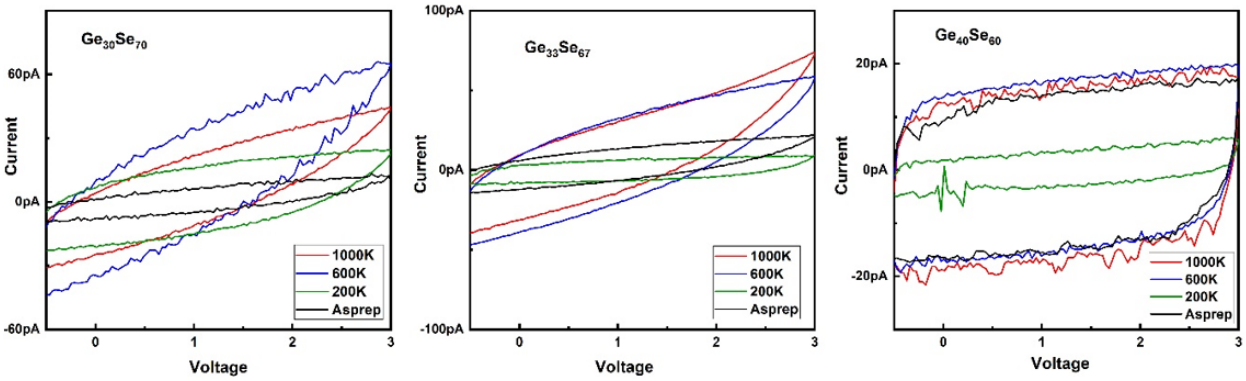

Figure 6.12 Performance of Ge-Se chalcogenide glass electrical sensors after different irradiation energy (200, 600 and 1000 keV).

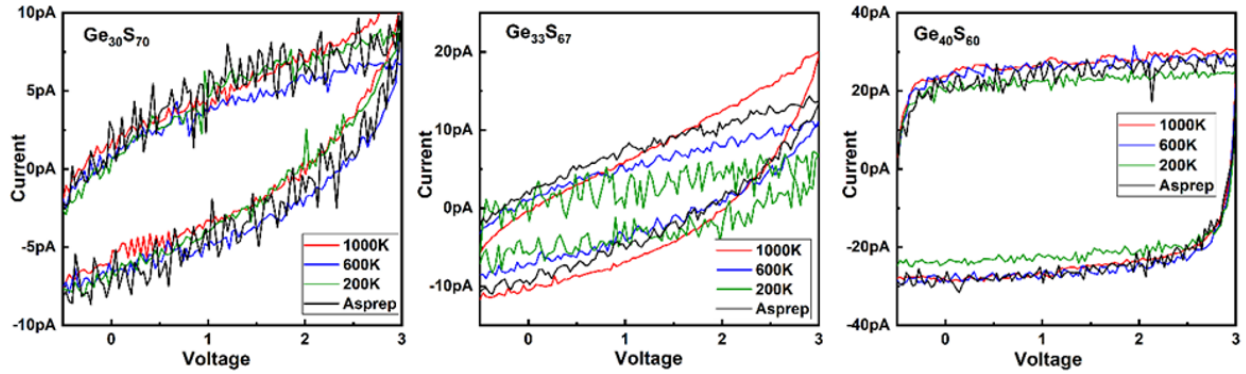

Figure 6.13 Performance of Ge-S chalcogenide glass electrical sensors after different irradiation energy (200, 600 and 1000 keV).

The devices were characterized by sweeping voltage from -0.5V to 3V, back and forth. The graphs show that the ChGs can be considered insulator/dielectric when they are in the amorphous phase, so the devices can be considered capacitors. The current is in the order of pA. For both Ge-Se and Ge-S systems, when x=40, the devices are fully charged under 1V. Variation of current due to irradiation is negligible when the devices are in the

amorphous phase. So, it can be deduced that 5 DPA does not have a distinctive effect on the devices.

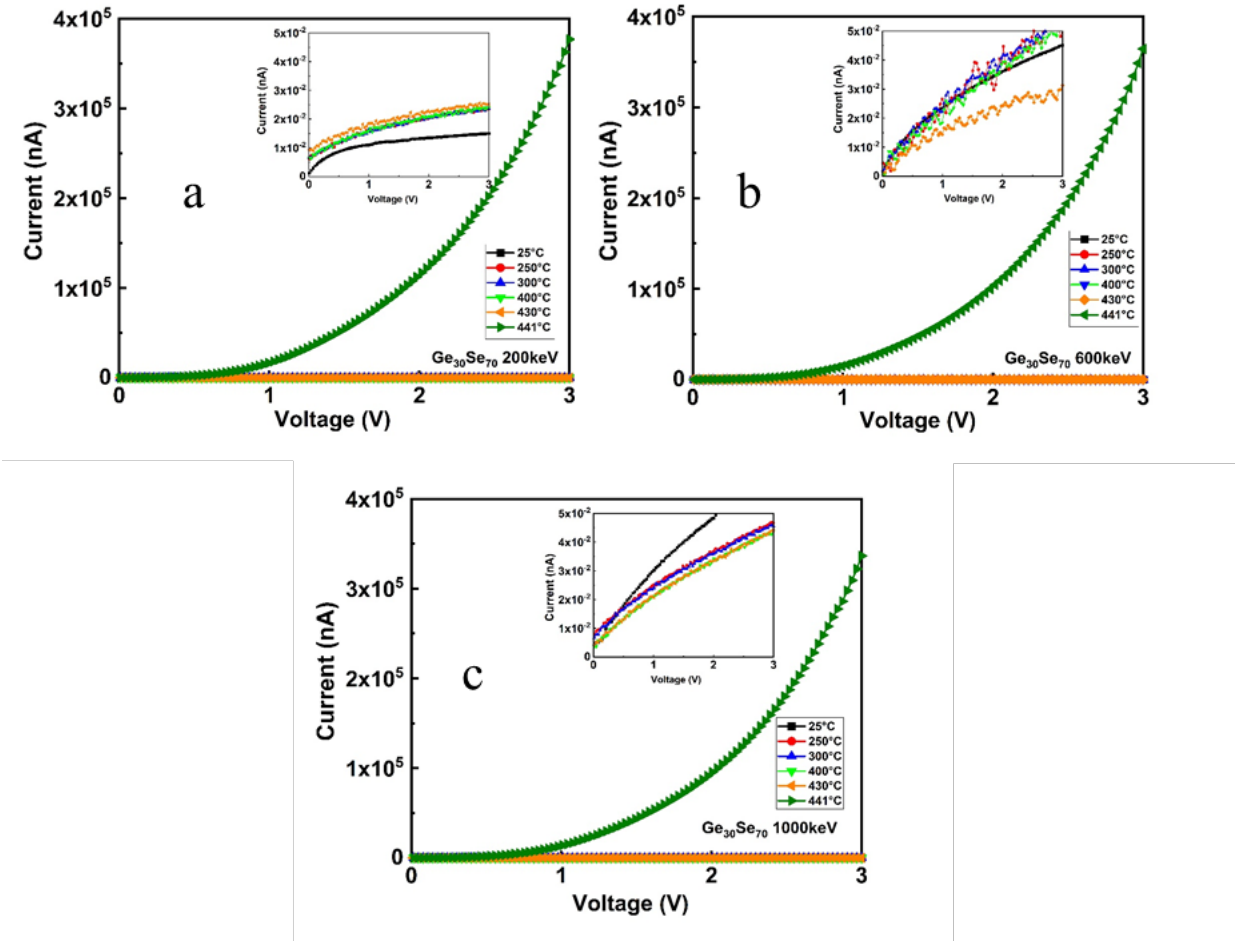

Figure 6.14 Performance of $Ge_{30}Se_{70}$ Device Characterization after irradiation a) 200keV b) 600keV c)1000keV.

To ensure reliable operation of the devices, SET devices were irradiated with Xe ions of 100, 400 and 700keV (damage 10 DPA). The energies are chosen so that the interaction of the ions mostly takes place in the ChG thin film and film-substrate interface, according to our research presented in chapter 4. Figure 6.17 (a) and (b), x=30,33 showed that the I_{on}/I_{off} is of the same order magnitude before and after irradiation. Our previous

study showed that these two compositions are not affected by the Xe ions due to low density.

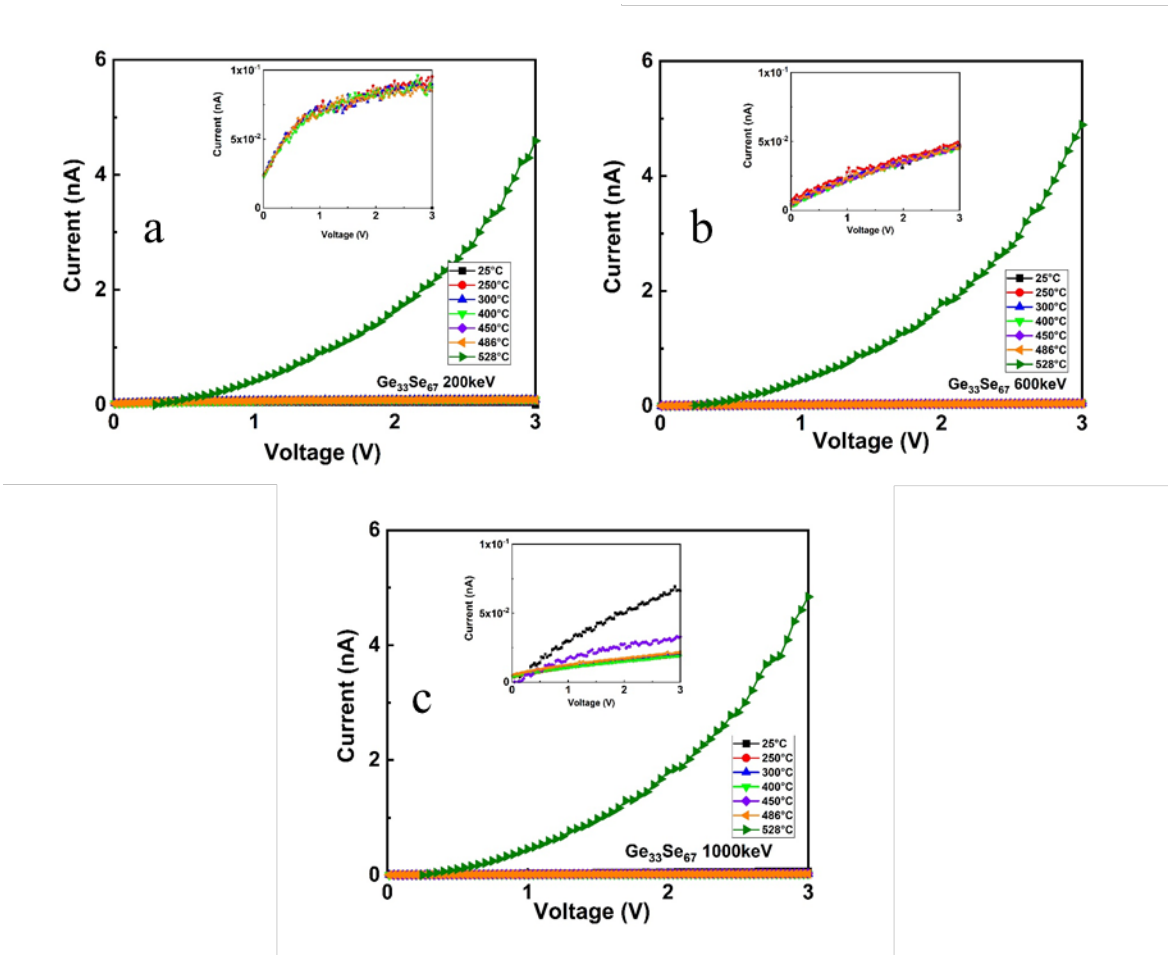

Figure 6.15 Performance of $Ge_{33}Se_{67}$ Device Characterization after irradiation a) 200keV b) 600keV c)1000keV.

In Figure 6.17 (c), x= 40 presents a reduction in current after irradiation. Although 100 and 400keV ions are found to be impacting the device negatively, 700keV ions don't seem to affect the IV characteristics. We suggest this is because the 100 and 400 keV ions interact the most with the surface of the ChG thin film, on the other hand, 700keV ions easily pass through the ChG layer and interact at the interface.

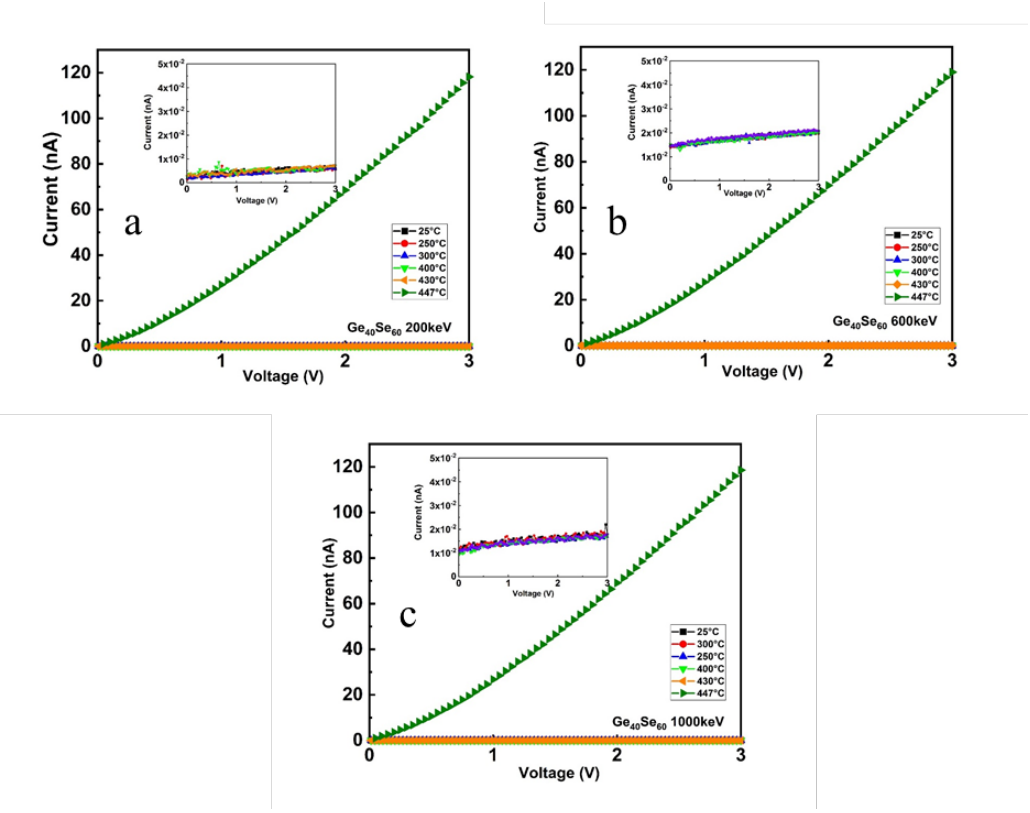

Figure 6.16 Performance of $Ge_{40}Se_{60}$ Device Characterization after irradiation a) 200keV b) 600keV c)1000keV.

Inkjet Printed Devices

These devices have a similar structure as the TE devices, but the ChG is fabricated by printing rather than thermal evaporation. As electrode Ni is used instead of Al, a Ni electrode was screen printed on top of the ChG layer. Then the top electrode was screen-printed. The device showed a similar response as the TE device. The threshold voltage is shifted to a higher value and the current level is lower than the TE devices at the SET state. This is expected as the printed thin films did not go through complete melting, so there are much more voids and defects in the printed ChG layer than TE thin films.

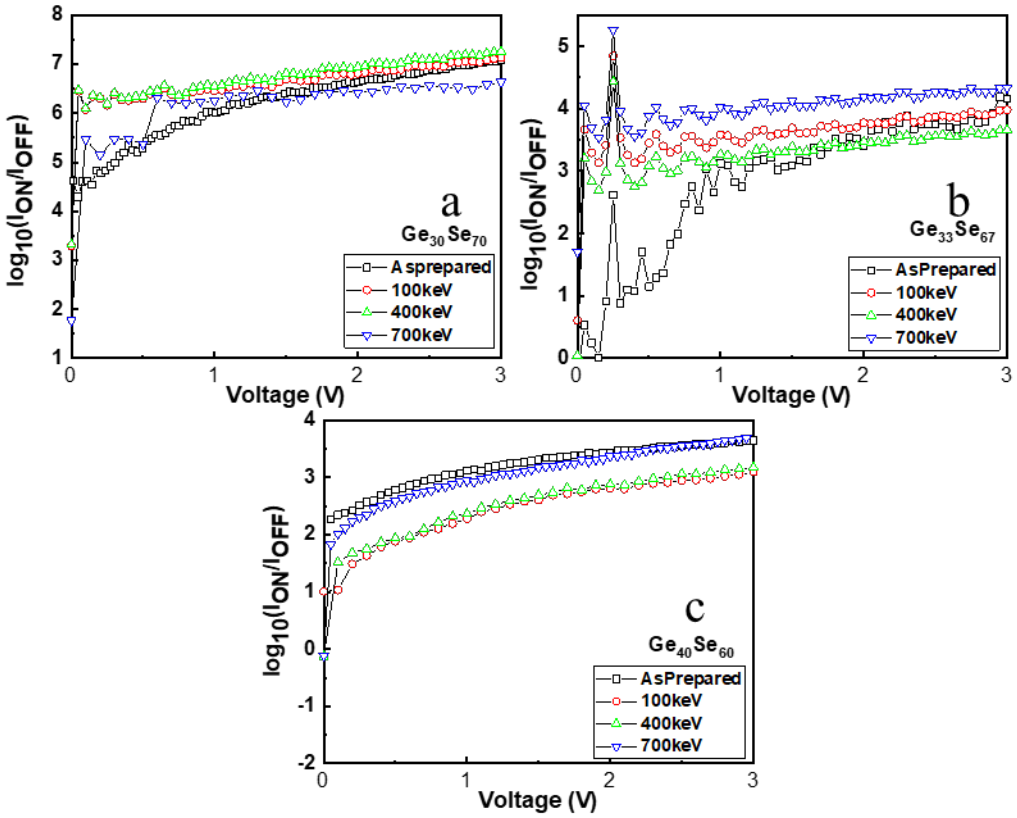

Figure 6.17 Ge_xSe_{100-x} SET Device Characterization after irradiation a) x=30 b) x=33 c) x=40.

Device Fabrication

The device was fabricated by printing 10 layers (thickness 5µm) of $Ge_{30}Se_{70}$ and the Ni electrodes were placed 1mm apart by screen printing. The crystallization onset temperature of $Ge_{30}Se_{70}$ is 441°C [171].

Device Characterization

The devices were heated gradually up to the onset of crystallization temperature. At each temperature, the devices were kept for 15sec. Before reaching the crystallization temperature, the amorphous material is highly resistive, and there is a pA level current flowing through the film. Once the temperature reaches the crystallization onset, a drastic change in I-V characteristic occurs since the material becomes conductive and high current

flows through the film. Building an array of devices with different compositions makes possible real-time monitoring of temperature since the crystallization temperature is composition-dependent. It is also heating rate dependent, which adds one more level of information by the application of these sensors.

The devices were reversed using an electrical pulse, after which the cycle can be repeated, as demonstrated in Figure 6.18. Reversibility was achieved after voltage pulsing by which a Joule heating is produced, that partially melts the film. The final step of the reversing process is a fast cooling of the melted film in contact with the wafer held at room temperature. This solidifies the melt in amorphous condition. After 10 minutes of pulsing, the printed device was RESET (10V square wave, 8µs period, and 45ns ON time).

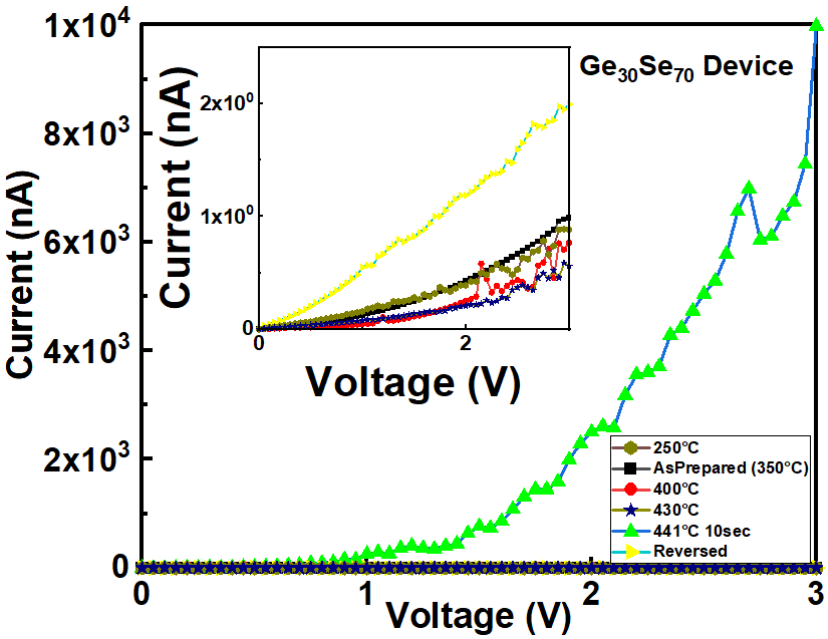

Figure 6.18 Performance of $Ge_{30}Se_{70}$ printed sensor heated at different temperatures.

Mutli-Temperature Sensing

To demonstrate more than one temperature sensing using one device, we synthesized $Sn_2Ge_8S_{15}$, a chalcogenide glass with two crystallization temperatures (peaks at 440°C and 478 °C). The device was heated up to its peak crystallization temperatures 440°C, 478 °C and Low resistive states were achieved. In the crystalline phase, TE devices exhibit nearly ohmic conduction mechanism. This device can measure two different crystallization temperatures. The voltage range for this device is 6-10V which is higher than the other devices. In the printed device, the difference between the two crystalline states is not prominent. On the other hand, TE devices show approximately, 1nA difference at 10V.

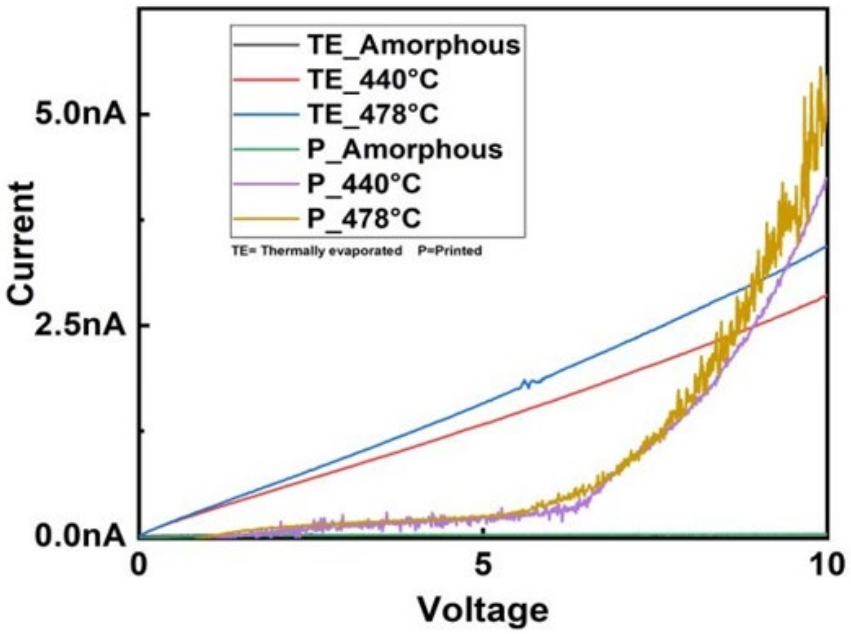

Figure 6.19 Performance of $Sn_2Ge_8S_{15}$ printed chalcogenide glass vertical sensor heated at different temperatures.

Optical and Plasmonic Devices

Ge-Se glasses change their optical properties because of phase change. Traditional CD/DVDs operate utilizing this mechanism. In CD/DVDs, crystallization/amorphization is done by localized heating using different laser pulses. With various waveguides and ChGs, such changes in properties can be used to measure temperature. In the sensor mode, the device will be crystallized by heating/ambient temperature. Next are presented the device structure, operation and performance of such devices based on both Ge-Se and Ge-S glasses.

Chalcogenide Coated Rad Hard Fiber Tip based Temperature Sensor

The optical fiber architecture shown in Figure 6.20 could sense a certain temperature. On the tip of a fiber core, a ChG layer is fabricated by thermal evaporation or dip-coating. The outer gold layer works as a protective sheath to ensure operation in high temperature and radiation environments.

The sensor will consist of an array of these fibers with different ChG layers on the tips, which have different crystallization temperatures, showing the time development of the temperature increase. Alternatively, we worked to find materials with several crystallization temperatures to monitor these characteristic temperatures with an array of devices. Since the fiber diameter is 125 μm, the total diameter of such an array with 10 different fibers will be about 2 mm.

Operation

When Temperature (T) < Crystallization Temperature (T_c): Refractive index and extinction coefficient will be low since the material is in an amorphous state and light will propagate through the fiber with very low losses and some part of it will reflect.

When T > T_c: Refractive index and extinction coefficient will change, since the material is in the crystalline state so the light will propagate through the fiber with higher losses and the reflected power will change.

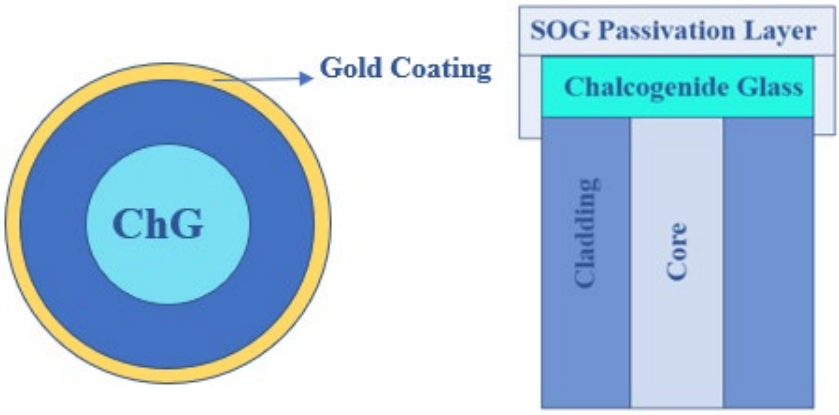

Figure 6.20 Top view of the chalcogenide coated rad-hard fiber-tip based temperature sensor (Left). A more simplified schematic of the device cross-section (Right).

ChG layer was deposited on fiber-tip (fiber dimension- Total diameter 125µm and core 8µm) by thermal evaporation (ChG thickness around 250 nm) or dip-coating with nano-particle ink. For simulation, thin film refractive index *n* and extinction coefficient *k* was used in Fimmwave or COMSOL Spectraphysics to simulate percent reflected power from the ChG-optical fiber interface. Dip-coated and evaporated fiber results are compared.

The proposed optical fiber-based temperature sensor architecture is shown in Figure 6.20. The design is modeled using PhotonDesign software modules (FIMMWAVE and FIMMPROP) and COMSOL. The optical properties of single-mode silica optical fiber with a core refractive index of 1.45 and cladding refractive index of 1.44 at 1550 nm wavelength are used to represent the fiber. The measured complex refractive indices of in-house synthesized Ge-Se and Ge-S compositions in amorphous and crystalline phases are

imported into the simulation models. Table. 6.1 summarizes the T_g, T_o and T_c for all synthesized and studied compositions. As mentioned in the previous chapters, we focused our studies on the representatives of the Se(S) rich members of the Ge-Se(S) systems $Ge_{30}Se(S)_{70,}$ the stoichiometric compositions $Ge_{33}Se(S)_{67}$ and Ge-rich members $Ge_{40}Se(S)_{60.}$

Fiber Sensor Modeling

In the amorphous phase, ChG behaves like a dielectric material with a lower absorption coefficient than in the crystalline phase. From Table C.1, it is evident that compared to the amorphous phase, the complex refractive index of the crystalline phase is vastly different. Thus, the intensity of the reflected light back into the fiber from the ChG-fiber tip interface is also expected to be different. This forms the basis of our sensor's operating mechanism. For example, the simulated result in Figure 6.21 shows the reflected power in $Ge_{40}Se_{60}$ capped fiber device over various temperatures. Due to a low absorption coefficient and a modest difference in the refractive index between ChG and fiber mode, most of the light transmits through the ChG. When the temperature is higher than the crystallization temperature of ChG ($T > T_c$), the material crystallizes. In this phase, the $Ge_{40}Se_{60}$ has a higher refractive index and a higher extinction ratio coefficient (behaves like a metal). Thus, a higher fraction of light is reflected back into the fiber, as shown in Figure 6.21. This change in the reflected power level occurs at very well-defined temperatures ($\sim T=T_c$), monitoring of which provides information regarding the node temperature. Similarly, the effect of all the other ChG composition's refractive index profiles in their amorphous and crystalline phases on the reflected power level can be explained.

The devices were modeled using optical fiber parameters along with refractive index and extinction coefficient extracted from thin film ellipsometry. Both COMSOL and Fimmwave models show a similar result. The simulation does not account for the fiber bending effect and loss in the circulator. This could be why small deviations in the amorphous phase compared to experimental data. Evaporation and crystallization physics were not considered in this model.

Next, the parametric effect of ChG material cap thickness on the reflected powers in the device was studied. Figure 6.22 (a) shows the normalized reflected power back into the fiber for Ge-S (left)- and Ge-Se (right)-capped fiber devices, respectively, as a function of ChG cap thickness. The reflected power into the fiber displays different power levels in the crystalline phase and amorphous phases due to the different extinction coefficients of the material, as shown in Figure 6.22 (b). For most of the studied compositions, selecting an end cap thickness less than 10 μm provides a relatively high extinction ratio that can be easily detected.

From the simulation results, it is observed that all compositions except $Ge_{33}S_{67}$, $Ge_{33}Se_{67}$, and $Ge_{30}S_{70}$ show a considerable difference in extinction coefficient; examples are $Ge_{40}S_{60}$, $Ge_{40}Se_{60}$, and $Ge_{30}Se_{70}$. All compositions (except $Ge_{33}S_{67}$, $Ge_{33}Se_{67}$) crystallize by a heterogeneous process by which several different crystalline phases appear and the structure becomes much denser, which leads to an increase in the refractive index. The stoichiometric compositions, $Ge_{33}S_{67}$ and $Ge_{33}Se_{67,}$ have similar total reflected power in both phases, indicating that small changes occur in the material structure and band gap during the crystallization process homogeneous in its nature [171].

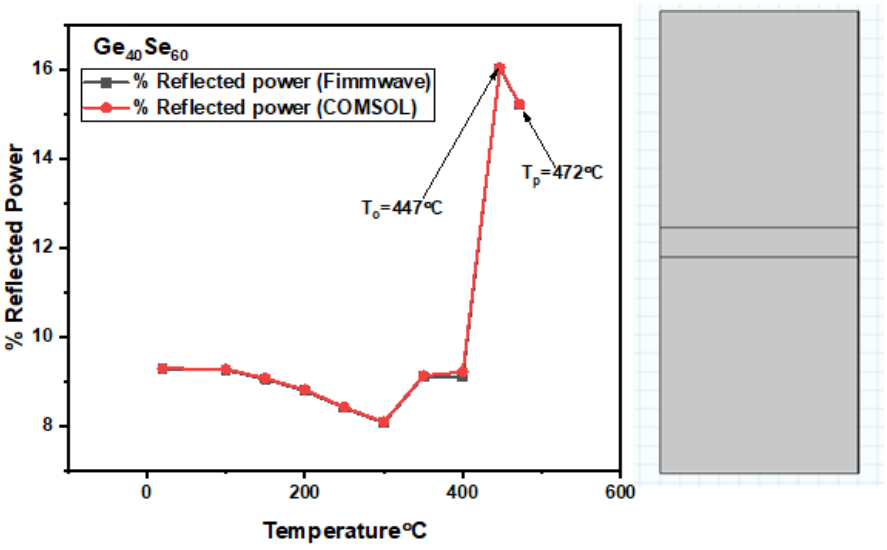

lambda0	1550[nm]	1.55E-6 m	Wavelength
n_core	1.4475	1.4475	Refractive index, core
n_cladding	1.444	1.444	Refractive index, cladding
h_core	8[um]	8E-6 m	Thickness, core
h_cladding	125[um]	1.25E-4 m	Thickness, cladding

Figure 6.21 $Ge_{40}Se_{60}$ fiber-tip based sensor simulation at different temperatures.

Fiber Sensor Fabrication

Gold-coated radiation-hard optical fiber was used for the device fabrication. The fibers were 1m in length. The gold coating was etched at both ends using aqua-regia. After that, both ends were cleaved. At one end of the fiber, ChG was deposited by thermal evaporation. This end is the actual sensor.

The proposed sensor is fabricated using a radiation-hardened pure fused silica core gold-coated fiber (FiberGuide AFS50/125/155G). The length of the employed fiber is about 50 cm. The fabrication process involves two steps. In the first step, to ensure a cleaved fiber tip, about 3–4 cm of gold from the fiber end was stripped by immersing the tip in Aqua Regia solution for 5–10 min [189]. In the second step, the exposed fiber tip was cleaved using a standard fiber cleaver and the cleaved tip was coated with ChG. The

effects of two coating methods to fabricate the sensors were studied: (a) dip coating and (b) thermal evaporation.

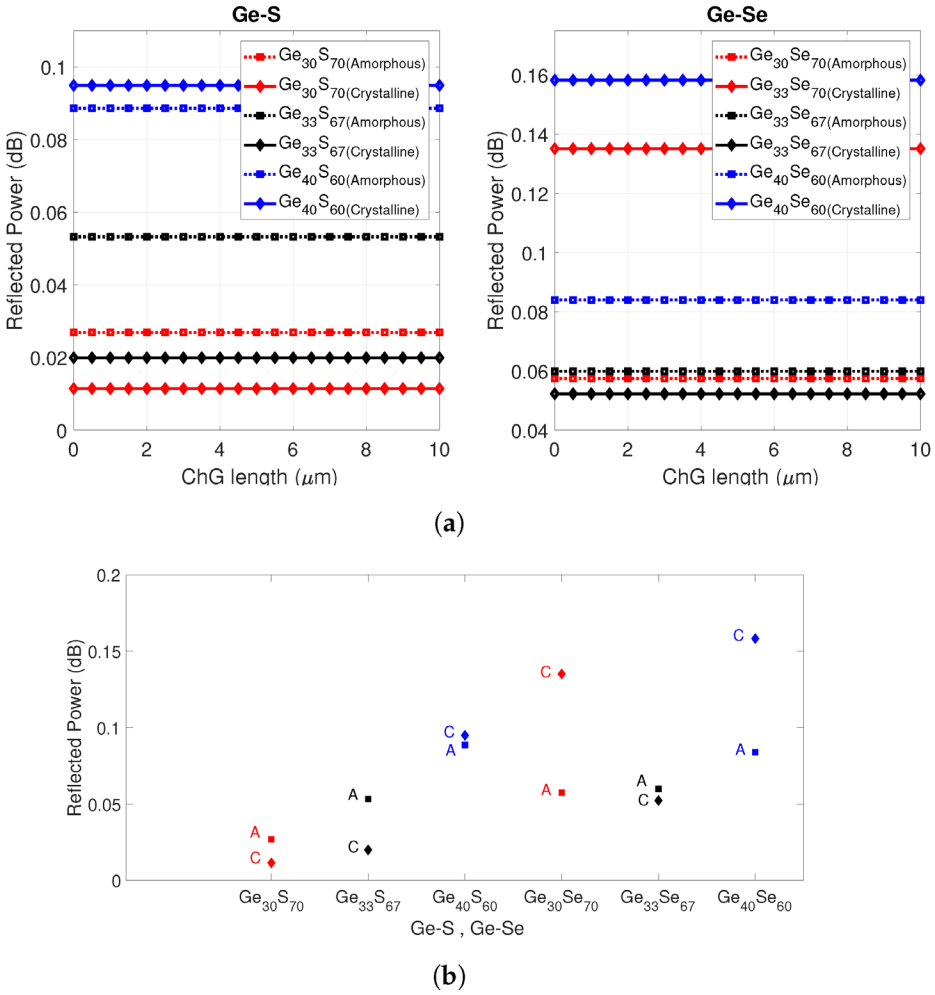

Figure 6.22 (a) Normalized reflected power of the fibers capped with in-house synthesized Ge-S (left) and Ge-Se (right) compositions. The solid curve indicates crystalline phase and the dashed-dotted curve indicates amorphous phase. (b) Normalized reflected power of Ge-Se- and Ge-S-capped fiber tips in amorphous and crystalline phases.

While dip-coating relies on forming a ChG ink, the thermal evaporation method is a standard process and provides a baseline for comparison. The fabrication process is shown in Figure 6.23.

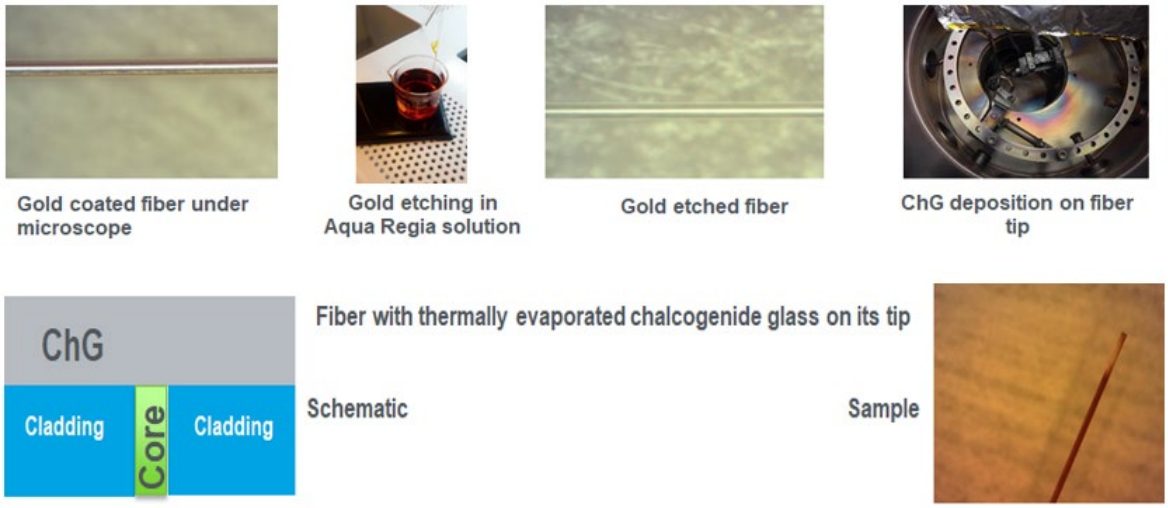

Figure 6.23 Thermally evaporated fiber-based device fabrication.

(a) Thermal evaporation: The ChGs on the tip of the fibers were also coated using thermal evaporation in a Cressington 308R coating system at 10^{-6} mbar vacuum with an evaporation rate of 0.35 Å/s. The fiber was not heated during the film preparation. The thickness of the deposited film was estimated using the output from a quartz crystal microbalance. To check the composition of the deposited coating, ChG was also deposited on a single crystalline silicon substrate along with the fiber. Compared to the composition of the source material, the thin film had ±1.5% compositional deviation as measured by the EDS study. Once the deposition was completed, the fiber tip was dip-coated with spin-on-glass. After drying at room temperature for 24 hours, the coated fibers were heated at 300 °C for 3 hours to cure the spin-on-glass completely. This vapor phase deposition process to form a ChG layer on the fiber tip is a standard process that leads to a highly conformal and uniform thickness coating. The thermally deposited sensors were used to benchmark the performance of the dip-coated devices.

(b) Dip-coating method: The sensor devices were made by dip coating the fiber in ChG nanoparticle ink [173], [190]. The fibers were dipped into the ink under vacuum at

40°C. Then, the fiber tip was heated on a hot plate at 350 °C for 1hour to decompose the surfactants in ink, ethyl cellulose. Once cooled, the fiber tip was dip-coated with spin-on-glass for isolation of the sensor from oxygen-containing ambient. After drying at room temperature for 24 h, the coated fiber was heated at 300 °C for 3 hours to cure the spin-on-glass. A device is shown in Figure 6.24.

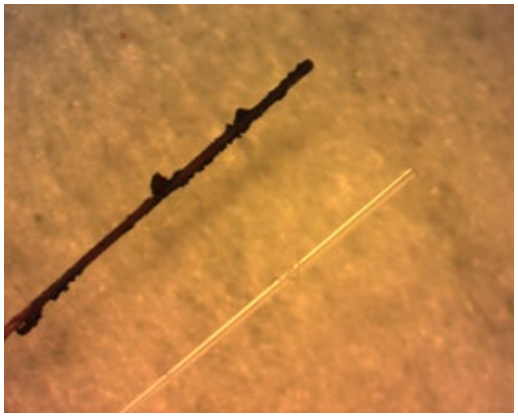

Figure 6.24 Dip coated fiber tip (dark) and blank fiber tip (transparent).

The measurement method is described in chapter 2, in the experimental section.

Results and Discussion

The normalized measured reflected power as a function of time for two compositions - $Ge_{40}Se_{60}$ and $Ge_{30}S_{70}$ are shown in Figure 6.25 and Figure 6.26, respectively. The normalized simulated reflected power with extracted refractive index profile from studying the particular ChGs as a function of time is also plotted. It can be seen from the figures that the measured and the simulated results match very well. Since the proposed sensor works on the principle of the phase change of ChG material, which is highly temperature-dependent, abrupt changes in the reflected power are observed, as predicted by the device simulation.

Two different methods were applied to efficiently extract the sensor data by plotting the slope as a function of time. (1) absolute slope of the reflected power, and (2) normalized reflected power. The first is a powerful tool to see an increase of slope regardless of the optical constants. The second shows data as it is and shows a direct change in optical power, which can be used to measure temperature without further calculation.

For example, from the data regarding the $Ge_{40}Se_{60}$ composition shown in Figure 6.25, a plot of the slope of the measured reflected power as a function of time is shown in Figure 6.27. Two peaks stand out at 2,462 seconds and 2,627 seconds, corresponding to the onset and peak crystallization temperatures of 447°C and 472°C obtained from monitoring the temperature inside the furnace, which is close to the predicted temperatures of 446.6 °C and 472.3°C. The data relating to the onset and peak crystallization temperatures calculated using the slope method for all studied compositions are shown in Table C.3. According to the measured refractive index data presented in Table C.1, two crystallization temperatures for $Ge_{40}S_{60}$ are expected. However, the experimental data only provide one of the crystallization temperatures (485°C), as shown in Table C.3. This is because at the lower crystallization temperature, the material's structure is not strongly organized and thus, no strong optical changes are observable. Table C.3 also provides the expected temperature error in the measured and the expected T_c. It can be seen that except from the evaporated $Ge_{33}Se_{67}$ sample, all other samples are in good agreement within ±10°C.

Based on our preliminary study of these materials and the collected Raman spectroscopy data, we suggest that this is a result of the fact that the stoichiometric

composition has a very homogeneous structure in the amorphous condition with a low number of wrong bonds and this structure is maintained upon crystallization as well [171].

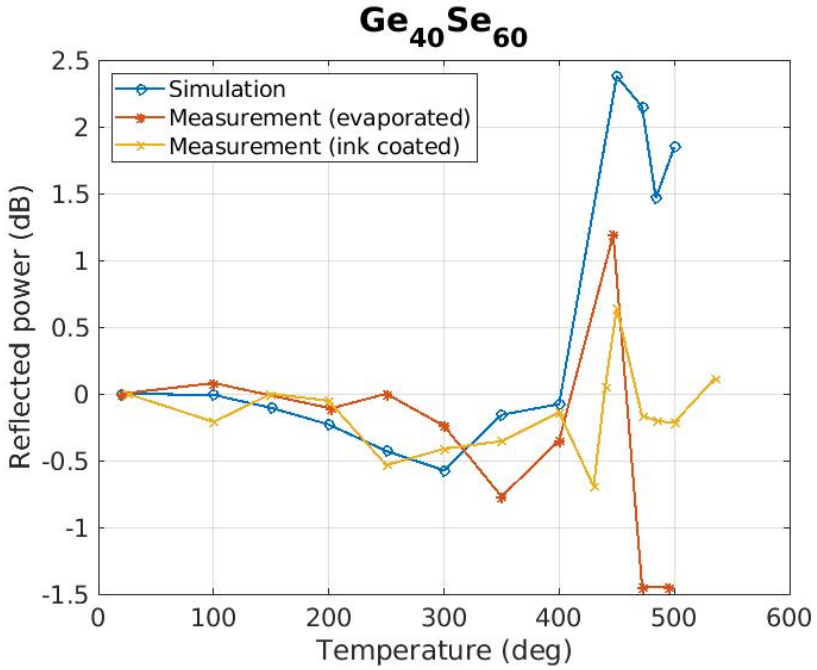

Figure 6.25 Simulated and measured normalized reflected power as a function of time with $Ge_{40}Se_{60}$ capped fiber tip.

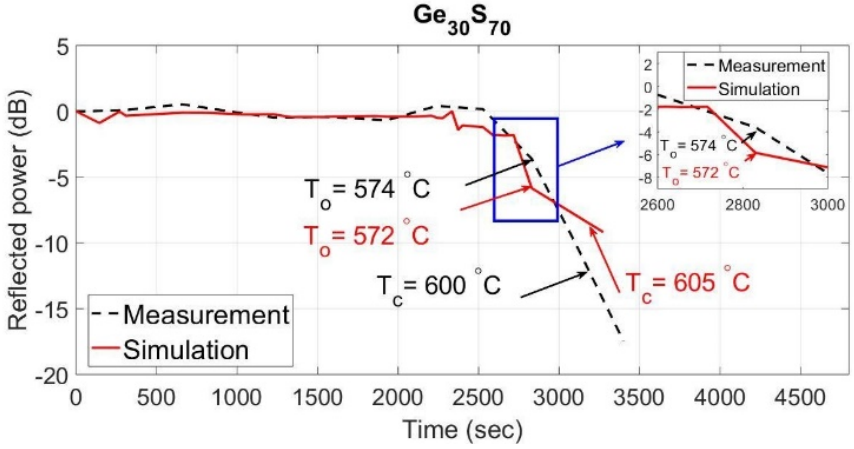

Figure 6.26 Simulated and measured normalized reflected power as a function of time with $Ge_{30}S_{70}$ capped fiber tip (TE).

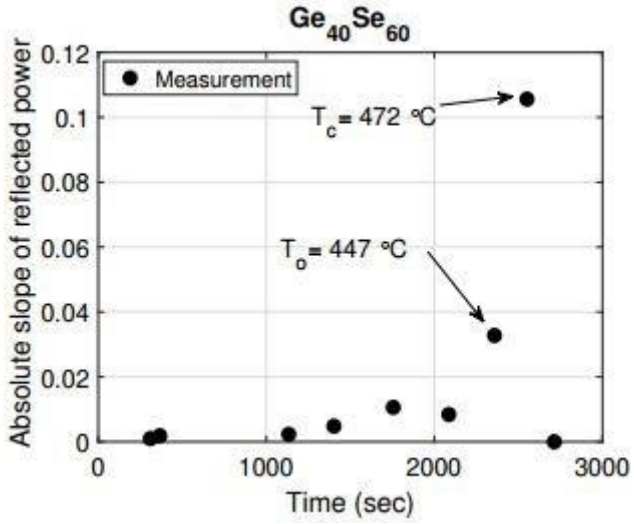

Figure 6.27 Temperature response of evaporated $Ge_{40}Se_{60}$ capped fiber-tip based temperature sensor.

Similarly, the glasses with composition $Ge_{30}Se_{70}$, which have a very close structure to the stoichiometric composition $Ge_{33}Se_{67}$, perform with a small difference of the optical properties after crystallization due to the lack of strong structural reorganization. This is not the case for the $Ge_{30}S_{70}$ compositions, in which the 8-member S rings open up at higher temperatures to become a part of the tetrahedral backbone of the crystalline material, thus leading to an observable change in the refractive index of this material. The crystallization kinetics and the formation of different structural units in these glasses are discussed in detail in [92], [171], [191].

In addition to the change in density, it has been argued [73] that the optical and electrical property contrast due to phase change originates mostly from the transformation in the structural medium-range order after crystallization. The crystalline $GeSe(S)_2$ that appears after the phase change has a predominantly corner-shared structure and is pseudo-two-dimensional when the low-temperature forms of these materials crystallize [192], [193]. In the high-temperature dichalcogenides, the corner-sharing units

are connected with edge-sharing building blocks [105]. Although the kinetics and materials are studied extensively, the change in optical properties due to crystallization is not well understood in these compositions. For example, except for x = 40, Ge-S compositions show a decrease in the refractive index after crystallization. We suggest that this is due to one more detail related to the $Ge_{40}Se(S)_{60}$ studied compositions—in accordance with the XRD studies besides $GeSe(S)_2$, the crystalline form occurring after the phase change contains also GeSe [171], which has *orthorhombic* structure [194]. In this structure, both atoms (Ge and Se or S) are threefold coordinated due to the occurrence of dative bonds. It is for this reason that the Ge-rich compositions react with bigger changes in optical properties after crystallization. In $Ge_{33}Se_{67}$, the change in optical properties due to crystallization is not distinct owing to the lack of medium-range structural changes. For $Ge_{30}Se_{70}$, some previous studies [195] reported a reduction in refractive index, which is also the case for the examined thin films until their temperature reaches the crystallization temperature. These data are from ellipsometric studies of thin films on flat substrates, but the fiber devices showed an increase in reflected power after crystallization, which is direct evidence of the fact that the refractive index increases after crystallization of $Ge_{30}Se_{70}$. We assume that there are additional interference effects occurring in the case of fiber, which influence the results measured from the fiber devices.

Temperature Profile Estimation Using Array Sensor

Arranging the single ChG tip-coated fibers in an array structure and monitoring the reflected power from each fiber will help with the real-time detection of several temperatures inside extreme environments, thus allowing mapping out of the temperature

profile. As mentioned before, each of the synthesized ChG compositions has a specific crystallization temperature which allows for accurate monitoring and recording of real-time temperature profiles within the desired environment. For example, the slope of the reflected power data from the array structure comprises four optical fibers capped with four different ChGs ($Ge_{40}Se_{60}$, $Ge_{30}S_{70}$, $Ge_{40}S_{60}$, and $Ge_{33}Se_{67}$) within a temperature range of 472°C to 600°C is shown in Figure 6.28 (a). At lower temperatures below T_o there are structural fluctuations in the solid-state, due to the initial stages of crystalline organization of the material. For a better reading, the measurements presented at temperatures above T_o are demonstrated at higher resolution. The proposed array sensor is arranged from ChG dip-coated devices, which show lower error in temperature response. Correlating the peak slope and times provides a temperature evolution chart as shown in Figure 6.28 (b), while four distinct temperatures, 472°C, 485°C, 528°C, and 600°C are recorded with this array structure. Increasing the array size to accommodate several other compositions of ChGs will enable real-time and precise monitoring of temperature with higher temperature resolution.

Silicon-Chalcogenide Hybrid Integrated Plasmonic Waveguide Based Temperature Sensor

A schematic cross-section of the device shows that a device consists of a silicon waveguide, with a chalcogenide glass layer on top. The waveguides in the array will be coated with different chalcogenide glasses using ink-jet printing to form the top cladding. The waveguides are fabricated in a silicon-on-insulator (SOI) wafer using a complementary metal-oxide-semiconductor (CMOS) process to keep the cost low. Waveguide fabrication

and device testing was done as part of a separate dissertation so only the results are described here as proof-of-concept.

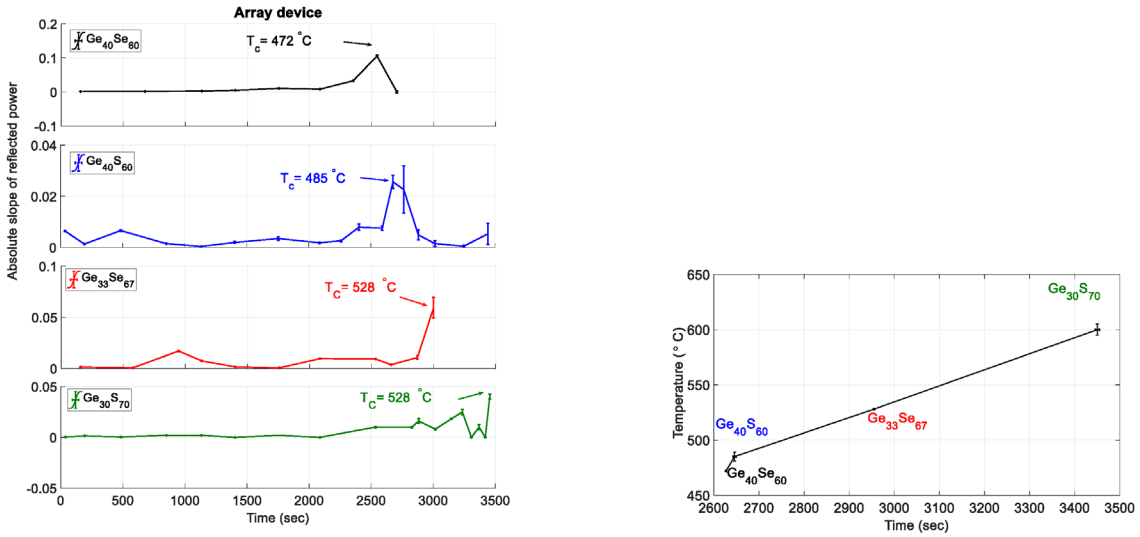

(a) (b)

Figure 6.28 a) Temperature response of array temperature sensor, b) Monitored temperature trend as a function of time using array structure.

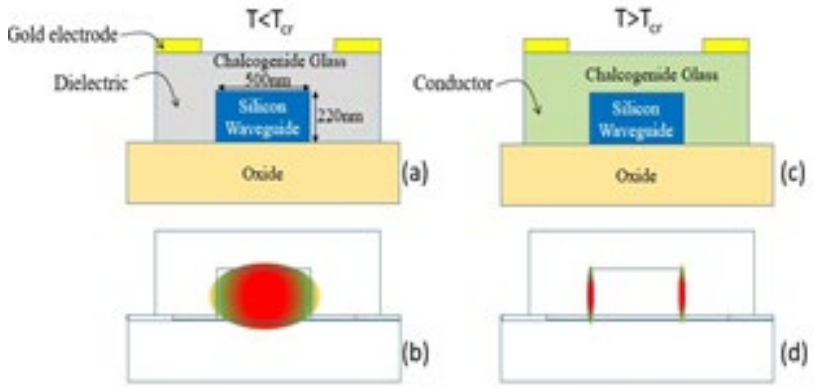

Figure 6.29 (a) Schematic cross-section of the silicon-chalcogenide hybrid integrated plasmonic waveguide-based temperature sensor. ChG forms the top cladding for the silicon waveguide. At $T < T_c$, chalcogenide is a transparent, dielectric and has low optical loss (b) fundamental mode profile for low loss when $T < T_c$. (c) when $T > T_c$, ChG becomes crystalline conductor like and the extinction is higher. (d) at the interface between silicon and ChG, the distribution of the mode of the very glossy surface plasmon mode excited.

Device Fabrication and Characterization

Fabrication of the waveguides is beyond the scope of this work. A shadow mask of Kapton was used to deposit ChG on Si waveguides. In each set, there are three waveguides. The idea is to cover each of them with different ChGs and use them as an array to measure several temperatures. The mask was aligned manually.

The light was coupled with the WG using optical fibers. From Table C.1, it is clearly seen that, although the refractive index could go higher or lower due to crystallization, the extinction coefficient always goes up. Such change confines the wave propagation in the ChG-Si interface and the transmitted power goes down. Figure 6.30 shows, $Ge_{40}S_{60}$ covered WG fabrication and its performance. A sharp reduction of the transmitted power is seen near the peak crystallization temperature of $Ge_{40}S_{60}$.

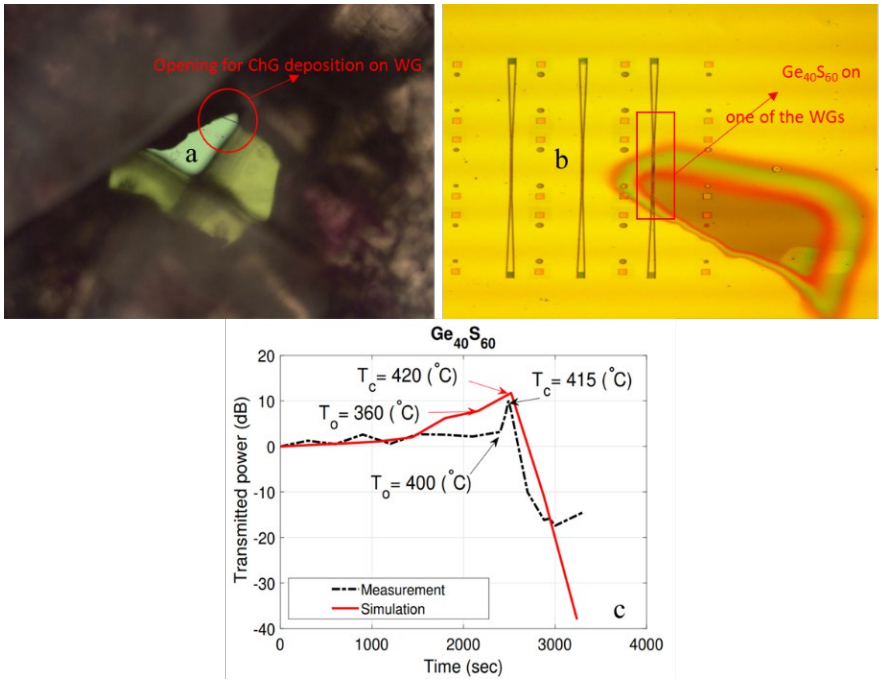

Figure 6.30 a) Kapton shadow mask alignment over WG, b) ChG over WG, c) Performance of a WG covered with $Ge_{40}S_{60}$.

Conclusion

This chapter presented data regarding application of phase change materials for temperature measurement using electrical or waveguide-based devices. SET devices under irradiation demonstrated that the reliability of the device is high even under 10DPA damage. Moreover, TE devices and printed devices both exhibited equally good performance. Using six different compositions of synthesized ChGs, different types of the sensor array can effectively track temperature from 440-600°C. As an example, optical fiber array performance was presented. Electrical devices demonstrated reversibility, which is a promising aspect for a multiple use of the devices.

CHAPTER SEVEN: CONCLUSION

This dissertation focuses on developing nanoparticle ink and printing of ChGs to fabricate phase change temperature sensors (440°C-600°C) for high-radiation environments. Due to the unique properties of Ge-Se and Ge-S ChGs, such a family of glasses was chosen to demonstrate their applicability as optical, electrical and plasmonic sensors. To analyze the performance of printed layers and devices, thermally evaporated thin films and devices were also prepared and their performance was compared. Since the devices must perform in high radiation environments, thin films and devices were tested under irradiation and the data were analyzed. The outcome of this work is summarized below

1. New structural data with more precise evaluation and interpretation of the bond lengths in the studied materials using high energy XRD have been reported.
2. New data regarding the crystallization temperatures have been created for materials from the Ge-S and Ge-Se chalcogenide glass systems.
3. The crystallization process is well documented using Raman spectroscopy, XRD, and microscopic analysis and interpreted based on Kissinger, Ozawa and Augis-Bennett methods. Evaluation of the glass-forming ability in the studied systems has been performed, based on the analysis of the measured characteristics of the studied materials.

4. The crystallization kinetics study revealed that the stoichiometric composition of Ge-Se and Ge-S require more energy to crystallize since their crystallization process is homogeneous in nature. Regardless of the composition, the glasses can be used to fabricate electrical sensors, but their performance as optical sensors depend on the composition due to the structural dependence of the ChGs optical properties. Amorphous ChGs are stable at high irradiation but are affected by low doses of ion irradiation because of the low number of electron-hole pairs generation and thus limited defects proximity and recombination, while crystalline structures can change considerably under irradiation over 10 DPA.
5. The studies of the IV characteristic of the temperature sensing devices proved that they are stable independently of the irradiation intensity due to the pinning of the Fermi level, which contributes to a stable electronic performance.
6. For the first time, nanoparticle inks based on chalcogenide glasses from the Ge-S and Ge-Se systems have been formulated; the process of the nanoparticles and inks formation are optimized and the inks are characterized with their viscosity and contact angle; compositional dependence of these characteristics has been extracted based on materials analysis.
7. For the first time, inkjet printing of ChGs has been performed and the sintering process is optimized. The composition and structure of the printed thin films closely resemble the corresponding thermally evaporated films.

8. Three types of devices have been created–based on the electronic effect, fiber-based devices and performance depending upon plasmons' formation.
9. Printed, dip-coated and thermally evaporated device performance is comparable and an array of devices were set up for real-time temperature monitoring.
10. The electrical devices were RESET by electrical pulsing and it has been proved by SAED pattern.

REFERENCES

[1] IAEA, *Nuclear Power Reactors in the World: 2015 Edition.* Vienna: IAEA, 2015. Accessed: Apr. 02, 2020. [Online]. Available: http://public.eblib.com/choice/publicfullrecord.aspx?p=4853270

[2] Internationale Atomenergie-Organisation, Ed., *Modern instrumentation and control for nuclear power plants: a guidebook*. Vienna: International Atomic Energy Agency, 1999.

[3] H. M. Hashemian, "Nuclear Power Plant Instrumentation and Control," in *Nuclear Power - Control, Reliability and Human Factors*, P. Tsvetkov, Ed. InTech, 2011. doi: 10.5772/18768.

[4] T. Qian, W. H. Hinds, and P. Tonner, "SELF-HEATING, GAMMA HEATING AND HEAT LOSS EFFECTS ON RESISTANCE TEMPERATURE DETECTOR (RTD) ACCURACY," in *Proceedings of the fourth international conference on CANDU maintenance*, Canada, 1997, p. 404.

[5] *National Semiconductor's Temperature Sensor Handbook*. USA: National Semiconductor Corporation, 1995. [Online]. Available: https://shrubbery.net/~heas/willem/PDF/NSC/temphb.pdf

[6] D. H. M. Hashemian, D. D. Beverly, D. W. Mitchell, and K. M. Petersen, *Aging of Nuclear Plant Resistance Temperature Detectors*. CreateSpace Independent Publishing Platform, 2014.

[7] V. F. Sears, "Neutron scattering lengths and cross sections," *Neutron News*, vol. 3, no. 3, pp. 26–37, Jan. 1992, doi: 10.1080/10448639208218770.

[8] P. Pavlasek, S. Duris, and R. Palencar, "Base metal thermocouples drift rate dependence from thermoelement diameter," *J. Phys.: Conf. Ser.*, vol. 588, p. 012016, Feb. 2015, doi: 10.1088/1742-6596/588/1/012016.

[9] S. Kasap, “THERMOELECTRIC EFFECTS IN METALS: THERMOCOUPLES,” p. 11, 1997.

[10] J. Daw, J. Rempe, D. Knudson, J. Crepeau, and S. C. Wilkins, “High Temperature Irradiation-Resistant Thermocouple Performance Improvements,” p. 16.

[11] G. M. Ludtka, T. G. Kollie, R. L. Anderson, and W. H. Christie, “Performance of Chromel versus Alumel and Nicrosil versus Nisil thermocouple assemblies in vacuum and argon between 1000 deg C and 1200 deg C,” *NASA STI/Recon Technical Report N*, vol. 85, Oct. 1984, Accessed: Apr. 02, 2020. [Online]. Available: http://adsabs.harvard.edu/abs/1984STIN...8521624L

[12] K. L. Davis, D. L. Knudson, J. E. Daw, J. L. Rempe, and A. J. Palmer, “Melt Wire Sensors Available to Determine Peak Temperatures in ATR Irradiation Testing,” p. 10.

[13] B. T. Reinhardt, A. Suprock, and B. Tittmann, “Testing piezoelectric sensors in a nuclear reactor environment,” Atlanta, Georgia, USA, 2017, p. 050005. doi: 10.1063/1.4974599.

[14] Jakrisrschner, *Surface Acoustic Wave Sensor Interdigitated Transducer Diagram*. [Online]. Available: https://en.wikipedia.org/wiki/Surface_acoustic_wave_sensor#/media/File:Surface_Acoustic_Wave_Sensor_Interdigitated_Transducer_Diagram.png

[15] R. M. White, “New Prospects for Acoustic Sensors: an Overview,” in *41st Annual Symposium on Frequency Control*, May 1987, pp. 333–338. doi: 10.1109/FREQ.1987.201042.

[16] D. A. Parks, B. Reinhardt, and B. R. Tittmann, “Piezoelectric material for use in a nuclear reactor core,” *AIP Conference Proceedings*, vol. 1430, no. 1, pp. 1633–1639, May 2012, doi: 10.1063/1.4716409.

[17] W. Qiu-kuan, L. Chang-hua, and Y. Yan, “Advanced Measuring (Instrumentation) Methods for Nuclear Installations: A Review,” *Science and Technology of Nuclear Installations*, 2012. https://www.hindawi.com/journals/stni/2012/672876/ (accessed Apr. 02, 2020).

[18] R. M. Waxler and G. W. Cleek, “The Effect of Temperature and Pressure on the Refractive Index of Some Oxide Glasses,” *J Res Natl Bur Stand A Phys Chem*, vol. 77A, no. 6, pp. 755–763, Dec. 1973, doi: 10.6028/jres.077A.046.

[19] A. Morana *et al.*, “Influence of neutron and gamma-ray irradiations on rad-hard optical fiber,” *Opt. Mater. Express, OME*, vol. 5, no. 4, pp. 898–911, Apr. 2015, doi: 10.1364/OME.5.000898.

[20] G. Cheymol, H. Long, J. F. Villard, and B. Brichard, “High level gamma and neutron irradiation of silica optical fibers in CEA OSIRIS nuclear reactor,” in *2007 9th European Conference on Radiation and Its Effects on Components and Systems*, Sep. 2007, pp. 1–5. doi: 10.1109/RADECS.2007.5205466.

[21] A. Sang, M. Froggatt, D. Gifford, S. Kreger, and B. Dickerson, “One Centimeter Spatial Resolution Temperature Measurements in a Nuclear Reactor Using Rayleigh Scatter in Optical Fiber,” *Sensors Journal, IEEE*, vol. 8, pp. 1375–1380, Aug. 2008, doi: 10.1109/JSEN.2008.927247.

[22] M. C. Decreton, “High temperature measurement by noise thermometry,” International Atomic Energy Agency (IAEA), IAEA-TC--389/6-6, 1982.

[23] C. L. Britton, M. Roberts, N. D. Bull, D. E. Holcomb, and R. T. Wood, “Johnson Noise Thermometry for Advanced Small Modular Reactors,” *UNT Digital Library*, Sep. 15, 2012. https://digital.library.unt.edu/ark:/67531/metadc827703/m1/1/ (accessed Apr. 06, 2020).

[24] J. B. Johnson, “Thermal Agitation of Electricity in Conductors,” *Phys. Rev.*, vol. 32, no. 1, pp. 97–109, Jul. 1928, doi: 10.1103/PhysRev.32.97.

[25] R. Kisner *et al.*, “Johnson noise thermometry for harsh environments,” in *2004 IEEE Aerospace Conference Proceedings (IEEE Cat. No.04TH8720)*, Mar. 2004, vol. 4, pp. 2586-2596 Vol.4. doi: 10.1109/AERO.2004.1368053.

[26] N. Habib, C. H. Lam, and R. McMahon, “Phase change material based temperature sensor,” US8114686B2, Feb. 14, 2012 Accessed: Apr. 06, 2020. [Online]. Available: https://patents.google.com/patent/US8114686B2/en

[27] R. Fairman and B. Ushkov, *Semiconducting Chalcogenide Glass I*, vol. 78. [Online]. Available: https://www.sciencedirect.com/bookseries/semiconductors-and-semimetals/vol/78/suppl/C

[28] A. Zakery and S. R. Elliott, "Optical properties and applications of chalcogenide glasses: a review," *J. Non-Cryst. Solids*, vol. 330, no. 1, pp. 1–12, Nov. 2003, doi: 10.1016/j.jnoncrysol.2003.08.064.

[29] J. Stuke, "Review of optical and electrical properties of amorphous semiconductors," *J. Non-Cryst. Solids*, vol. 4, pp. 1–26, Apr. 1970, doi: 10.1016/0022-3093(70)90015-3.

[30] J. C. Phillips, "Topology of covalent non-crystalline solids I: Short-range order in chalcogenide alloys," *J. Non-Cryst. Solids*, vol. 34, no. 2, pp. 153–181, Oct. 1979, doi: 10.1016/0022-3093(79)90033-4.

[31] P. Boolchand, G. Lucovsky, J. C. Phillips, and M. F. Thorpe, "Self-organization and the physics of glassy networks," *Philosophical Magazine*, vol. 85, no. 32, pp. 3823–3838, Nov. 2005, doi: 10.1080/14786430500256425.

[32] D. J. Jacobs and M. F. Thorpe, "Generic Rigidity Percolation: The Pebble Game," *Phys. Rev. Lett.*, vol. 75, no. 22, pp. 4051–4054, Nov. 1995, doi: 10.1103/PhysRevLett.75.4051.

[33] M. F. Thorpe, "Continuous deformations in random networks," *J. Non-Cryst. Solids*, vol. 57, no. 3, pp. 355–370, Sep. 1983, doi: 10.1016/0022-3093(83)90424-6.

[34] M. F. Thorpe, D. J. Jacobs, M. V. Chubynsky, and J. C. Phillips, "Self-organization in network glasses," *J. Non-Cryst. Solids*, vol. 266-269 B, pp. 859–866, May 2000, Accessed: Apr. 06, 2020. [Online]. Available: https://asu.pure.elsevier.com/en/publications/self-organization-in-network-glasses

[35] M. F. Thorpe, D. J. Jacobs, N. V. Chubynsky, and A. J. Rader, "Generic Rigidity of Network Glasses," in *Rigidity Theory and Applications*, M. F. Thorpe and P. M. Duxbury, Eds. Boston, MA: Springer US, 2002, pp. 239–277. doi: 10.1007/0-306-47089-6_14.

[36] P. Boolchand, D. G. Georgiev, and B. Goodman, “DISCOVERY OF THE INTERMEDIATE PHASE IN CHALCOGENIDE GLASSES,” *J. OPT. and ADV. MAT.-RAPID COMMUNICATIONS*, vol. 3, no. 3, pp. 703–720.

[37] F. Wang, S. Mamedov, P. Boolchand, B. Goodman, and M. Chandrasekhar, “Pressure Raman effects and internal stress in network glasses,” *Phys. Rev. B*, vol. 71, no. 17, p. 174201, May 2005, doi: 10.1103/PhysRevB.71.174201.

[38] L. Tichý, H. Tichá, and K. Handlír, “Photoinduced changes of optical properties of amorphous chalcogenide films at ambient air pressure,” *J. Non-Cryst. Solids*, vol. 97–98, pp. 1227–1230, Dec. 1987, doi: 10.1016/0022-3093(87)90293-6.

[39] M. T. M. Shatnawi *et al.*, “Search for a structural response to the intermediate phase in ${\mathrm{Ge}}_{x}{\mathrm{Se}}_{1\ensuremath{-}x}$ glasses,” *Phys. Rev. B*, vol. 77, no. 9, p. 094134, Mar. 2008, doi: 10.1103/PhysRevB.77.094134.

[40] C. T. Moynihan, A. J. Easteal, J. Wilder, and J. Tucker, “Dependence of the glass transition temperature on heating and cooling rate,” *J. Phys. Chem.*, vol. 78, no. 26, pp. 2673–2677, Dec. 1974, doi: 10.1021/j100619a008.

[41] F. H. Stillinger and P. G. Debenedetti, “Glass Transition Thermodynamics and Kinetics,” *Annual Review of Condensed Matter Physics*, vol. 4, no. 1, pp. 263–285, 2013, doi: 10.1146/annurev-conmatphys-030212-184329.

[42] null Zhou, null Paesler, and null Sayers, “Structure of germanium-selenium glasses: An x-ray-absorption fine-structure study,” *Phys. Rev., B Condens. Matter*, vol. 43, no. 3, pp. 2315–2321, Jan. 1991, doi: 10.1103/physrevb.43.2315.

[43] “A Method of Geometrical Representation of the Thermodynamic Properties of Substances by Means of Surfaces | work by Gibbs,” *Encyclopedia Britannica*. https://www.britannica.com/topic/A-Method-of-Geometrical-Representation-of-the-Thermodynamic-Properties-of-Substances-by-Means-of-Surfaces (accessed Apr. 06, 2020).

[44] W. Ostwald, “Studien über die Bildung und Umwandlung fester Körper: 1. Abhandlung: Übersättigung und Überkaltung,” *Zeitschrift für Physikalische Chemie*, vol. 22U, no. 1, pp. 289–330, Feb. 1897, doi: 10.1515/zpch-1897-2233.

[45] R. K. Brow, “Kinetic Theory of Glass Formation: Nucleation,” 2005. [Online]. Available: https://web.mst.edu/~brow/PDF_nucleation.pdf

[46] R. E. Smallman and A. H. W. Ngan, *Physical Metallurgy and Advanced Materials - 7th Edition*. Butterworth-Heinemann, 2007. Accessed: Apr. 06, 2020. [Online]. Available: https://www.elsevier.com/books/physical-metallurgy-and-advanced-materials/smallman/978-0-7506-6906-1

[47] MesserWoland, *Three nuclei on a surface, illustrating decreasing contact angles.* 2006. [Online]. Available: https://commons.wikimedia.org/wiki/File:Surface_tension.svg

[48] N. A. Goryunova and B. T. Kolomiets, “New vitreous semiconductors,” *Izv. AN USSR. Ser. Fiz.*, vol. 20, no. 12, pp. 1496–1500, 1956.

[49] O. I. Shpotyuk, “Radiation-induced effects in chalcogenide vitreous semiconductors, Chapter 6,” in *Semiconductors and Semimetals*, vol. 78, R. Fairman and B. Ushkov, Eds. Elsevier, 2004, pp. 215–260. doi: 10.1016/S0080-8784(04)80048-6.

[50] R. A. Street and N. F. Mott, “States in the Gap in Glassy Semiconductors,” *Phys. Rev. Lett.*, vol. 35, no. 19, pp. 1293–1296, Nov. 1975, doi: 10.1103/PhysRevLett.35.1293.

[51] S. R. Ovshinsky, E. J. Evans, D. L. Nelson, and H. Fritzsche, “Radiation Hardness of Ovonic Devices,” *J OVONIC RES*, vol. 15, no. 6, pp. 311–321, Dec. 1968, doi: 10.1109/TNS.1968.4325062.

[52] T. Shimizu, “Defect States in Chalcogenide Glasses,” *Jpn. J. Appl. Phys.*, vol. 17, no. 3, p. 463, Mar. 1978, doi: 10.1143/JJAP.17.463.

[53] K. Tanaka and K. Shimakawa, “Amorphous Chalcogenide Semiconductors and Related Materials, Introduction,” in *Amorphous Chalcogenide Semiconductors*

and Related Materials, K. Tanaka and K. Shimakawa, Eds. New York, NY: Springer, 2011, pp. 1–28. doi: 10.1007/978-1-4419-9510-0_1.

[54] K. Tanaka, "Configurational and Structural Models for Photodarkening in Glassy Chalcogenides," *Jpn. J. Appl. Phys.*, vol. 25, no. 6R, p. 779, Jun. 1986, doi: 10.1143/JJAP.25.779.

[55] O. A. Lafi and M. M. A. Imran, "The effect of gamma irradiation on glass transition temperature and thermal stability of Se96Sn4 chalcogenide glass," *Radiation Physics and Chemistry*, vol. 79, no. 1, pp. 104–108, Jan. 2010, doi: 10.1016/j.radphyschem.2009.08.005.

[56] M. Naitoh *et al.*, "The radiation tolerance of chalcogenide glasses," in *Infrared Technology and Applications XXXVI*, May 2010, vol. 7660, p. 766028. doi: 10.1117/12.850146.

[57] O. Shpotyuk, M. Shpotyuk, and S. Ubizskii, "RADIATION-INDUCED OPTICAL EFFECTS IN CHALCOGENIDE SEMICONDUCTOR GLASSES," 2017. doi: 10.21175/RADJ.2017.02.021.

[58] P. Macko and D. Lukášik, "Electrical and optical properties of neutron irradiated the GeS8 glass," *Solid State Commun.*, vol. 39, no. 2, pp. 239–243, Jul. 1981, doi: 10.1016/0038-1098(81)90664-5.

[59] J. T. Edmond, J. C. Male, and P. F. Chester, "On the suitability of liquid semiconductors for resistance thermometry in nuclear reactors," *J. Phys. E: Sci. Instrum.*, vol. 1, no. 4, pp. 373–378, Apr. 1968, doi: 10.1088/0022-3735/1/4/302.

[60] S. S. Sarsembinov, E. E. Abdulgafarov, M. A. Tumanov, and N. A. Rogachev, "Radiation-induced defects influence on the electrical, photoelectrical and optical properties of chalcogenide glasses," *J. Non-Cryst. Solids*, vol. 35–36, pp. 877–882, Jan. 1980, doi: 10.1016/0022-3093(80)90311-7.

[61] S. Bhosle, K. Gunasekera, P. Chen, P. Boolchand, M. Micoulaut, and C. Massobrio, "Meeting experimental challenges to physics of network glasses: Assessing the role of sample homogeneity," *Solid State Commun.*, vol. 151, no. 24, pp. 1851–1855, Dec. 2011, doi: 10.1016/j.ssc.2011.10.016.

[62] S. Ravindren, K. Gunasekera, Z. Tucker, A. Diebold, P. Boolchand, and M. Micoulaut, “Crucial effect of melt homogenization on the fragility of non-stoichiometric chalcogenides,” *J. Chem. Phys.*, vol. 140, no. 13, p. 134501, Apr. 2014, doi: 10.1063/1.4869107.

[63] S. Kohara, K. Suzuya, Y. Kashihara, N. Matsumoto, N. Umesaki, and I. Sakai, “A horizontal two-axis diffractometer for high-energy X-ray diffraction using synchrotron radiation on bending magnet beamline BL04B2 at SPring-8,” *Nuclear Instruments and Methods in Physics Research Section A: Accelerators, Spectrometers, Detectors and Associated Equipment*, vol. 467–468, pp. 1030–1033, Jul. 2001, doi: 10.1016/S0168-9002(01)00630-1.

[64] M. Isshiki, Y. Ohishi, S. Goto, K. Takeshita, and T. Ishikawa, “High-energy X-ray diffraction beamline: BL04B2 at SPring-8,” *Nuclear Instruments and Methods in Physics Research Section A: Accelerators, Spectrometers, Detectors and Associated Equipment*, vol. 467–468, pp. 663–666, Jul. 2001, doi: 10.1016/S0168-9002(01)00441-7.

[65] S. R. Ovshinsky, “Reversible Electrical Switching Phenomena in Disordered Structures,” *Phys. Rev. Lett.*, vol. 21, no. 20, pp. 1450–1453, Nov. 1968, doi: 10.1103/PhysRevLett.21.1450.

[66] A. P. Kovalskyy *et al.*, “Chalcogenide glass e-beam and photoresists for ultrathin grayscale patterning,” *JM3*, vol. 8, no. 4, p. 043012, Oct. 2009, doi: 10.1117/1.3273966.

[67] M. R. Latif, P. H. Davis, W. B. Knowton, and M. Mitkova, “CBRAM devices based on a nanotube chalcogenide glass structure,” *J Mater Sci: Mater Electron*, vol. 30, no. 3, pp. 2389–2402, Feb. 2019, doi: 10.1007/s10854-018-0512-0.

[68] E. J. Skoug and D. T. Morelli, “Role of Lone-Pair Electrons in Producing Minimum Thermal Conductivity in Nitrogen-Group Chalcogenide Compounds,” *Phys. Rev. Lett.*, vol. 107, no. 23, p. 235901, Nov. 2011, doi: 10.1103/PhysRevLett.107.235901.

[69] V. Oliveira, D. Cremer, and E. Kraka, “The Many Facets of Chalcogen Bonding: Described by Vibrational Spectroscopy,” *J. Phys. Chem. A*, vol. 121, no. 36, pp. 6845–6862, Sep. 2017, doi: 10.1021/acs.jpca.7b06479.

[70] A. K. Varshneya and J. C. Mauro, *Fundamentals of Inorganic Glasses - 3rd Edition*, 3rd ed. New York: Academic Press Inc., 2019. Accessed: Apr. 08, 2020. [Online]. Available: https://www.elsevier.com/books/fundamentals-of-inorganic-glasses/varshneya/978-0-12-816225-5

[71] S. Sen and B. G. Aitken, “Atomic structure and chemical order in Ge-As selenide and sulfoselenide glasses: An x-ray absorption fine structure spectroscopic study,” *Phys. Rev. B*, vol. 66, no. 13, p. 134204, Oct. 2002, doi: 10.1103/PhysRevB.66.134204.

[72] C. Lin *et al.*, “Defect configurations in Ge–S chalcogenide glasses studied by Raman scattering and positron annihilation technique,” *J. Non-Cryst. Solids*, vol. 355, no. 7, pp. 438–440, Mar. 2009, doi: 10.1016/j.jnoncrysol.2009.01.004.

[73] M. Mitkova, Y. Sakaguchi, D. Tenne, S. K. Bhagat, and T. L. Alford, “Structural details of Ge-rich and silver-doped chalcogenide glasses for nanoionic nonvolatile memory,” *Phys. Stat. Sol A*, vol. 207, no. 3, pp. 621–626, 2010, doi: 10.1002/pssa.200982902.

[74] Y. Kawamoto and S. Tsuchihashi, “Glass-Forming Regions and Structure of Glasses in the System Ge-S,” *Journal of the American Ceramic Society*, vol. 52, no. 11, pp. 626–627, 1969, doi: 10.1111/j.1151-2916.1969.tb15856.x.

[75] R. Azoulay, H. Thibierge, and A. Brenac, “Devitrification characteristics of GexSe1−x glasses,” *J. Non-Cryst. Solids*, vol. 18, no. 1, pp. 33–53, Jul. 1975, doi: 10.1016/0022-3093(75)90006-X.

[76] P. Boolchand, X. Feng, and W. J. Bresser, “Rigidity transitions in binary Ge–Se glasses and the intermediate phase,” *J. Non-Cryst. Solids*, vol. 293–295, pp. 348–356, Nov. 2001, doi: 10.1016/S0022-3093(01)00867-5.

[77] M. V. Chubynsky and M. F. Thorpe, “Self-organization and rigidity in network glasses,” *Current Opinion in Solid State and Materials Science*, vol. 5, no. 6, pp. 525–532, Dec. 2001, doi: 10.1016/S1359-0286(02)00018-9.

[78] A. Sartbaeva, S. A. Wells, A. Huerta, and M. F. Thorpe, “Local structural variability and the intermediate phase window in network glasses,” *Phys. Rev. B*, vol. 75, no. 22, p. 224204, Jun. 2007, doi: 10.1103/PhysRevB.75.224204.

[79] G. Lucovsky, F. L. Galeener, R. C. Keezer, R. H. Geils, and H. A. Six, “Structural interpretation of the infrared and Raman spectra of glasses in the alloy system ${\mathrm{Ge}}_{1\ensuremath{-}x}{\mathrm{S}}_{x}$,” *Phys. Rev. B*, vol. 10, no. 12, pp. 5134–5146, Dec. 1974, doi: 10.1103/PhysRevB.10.5134.

[80] S. Sugai, “Stochastic random network model in Ge and Si chalcogenide glasses,” *Phys. Rev. B*, vol. 35, no. 3, pp. 1345–1361, Jan. 1987, doi: 10.1103/PhysRevB.35.1345.

[81] G. Lucovsky, R. J. Nemanich, and F. L. Galeener, “Amorphous and Liquid Semiconductors,” in *7th International Conference on Amorphous and Liquid Semiconductors*, p. 125.

[82] N. Fueki, T. Usuki, S. Tamaki, H. Okazaki, and Y. Waseda, “Structure of Amorphous Ge–S System by X-Ray Diffraction,” *J. Phys. Soc. Jpn.*, vol. 61, no. 8, pp. 2814–2820, Aug. 1992, doi: 10.1143/JPSJ.61.2814.

[83] E. Bychkov, M. Miloshova, D. L. Price, C. J. Benmore, and A. Lorriaux, “Short, intermediate and mesoscopic range order in sulfur-rich binary glasses,” *J. Non-Cryst. Solids*, vol. 352, no. 1, pp. 63–70, Jan. 2006, doi: 10.1016/j.jnoncrysol.2005.11.002.

[84] A. Bytchkov, G. J. Cuello, S. Kohara, C. J. Benmore, D. L. Price, and E. Bychkov, “Unraveling the atomic structure of Ge-rich sulfide glasses,” *Phys. Chem. Chem. Phys.*, vol. 15, no. 22, pp. 8487–8494, May 2013, doi: 10.1039/C3CP50536G.

[85] S. J. Rettig and J. Trotter, “Refinement of the structure of orthorhombic sulfur, α-S8,” *Acta Crystallographica Section C*, vol. 43, no. 12, pp. 2260–2262, 1987, doi: https://doi.org/10.1107/S0108270187088152.

[86] G. Dittmar and H. Schäfer, “Die Kristallstruktur von HT-GeS2,” *Acta Crystallographica Section B: Structural Crystallography and Crystal Chemistry*, vol. 31, no. 8, pp. 2060–2064, 1975.

[87] W. H. Zachariasen, “The Crystal Lattice of Germano Sulphide, GeS,” *Phys. Rev.*, vol. 40, no. 6, pp. 917–922, Jun. 1932, doi: 10.1103/PhysRev.40.917.

[88] H. Wiedemeier and H. G. Von Schnering, “Refinement of the structures of GeS, GeSe, SnS and SnSe,” *Z. Kristallogr*, vol. 148, no. 295, pp. 3–4, 1978.

[89] A. Okazaki, “The Crystal Structure of Germanium Selenide GeSe,” *J. Phys. Soc. Jpn.*, vol. 13, no. 10, pp. 1151–1155, Oct. 1958, doi: 10.1143/JPSJ.13.1151.

[90] H. C. Hsueh, M. C. Warren, H. Vass, G. J. Ackland, S. J. Clark, and J. Crain, “Vibrational properties of the layered semiconductor germanium sulfide under hydrostatic pressure: Theory and experiment,” *Phys. Rev. B*, vol. 53, no. 22, pp. 14806–14817, Jun. 1996, doi: 10.1103/PhysRevB.53.14806.

[91] S. Blaineau, P. Jund, and D. A. Drabold, “Physical properties of a ${\mathrm{GeS}}_{2}$ glass using approximate ab initio molecular dynamics,” *Phys. Rev. B*, vol. 67, no. 9, p. 094204, Mar. 2003, doi: 10.1103/PhysRevB.67.094204.

[92] Y. Sakaguchi, T. Hanashima, K. Ohara, A.-A. A. Simon, and M. Mitkova, “Structural transformation in ${\mathrm{Ge}}_{x}{\mathrm{S}}_{100\ensuremath{-}x}$ $(10\ensuremath{\le}x\ensuremath{\le}40)$ network glasses: Structural varieties in short-range, medium-range, and nanoscopic scale,” *Phys. Rev. Materials*, vol. 3, no. 3, p. 035601, Mar. 2019, doi: 10.1103/PhysRevMaterials.3.035601.

[93] P. Boolchand, J. Grothaus, M. Tenhover, M. A. Hazle, and R. K. Grasselli, “Structure of GeSsub2 glass: Spectroscopic evidence for broken chemical order,”

Phys. Rev. B, vol. 33, no. 8, pp. 5421–5434, Apr. 1986, doi: 10.1103/PhysRevB.33.5421.

[94] J. D. Neufville and H. K. Rockstad, "Amorphous and Liquid Semiconductors," in *Amorphous and Liquid Semiconductors*, vol. 1, London: Taylor and Francis, 1974, p. 419.

[95] "IUPAC - glass-transition temperature (G02641)." https://goldbook.iupac.org/terms/view/G02641 (accessed Apr. 14, 2020).

[96] A. Hrubý, "Evaluation of glass-forming tendency by means of DTA," *Czech J Phys*, vol. 22, no. 11, pp. 1187–1193, Nov. 1972, doi: 10.1007/BF01690134.

[97] X. Feng, W. J. Bresser, and P. Boolchand, "Direct Evidence for Stiffness Threshold in Chalcogenide Glasses," *Phys. Rev. Lett.*, vol. 78, no. 23, pp. 4422–4425, Jun. 1997, doi: 10.1103/PhysRevLett.78.4422.

[98] Y. Wang, K. Tanaka, T. Nakaoka, and K. Murase, "Evidence of nanophase separation in Ge–Se glasses," *J. Non-Cryst. Solids*, vol. 299–302, pp. 963–967, Apr. 2002, doi: 10.1016/S0022-3093(01)01060-2.

[99] E. Sleeckx, L. Tichý, P. Nagels, and R. Callaerts, "Thermally and photo-induced irreversible changes in the optical properties of amorphous GexSe100-x films," *J. Non-Cryst. Solids*, vol. 198–200, pp. 723–727, May 1996, doi: 10.1016/0022-3093(96)00030-0.

[100] K. Jackson, "Electric Fields in Electronic Structure Calculations: Electric Polarizabilities and IR and Raman Spectra from First Principles," *physica status solidi (b)*, vol. 217, no. 1, pp. 293–310, 2000, doi: 10.1002/(SICI)1521-3951(200001)217:1<293::AID-PSSB293>3.0.CO;2-N.

[101] V. V. Poborchii, A. V. Kolobov, J. Caro, V. V. Zhuravlev, and K. Tanaka, "Polarized Raman spectra of selenium species confined in nanochannels of AlPO4-5 single crystals," *Chemical Physics Letters*, vol. 280, no. 1, pp. 17–23, Nov. 1997, doi: 10.1016/S0009-2614(97)01087-7.

[102] V. V. Poborchii, A. V. Kolobov, J. Caro, V. V. Zhuravlev, and K. Tanaka, "Dynamics of Single Selenium Chains Confined in One-Dimensional

Nanochannels of ${\mathrm{AlPO}}_{4}\ensuremath{-}5$: Temperature Dependencies of the First- and Second-Order Raman Spectra," *Phys. Rev. Lett.*, vol. 82, no. 9, pp. 1955–1958, Mar. 1999, doi: 10.1103/PhysRevLett.82.1955.

[103] R. Holomb, V. Mitsa, E. Akalin, S. Akyuz, and M. Sichka, "Ab initio and Raman study of medium range ordering in GeSe2 glass," *J. Non-Cryst. Solids*, vol. 373–374, pp. 51–56, Aug. 2013, doi: 10.1016/j.jnoncrysol.2013.04.032.

[104] R. Holomb, V. Mitsa, S. Akyuz, and E. Akalin, "New ring-like models and ab initio DFT study of the medium-range structures, energy and electronic properties of GeSe2 glass," *PHILOS MAG*, vol. 93, no. 19, pp. 2549–2562, Jul. 2013, doi: 10.1080/14786435.2013.778426.

[105] K. Inoue, O. Matsuda, and K. Murase, "Raman spectra of tetrahedral vibrations in crystalline germanium dichalcogenides, GeS2 and GeSe2, in high and low temperature forms," *Solid State Commun.*, vol. 79, no. 11, pp. 905–910, Sep. 1991, doi: 10.1016/0038-1098(91)90441-W.

[106] Z. V. Popovic, Y. S. Raptis, E. Anastassakis, and Z. Jaksic, "Pressure-induced amorphization of germanium diselenide," *J. Non-Cryst. Solids*, vol. 227–230, pp. 794–798, May 1998, doi: 10.1016/S0022-3093(98)00172-0.

[107] Z. Jiao, Q. Yao, L. M. Balescu, Q. Liu, B. Tang, and H. J. W. Zandvliet, "Structural and electronic properties of the α-GeSe surface," *Surf. Sci.*, vol. 686, pp. 17–21, Aug. 2019, doi: 10.1016/j.susc.2019.03.007.

[108] U. Köster and P. Weiss, "Crystallization and decomposition of amorphous silicon-aluminium films," *J. Non-Cryst. Solids*, vol. 17, no. 3, pp. 359–368, May 1975, doi: 10.1016/0022-3093(75)90126-X.

[109] D. Nesheva, M. Ailavajhala, P. Chen, D. A. Tenne, H. Barnaby, and M. Mitkova, "Studies of gamma radiation induced effects in ge-rich chalcogenide thin films," in *RAD 2012 - 1st International Conference on Radiation and Dosimetry in Various Fields of Research, Proceedings*, Serbia, 2012, vol. 2012-April, pp. 19–22.

[110] N. Mehta, R. S. Tiwari, and A. Kumar, “Glass forming ability and thermal stability of some Se–Sb glassy alloys,” *Mater. Res. Bull.*, vol. 41, no. 9, pp. 1664–1672, Sep. 2006, doi: 10.1016/j.materresbull.2006.02.024.

[111] S. A. Fayek and M. Fadel, “CRYSTALLIZATION KINETICS OF GeSe CHALCOGENIDE GLASS WITH ANTIMONY,” *J. Ovonic Research*, vol. 5, p. 43, 2009.

[112] Y. Wang, P. Boolchand, and M. Micoulaut, “Glass structure, rigidity transitions and the intermediate phase in the Ge–As–Se ternary,” *EPL*, vol. 52, no. 6, p. 633, Dec. 2000, doi: 10.1209/epl/i2000-00485-9.

[113] M. M. A. Imran, N. S. Saxena, Y. K. Vijay, R. Vijayvergiya, N. B. Maharjan, and M. Husain, “Crystallization kinetics and optical band gap studies of Se96In4 glass before and after slow neutron irradiation,” *J. Non-Cryst. Solids*, vol. 298, no. 1, pp. 53–59, Feb. 2002, doi: 10.1016/S0022-3093(01)01033-X.

[114] P. K. Jain, K. S. Rathore, N. Jain, N. S. Saxena, and Deepika, “ACTIVATION ENERGY OF CRYSTALLIZATION AND ENTHALPY RELEASED OF Se90In10-xSbx (x=0, 2, 4, 6, 8, 10) CHALCOGENIDE GLASSES,” *CHALCOGENIDE LETT*, vol. 6, no. 3, pp. 97–107, 2009.

[115] P. Boolchand, “The Maximum in Glass Transition Temperature (Tg) near x = 1/3 in GexSe1-x Glasses,” *Asian J Phys*, vol. 9, no. 3, pp. 709–721, 2000, Accessed: Apr. 07, 2020. [Online]. Available: http://asianjournalofphysics.in/content2/vol-9-2000/vol-9-no-3

[116] J. Málek, “The glass transition and crystallization of germanium-sulphur glasses,” *J. Non-Cryst. Solids*, vol. 107, no. 2, pp. 323–327, Jan. 1989, doi: 10.1016/0022-3093(89)90479-1.

[117] V. M. Fokin, A. S. Abyzov, E. D. Zanotto, D. R. Cassar, A. M. Rodrigues, and J. W. P. Schmelzer, “Crystal nucleation in glass-forming liquids: Variation of the size of the ‘structural units’ with temperature,” *J. Non-Cryst. Solids*, vol. 447, pp. 35–44, Sep. 2016, doi: 10.1016/j.jnoncrysol.2016.05.017.

[118] H. E. Kissinger, “Variation of peak temperature with heating rate in differential thermal analysis,” *J. RES. NATL. BUR. STAN.*, vol. 57, no. 4, p. 217, Oct. 1956, doi: 10.6028/jres.057.026.

[119] T. Ozawa, “Kinetic analysis of derivative curves in thermal analysis,” *J. Therm. Anal. Calorim.*, vol. 2, no. 3, pp. 301–324, Sep. 1970, doi: 10.1007/BF01911411.

[120] J. A. Augis and J. E. Bennett, “Calculation of the Avrami parameters for heterogeneous solid state reactions using a modification of the Kissinger method,” *J. Therm. Anal. Calorim.*, vol. 13, no. 2, pp. 283–292, Apr. 1978, doi: 10.1007/BF01912301.

[121] J. E. Shelby, *Introduction to Glass Science and Technology*. The Royal Society of Chemistry, 2005. doi: 10.1039/9781847551160.

[122] Y. Sakaguchi, D. A. Tenne, and M. Mitkova, “Structural development in Ge-rich Ge–S glasses,” *J. Non-Cryst. Solids*, vol. 355, no. 37, pp. 1792–1796, Oct. 2009, doi: 10.1016/j.jnoncrysol.2009.04.064.

[123] K. Matusita, T. Komatsu, and R. Yokota, “Kinetics of non-isothermal crystallization process and activation energy for crystal growth in amorphous materials,” *J Mater Sci*, vol. 19, no. 1, pp. 291–296, Jan. 1984, doi: 10.1007/BF02403137.

[124] J. S. Blázquez, C. F. Conde, and A. Conde, “Non-isothermal approach to isokinetic crystallization processes: Application to the nanocrystallization of HITPERM alloys,” *Acta Mater.*, vol. 53, no. 8, pp. 2305–2311, May 2005, doi: 10.1016/j.actamat.2005.01.037.

[125] M. Avrami, “Kinetics of Phase Change. I General Theory,” *J. Chem. Phys.*, vol. 7, no. 12, pp. 1103–1112, Dec. 1939, doi: 10.1063/1.1750380.

[126] M. Avrami, “Kinetics of Phase Change. II Transformation-Time Relations for Random Distribution of Nuclei,” *J. Chem. Phys.*, vol. 8, no. 2, pp. 212–224, Feb. 1940, doi: 10.1063/1.1750631.

[127] M. Avrami, “Granulation, Phase Change, and Microstructure Kinetics of Phase Change. III,” *J. Chem. Phys.*, vol. 9, no. 2, pp. 177–184, Feb. 1941, doi: 10.1063/1.1750872.

[128] P. Gong, S. Zhao, H. Ding, K. Yao, and X. Wang, “Nonisothermal crystallization kinetics, fragility and thermodynamics of Ti20Zr20Cu20Ni20Be20 high entropy bulk metallic glass,” *J. Mater. Res.*, vol. 30, no. 18, pp. 2772–2782, Sep. 2015, doi: 10.1557/jmr.2015.253.

[129] A. Mishchenko, J. Berashevich, K. Wolf, D. A. Tenne, A. Reznik, and M. Mitkova, “Dynamic variations of the light-induced effects in a-Ge_xSe_{100-x} films: experiment and simulation,” *Opt. Mater. Express, OME*, vol. 5, no. 2, pp. 295–306, Feb. 2015, doi: 10.1364/OME.5.000295.

[130] M. Mitkova *et al.*, “X-ray radiation induced effects in selected chalcogenide glasses and CBRAM devices based on them,” *Phys Status Solidi (B) Basic Res*, vol. 253, no. 6, pp. 1060–1068, Jun. 2016, doi: 10.1002/pssb.201552562.

[131] M. S. Ailavajhala *et al.*, “Gamma radiation induced effects in floppy and rigid Ge-containing chalcogenide thin films,” *Journal of Applied Physics*, vol. 115, no. 4, p. 043502, Jan. 2014, doi: 10.1063/1.4862561.

[132] J. L. Taggart *et al.*, “Ionizing Radiation Effects on Nonvolatile Memory Properties of Programmable Metallization Cells,” *IEEE Transactions on Nuclear Science*, vol. 61, no. 6, pp. 2985–2990, Dec. 2014, doi: 10.1109/TNS.2014.2362126.

[133] T. Nichol *et al.*, “Structural and Material Changes in Thin Film Chalcogenide Glasses Under Ar-Ion Irradiation,” *IEEE Transactions on Nuclear Science*, vol. 61, no. 6, pp. 2855–2861, Dec. 2014, doi: 10.1109/TNS.2014.2367578.

[134] G. S. Was *et al.*, “Emulation of reactor irradiation damage using ion beams,” *Scripta Materialia*, vol. 88, pp. 33–36, Oct. 2014, doi: 10.1016/j.scriptamat.2014.06.003.

[135] K. Murase, “Vibrational Excitations in Glasses — C. RAMAN SCATTERING,” in *Insulating and Semiconductor Glasses*, vol. 17, P. Boolchand, Ed. WORLD SCIENTIFIC, 2000, pp. 415–463. doi: 10.1142/9789812813619_0011.

[136] D. K. Avasthi and G. K. Mehta, “Ion Matter Interaction,” in *Swift Heavy Ions for Materials Engineering and Nanostructuring*, D. K. Avasthi and G. K. Mehta, Eds. Dordrecht: Springer Netherlands, 2011, pp. 47–66. doi: 10.1007/978-94-007-1229-4_2.

[137] G. Yang *et al.*, “Physical properties of the GexSe1−x glasses in the 0,” *Journal of Non-Crystalline Solids*, vol. 377, pp. 54–59, Oct. 2013, doi: 10.1016/j.jnoncrysol.2013.01.049.

[138] Crystalmaker, “Elements, Atomic Radii and the Periodic Radii,” *Crystalmaker.com*. http://crystalmaker.com/support/tutorials/atomic-radii/index.html (accessed Jul. 19, 2020).

[139] M.-L. Theye, A. Gheorghiu, C. Senemaud, M. F. Kotkata, and K. M. Kandil, “Studies of short-range order in amorphous Ge x Se100−x compounds by X-ray photoelectron spectroscopy,” *Philosophical Magazine B*, vol. 69, no. 2, pp. 209–222, Feb. 1994, doi: 10.1080/01418639408240104.

[140] P. K. Dwivedi, S. K. Tripathi, A. Pradhan, V. N. Kulkarni, and S. C. Agarwal, “Raman study of ion irradiated GeSe films,” *Journal of Non-Crystalline Solids*, vol. 266–269, pp. 924–928, May 2000, doi: 10.1016/S0022-3093(99)00867-4.

[141] H. Takeuchi, O. Matsuda, and K. Murase, “Reversible mesoscopic structural transformations in vacuum evaporated amorphous Ge30Se70 film studied by Raman scattering,” *Journal of Non-Crystalline Solids*, vol. 238, no. 1, pp. 91–97, Sep. 1998, doi: 10.1016/S0022-3093(98)00685-1.

[142] J. Rumble, *Handbook of Chemistry and Physics 101st Edition*. CRC Press. Accessed: Jul. 31, 2020. [Online]. Available: http://hbcponline.com/faces/contents/ContentsSearch.xhtml;jsessionid=6CF12DB16C4217798E361DAF721178D8

[143] M. A. Abdel-Rahim, M. M. Hafiz, and A. M. Shamekh, “A study of crystallization kinetics of some Ge–Se–In glasses,” *Physica B: Condensed Matter*, vol. 369, no. 1, pp. 143–154, Dec. 2005, doi: 10.1016/j.physb.2005.08.007.

[144] L. Filipovic, “Silicon Dioxide Properties,” *Topography Simulation of Novel Processing Techniques*. https://www.iue.tuwien.ac.at/phd/filipovic/node26.html (accessed Jul. 28, 2020).

[145] E.-C. Inc, “Properties of Silicon - El-Cat.com,” *Properties of silicon and silicon wafersProperties of silicon and silicon wafers*. https://www.el-cat.com/silicon-properties.htm (accessed Jul. 28, 2020).

[146] Y. Wang, K. Tanaka, T. Nakaoka, and K. Murase, “Effect of nanophase separation on crystallization process in Ge–Se glasses studied by Raman scattering,” *Physica B: Condensed Matter*, vol. 316–317, pp. 568–571, May 2002, doi: 10.1016/S0921-4526(02)00575-6.

[147] A. Sharma, M. Varshney, H.-J. Shin, Y. Kumar, S. Gautam, and K. H. Chae, “Monoclinic to tetragonal phase transition in ZrO2 thin films under swift heavy ion irradiation: Structural and electronic structure study,” *Chemical Physics Letters*, vol. 592, pp. 85–89, Jan. 2014, doi: 10.1016/j.cplett.2013.12.012.

[148] N. C. Mishra, “Swift heavy ion irradiation-induced phase transformation in oxide materials,” *Radiation Effects and Defects in Solids*, vol. 166, no. 8–9, pp. 657–665, Sep. 2011, doi: 10.1080/10420150.2011.578637.

[149] D. Simeone, D. Gosset, J. L. Bechade, and A. Chevarier, “Analysis of the monoclinic–tetragonal phase transition of zirconia under irradiation,” *Journal of Nuclear Materials*, vol. 300, no. 1, pp. 27–38, Jan. 2002, doi: 10.1016/S0022-3115(01)00701-2.

[150] B. Schuster, C. Trautmann, and F. Fujara, “Stabilization of high-pressure phase in HfO2*,” GSI Scientific Reoprt (Project No. FU 308/12) PNI-MR-02, 2011. [Online]. Available: https://www.semanticscholar.org/paper/Stabilization-of-high-

pressure-phase-in-HfO-2-*-Schuster-Trautmann/197a698e51d824e22fc6edae641a925a8cf632fa

[151] T. G. Edwards and S. Sen, “Structure and relaxation in germanium selenide glasses and supercooled liquids: a Raman spectroscopic study,” *J Phys Chem B*, vol. 115, no. 15, pp. 4307–4314, Apr. 2011, doi: 10.1021/jp202174x.

[152] H. W. Tan, T. Tran, and C. K. Chua, “A review of printed passive electronic components through fully additive manufacturing methods,” *Virtual and Physical Prototyping*, vol. 11, no. 4, pp. 271–288, Oct. 2016, doi: 10.1080/17452759.2016.1217586.

[153] S. A. M. Tofail, E. P. Koumoulos, A. Bandyopadhyay, S. Bose, L. O’Donoghue, and C. Charitidis, “Additive manufacturing: scientific and technological challenges, market uptake and opportunities,” *Materials Today*, vol. 21, no. 1, pp. 22–37, Jan. 2018, doi: 10.1016/j.mattod.2017.07.001.

[154] U. M. Dilberoglu, B. Gharehpapagh, U. Yaman, and M. Dolen, “The Role of Additive Manufacturing in the Era of Industry 4.0,” *Procedia Manufacturing*, vol. 11, pp. 545–554, 2017, doi: 10.1016/j.promfg.2017.07.148.

[155] R. Singh, E. Singh, and H. S. Nalwa, “Inkjet printed nanomaterial based flexible radio frequency identification (RFID) tag sensors for the internet of nano things,” *RSC Adv.*, vol. 7, no. 77, pp. 48597–48630, Oct. 2017, doi: 10.1039/C7RA07191D.

[156] F. Kotz *et al.*, “Three-dimensional printing of transparent fused silica glass,” *Nature*, vol. 544, no. 7650, Art. no. 7650, Apr. 2017, doi: 10.1038/nature22061.

[157] J. F. Destino *et al.*, “3D Printed Optical Quality Silica and Silica–Titania Glasses from Sol–Gel Feedstocks,” *Advanced Materials Technologies*, vol. 3, no. 6, p. 1700323, 2018, doi: https://doi.org/10.1002/admt.201700323.

[158] I. Cooperstein, E. Shukrun, O. Press, A. Kamyshny, and S. Magdassi, “Additive Manufacturing of Transparent Silica Glass from Solutions,” *ACS Appl. Mater. Interfaces*, vol. 10, no. 22, pp. 18879–18885, Jun. 2018, doi: 10.1021/acsami.8b03766.

[159] E. Baudet, Y. Ledemi, P. Larochelle, S. Morency, and Y. Messaddeq, "3D-printing of arsenic sulfide chalcogenide glasses," *Opt. Mater. Express, OME*, vol. 9, no. 5, pp. 2307–2317, May 2019, doi: 10.1364/OME.9.002307.

[160] S. Novak *et al.*, "Direct Electrospray Printing of Gradient Refractive Index Chalcogenide Glass Films," *ACS Appl. Mater. Interfaces*, vol. 9, no. 32, pp. 26990–26995, Aug. 2017, doi: 10.1021/acsami.7b06140.

[161] E. A. Sanchez, M. Waldmann, and C. B. Arnold, "Chalcogenide glass microlenses by inkjet printing," *Appl. Opt., AO*, vol. 50, no. 14, pp. 1974–1978, May 2011, doi: 10.1364/AO.50.001974.

[162] S. Slang, K. Palka, L. Loghina, A. Kovalskiy, H. Jain, and M. Vlcek, "Mechanism of the dissolution of As–S chalcogenide glass in n-butylamine and its influence on the structure of spin coated layers," *Journal of Non-Crystalline Solids*, vol. 426, pp. 125–131, Oct. 2015, doi: 10.1016/j.jnoncrysol.2015.07.009.

[163] H. Nguyen, A. Yakubov, P. Lazarenko, A. Volkova, A. Sherchenkov, and S. Kozyukhin, "Characteristics of Amorphous As2S3 Semiconductor Films Obtained via Spin Coating," *Semiconductors*, vol. 52, pp. 1963–1968, Dec. 2018, doi: 10.1134/S1063782618150058.

[164] K. Palka, J. Jancalek, S. Slang, M. Grinco, and M. Vlcek, "Comparison of optical and chemical properties of thermally evaporated and spin-coated chalcogenide AsS thin films targeting electron beam lithography applications," *Journal of Non-Crystalline Solids*, vol. 508, pp. 7–14, Mar. 2019, doi: 10.1016/j.jnoncrysol.2018.12.012.

[165] Y. Zha, M. Waldmann, and C. B. Arnold, "A review on solution processing of chalcogenide glasses for optical components," *Opt. Mater. Express, OME*, vol. 3, no. 9, pp. 1259–1272, Sep. 2013, doi: 10.1364/OME.3.001259.

[166] T. Kohoutek, T. Wagner, M. Frumar, A. Chrissanthopoulos, O. Kostadinova, and S. N. Yannopoulos, "Effect of cluster size of chalcogenide glass nanocolloidal solutions on the surface morphology of spin-coated amorphous films," *Journal of Applied Physics*, vol. 103, no. 6, p. 063511, Mar. 2008, doi: 10.1063/1.2895005.

[167] T. Guiton and C. Pantano, “Sol-to-Gel and Gel-to-Glass Transitions in the As2S3-Amine system,” *MRS Proceedings*, vol. 121, Jan. 2011, doi: 10.1557/PROC-121-509.

[168] T. A. Guiton and C. G. Pantano, “Solution/gelation of arsenic trisulfide in amine solvents,” *Chem. Mater.*, vol. 1, no. 5, pp. 558–563, Sep. 1989, doi: 10.1021/cm00005a018.

[169] Y.-C. Liao, F.-Y. Yang, and C. Ting, “Ink composition, Chalcogenide Semiconductor Film, Photovoltaic Device and Methods for Forming the same,” US20120282730A1, Nov. 08, 2012 Accessed: Apr. 07, 2021. [Online]. Available: https://patents.google.com/patent/US20120282730/en

[170] C. J. Hages *et al.*, “The potential of nanoparticle ink-based processing for Chalcogenide photovoltaics,” in *2014 IEEE 40th Photovoltaic Specialists Conference (PVSC) Volume 2*, Jun. 2014, pp. 1–3. doi: 10.1109/PVSC-Vol2.2014.7588255.

[171] A.-A. Ahmed Simon, B. Badamchi, H. Subbaraman, Y. Sakaguchi, and M. Mitkova, “Phase change in Ge–Se chalcogenide glasses and its implications on optical temperature-sensing devices,” *J Mater Sci: Mater Electron*, vol. 31, no. 14, pp. 11211–11226, Jul. 2020, doi: 10.1007/s10854-020-03669-0.

[172] C. Suryanarayana, “Mechanical alloying and milling,” *Progress in Materials Science*, vol. 46, no. 1, pp. 1–184, Jan. 2001, doi: 10.1016/S0079-6425(99)00010-9.

[173] A.-A. A. Simon, S. M. R. Ullah, B. Badamchi, H. Subbaraman, and M. Mitkova, “Materials Characterization of Thin Films Printed with Ge20Se80 Ink,” *Microscopy and Microanalysis*, vol. 25, no. S2, pp. 2606–2607, Aug. 2019, doi: 10.1017/S143192761901376X.

[174] “Safety Data Sheet: Selenium Dioxide.” Accessed: Apr. 07, 2021. [Online]. Available: http://www.integrachem.com/msds/S138_26294_101.pdf

[175] M. Jin, P. Boolchand, and M. Mitkova, “Heterogeneity of molecular structure of Ag photo-diffused Ge30Se70 thin films,” *Journal of Non-Crystalline Solids*, vol. 354, no. 19, pp. 2719–2723, May 2008, doi: 10.1016/j.jnoncrysol.2007.10.091.

[176] M. Descamps and J. Willart, “Perspectives on the amorphization/milling relationship in pharmaceutical materials,” *Advanced Drug Delivery Reviews*, vol. 100, Jan. 2016, doi: 10.1016/j.addr.2016.01.011.

[177] J.-F. Willart, L. Carpentier, F. Danède, and M. Descamps, “Solid-state vitrification of crystalline griseofulvin by mechanical milling,” *J Pharm Sci*, vol. 101, no. 4, pp. 1570–1577, Apr. 2012, doi: 10.1002/jps.23041.

[178] S. D. Doke, C. M. Patel, and V. N. Lad, “Improving Performance of the Synthesis of Silica Nanoparticles by Surfactant-incorporated Wet Attrition Milling,” *Silicon*, Jan. 2021, doi: 10.1007/s12633-020-00871-x.

[179] D. Guérard, “Ball milling in the presence of a fluid: Results and perspectives,” *Reviews on Advanced Materials Science*, vol. 18, Aug. 2008.

[180] C.-N. Chen, Y.-L. Chen, and W. J. Tseng, “Surfactant-assisted de-agglomeration of graphite nanoparticles by wet ball mixing,” *Journal of Materials Processing Technology*, vol. 190, no. 1, pp. 61–64, Jul. 2007, doi: 10.1016/j.jmatprotec.2007.03.109.

[181] K. Ksiażek, S. Wacke, T. Górecki, and C. Górecki, “Effect of the milling conditions on the degree of amorphization of selenium by milling in a planetary ball mill,” *J. Phys.: Conf. Ser.*, vol. 79, p. 012037, Aug. 2007, doi: 10.1088/1742-6596/79/1/012037.

[182] A. W. Weeber and H. Bakker, “Amorphization by ball milling. A review,” *Physica B: Condensed Matter*, vol. 153, no. 1, pp. 93–135, Oct. 1988, doi: 10.1016/0921-4526(88)90038-5.

[183] P. Boolchand and W. J. Bresser, “The structural origin of broken chemical order in GeSe2 glass,” *Philosophical Magazine B*, vol. 80, no. 10, pp. 1757–1772, Oct. 2000, doi: 10.1080/13642810008216504.

[184] D. Tuschel, “Stress, Strain, and Raman Spectroscopy,” *Spectroscopy Online*, vol. 34, no. 9, pp. 10–21, Sep. 01, 2019. Accessed: Apr. 07, 2021. [Online]. Available: https://www.spectroscopyonline.com/view/stress-strain-and-raman-spectroscopy

[185] S. Slang, P. Janicek, K. Palka, and M. Vlcek, “Structure and properties of spin-coated $Ge_{25}S_{75}$ chalcogenide thin films,” *Opt. Mater. Express, OME*, vol. 6, no. 6, pp. 1973–1985, Jun. 2016, doi: 10.1364/OME.6.001973.

[186] S. Slang, K. Palka, P. Janicek, M. Grinco, and M. Vlcek, “Solution processed $As_{30}Se_{70}$ chalcogenide glass thin films with specular optical quality: multi-component solvent approach,” *Opt. Mater. Express, OME*, vol. 8, no. 4, pp. 948–959, Apr. 2018, doi: 10.1364/OME.8.000948.

[187] Y. Zou *et al.*, “Effect of annealing conditions on the physio-chemical properties of spin-coated As_2Se_3 chalcogenide glass films,” *Opt. Mater. Express, OME*, vol. 2, no. 12, pp. 1723–1732, Dec. 2012, doi: 10.1364/OME.2.001723.

[188] M. Y. Chuang, “Surface Roughness Dependence of Inkjet Printing of Ag Nanoparticles,” *Technical Report*, p. 9.

[189] FiberGuide, “Fiberguide Industries. Buffer Removal Techniques for Optical Fiber. 2008.” Accessed: Sep. 17, 2020. [Online]. Available: https://www.fiberguide.com/supplier-resources/application-notes/

[190] A.-A. Ahmed Simon, K. Kadrager, B. Badamchi, H. Subbaraman, and M. Mitkova, “TEMPERATURE SENSING IN NUCLEAR FACILITIES: APPLICATION OF THE PHASE CHANGE EFFECT OF CHALCOGENIDE GLASSES,” presented at the Nuclear Plant Instrumentation, Control, and Human-Machine Interface Technologies, Orlando,FL, Feb. 2019. doi: 10.6084/m9.figshare.10031921.

[191] J. Málek and J. Klikorka, “Crystallization kinetics of glassy GeS2,” *Journal of Thermal Analysis*, vol. 32, no. 6, pp. 1883–1893, Nov. 1987, doi: 10.1007/BF01913981.

[192] V. G. DITTMAR and H. SCHAFER, “Die Kristallstruktur von Germaniumdiselenid.,” *Acta Cryst.*, vol. B32, pp. 2726–2728, 1976.

[193] S. S. Fouad, “On the glass transition temperature and related parameters in the glassy GexSe1−x system,” *Physica B Condens. Matter*, vol. 293, no. 3, pp. 276–282, Jan. 2001, doi: 10.1016/S0921-4526(00)00563-9.

[194] R. Eymard and A. Otto, “Optical and electron-energy-loss spectroscopy of GeS, GeSe, SnS, and SnSe single crystals,” *Physical Review B*, vol. 16, no. 4, p. 1616, 1977.

[195] G. Saffarini, “The effect of compositional variations on the glass-transition and crystallisation temperatures in Ge-Se-In glasses,” *Appl Phys A*, vol. 74, no. 2, pp. 283–285, Feb. 2002, doi: 10.1007/s003390100894.

APPENDIX A

Optical Properties of Chalcogenide glasses

As mentioned earlier, the data was collected *in situ* and modeling needed to be done to extract *n* and *k*. In this portion, the modeling is discussed with an example of $Ge_{30}Se_{70}$ thin films. To extract *n* and *k*, *Psi* and *Delta* spectra obtained by variable angle spectroscopic ellipsometry (VASE) were modeled with Cauchy equation.

Ellipsometric data was collected while the thin films are being heated in a heat stage. Figure A.1 shows the measurement setup. The data was collected at 70° angle.

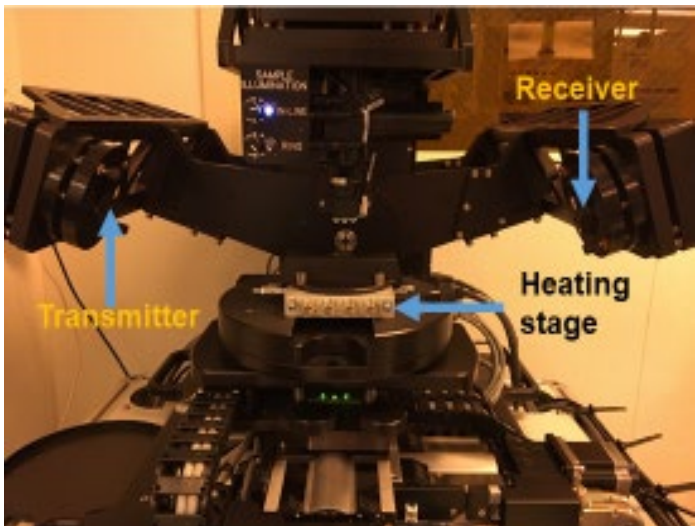

Figure A.1 In situ Ellipsometry of thin film.

The Cauchy equation is one of the most used equations to determine *n* and *k* of thin films from raw VASE data. The equation is specifically applicable to transparent or partially transparent films. The Cauchy equation is an empirical relationship between the *n* and wavelength (λ).

$$n(\lambda) = A + \frac{B}{\lambda^2} + \frac{C}{\lambda^4}$$

$$k = kamp \cdot e^{\exp(E - Bandedge)}$$

Here, A, B, C are coefficients that are determined for material by fitting the equation to measured refractive indices at known wavelengths. And *kamp* and *exp* are fit parameters for determining the shape of absorption.

Other equations can also be used to model the ChG layer like General Oscillator and B-spline. Both of these are used to model comparatively absorbing thin films. For the most part, Ge-Se thin films can be successfully modeled using the Cauchy equation. The result of the modeling further verifies the selection of the equation.

Model Description

ChGs on single crystalline silicon is modeled as shown in Figure A.2. Si_JAW and NTVE_JAW are inbuilt models of crystalline silicon and native oxide, respectively. Layer 2 is the Cauchy equation that represents the ChG. The values of A, B, C, *kamp* and *exponent* are Cauchy fitting parameters.

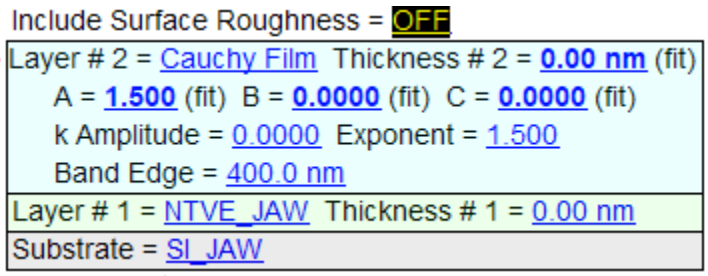

Figure A.2 ChG on Silicon model.

In addition to that, a surface roughness layer is added on top of layer 1.

Modeling

The native oxide layer was fixed at a value of 2 Å. Initially, absorption parameters *kamp*, *exp* and surface roughness were turned off. The model was fitted with 4 parameters, A, B, C and thickness.

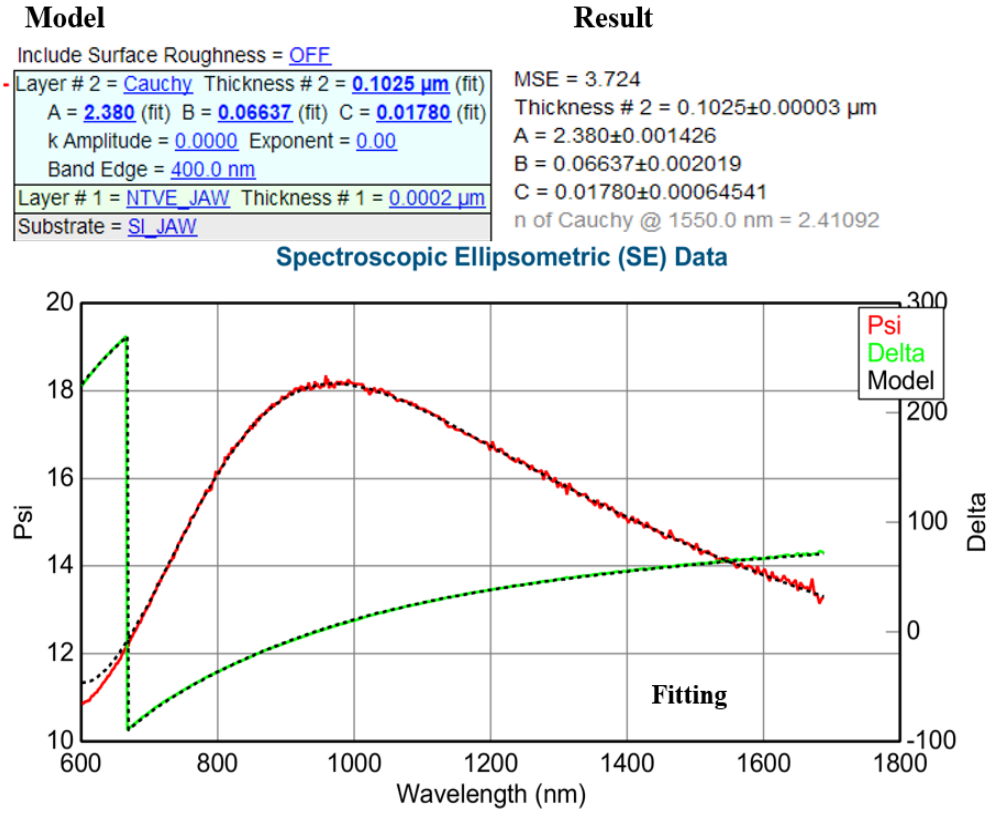

Figure A.3 Ellipsometry modeling (simplified).

Figure A.3 shows that the model satisfactorily fits the data. Near 600 nm, there is a deviation between the model and experimental *psi*. But overall mean squared error (MSE) is around 3, which indicates good fitting. The simplified modeling is useful to have a good starting point for thickness estimation. Once this is achieved with low MSE, both absorption and surface roughness were introduced in the model.

Figure A.4 shows the result of the model with absorption and surface roughness. This model shows a bit higher thickness (~0.006µm), A, C and lower B. So the MSE is not reduced significantly after introducing absorption and surface roughness, but the fitting has improved near 600 nm. From this model, the *n* and *k* values are extracted and shown in Figure A.5. This method was applied to collect *n* and *k* values at 1550nm wavelength, which is further used in device modeling.

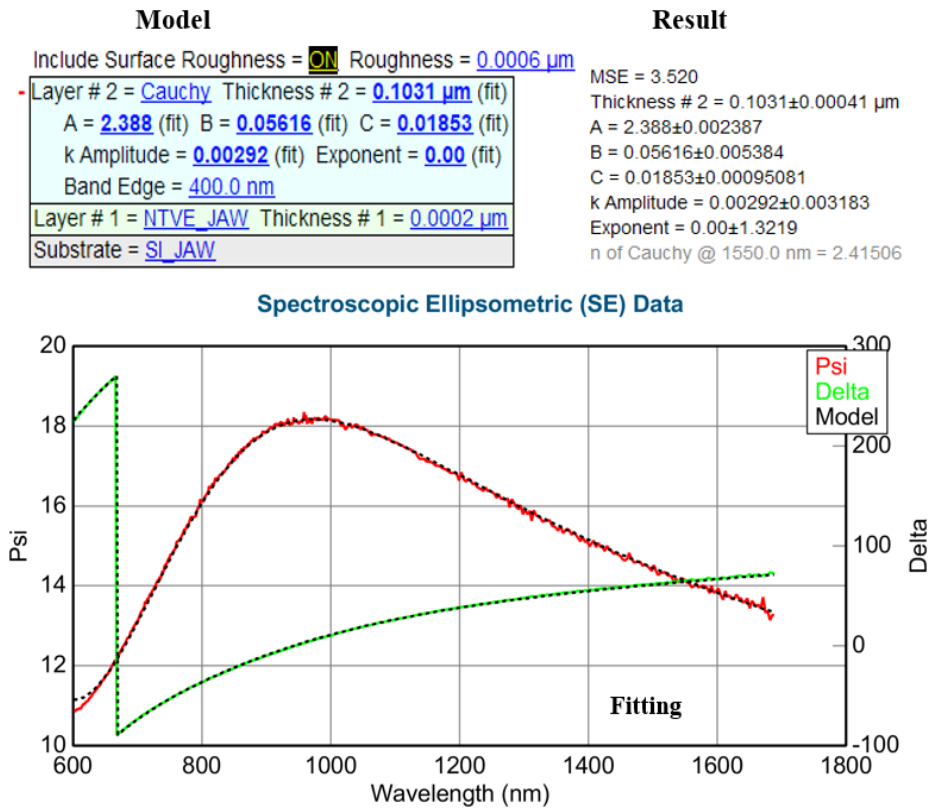

Figure A.4 Ellipsometry modeling with absorption and surface roughness.

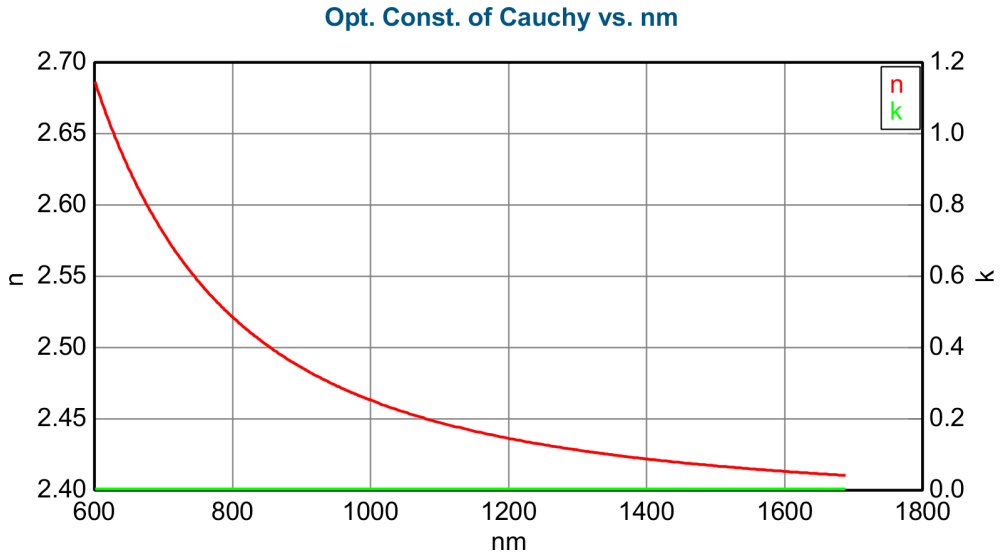

Figure A.5 n and k of amorphous Ge30Se70.

Table A.1 DSC Data for Ge_xSe_{100-X} at Different Heating Rates

Heating Rate (°C/min)	Composition (x)	Crystallization Onset Temperature, T_o (°C)	Glass Transition Temperature, T_g (°C)	Peak Crystallization Temperature, T_c (°C)	End of Crystallization Temperature, T_{c_end} (°C)	$\Delta T_c = T_c - T_g$ (°C)
10	30	440.9 ± 0.1	334.8 ± 0.1	470.3 ± 0.1	495.1 ± 0.1	135.6 ± 0.1
15	30	450.7 ± 0.1	346.1 ± 0.1	485.0 ± 0.1	515.2 ± 0.1	138.9 ± 0.1
20	30	469.3 ± 0.1	350.5 ± 0.1	501.2 ± 0.1	527.9 ± 0.1	150.7 ± 0.1
25	30	472.2 ± 0.1	363.8 ± 0.1	506.4 ± 0.1	541.3 ± 0.1	142.6 ± 0.1
30	30	486.9 ± 0.1	364.4 ± 0.1	518.8 ± 0.1	550.7 ± 0.1	154.4 ± 0.1
10	33	485.5 ± 0.1	396.3 ± 0.1	527.7 ± 0.1	563.6 ± 0.1	131.4 ± 0.1
15	33	492.1 ± 0.1	401.1 ± 0.1	545.1 ± 0.1	589.2 ± 0.1	144.0 ± 0.1
20	33	498.7 ± 0.1	412.8 ± 0.1	553.6 ± 0.1	593.1 ± 0.1	140.8 ± 0.1
25	33	499.5 ± 0.1	410.9 ± 0.1	557.0 ± 0.1	598.8 ± 0.1	146.1 ± 0.1
30	33	508.6 ± 0.1	429.7 ± 0.1	565.6 ± 0.1	612.0 ± 0.1	135.9 ± 0.1
10	40	446.6 ± 0.1	343.7 ± 0.1	472.3 ± 0.1	498.0 ± 0.1	128.6 ± 0.1
15	40	449.7 ± 0.1	347.0 ± 0.1	482.0 ± 0.1	511.5 ± 0.1	135.0 ± 0.1
20	40	470.2 ± 0.1	349.7 ± 0.1	485.6 ± 0.1	498.7 ± 0.1	135.9 ± 0.1
25	40	472.1 ± 0.1	350.9 ± 0.1	493.1 ± 0.1	535.9 ± 0.1	142.2 ± 0.1
30	40	488.7 ± 0.1	353.4 ± 0.1	501.1 ± 0.1	537.9 ± 0.1	147.7 ± 0.1

Table A.2 Calculation of Activation Energy of Crystallization

Equation	Composition	E_{ac} (kJmol^{-1})	E_{ao} (kJmol^{-1})
Kissinger	30	98.7 ± 6.8	92.8 ± 12.2
Kissinger	33	152.6 ± 14.7	227.7 ± 32.6
Kissinger	40	174.5 ± 20	95 ± 21.1
Ozawa	30	111.4 ± 6.8	105.1 ± 12.2
Ozawa	33	166.2 ± 14.7	240.5 ± 32.6
Ozawa	40	187.2 ± 20	107.3 ± 21.1
Augis-Bennett	30	105.1 ± 6.8	98.9± 12.2
Augis-Bennett	33	159.4± 14.7	234.1± 32.6
Augis-Bennett	40	180.8± 20	101.1± 21.1

Table A.3 Calculation of Activation Energy from Matusita's Equation

Composition (x)	Slope Matusita	Constant	E_c (kJmol^{-1})	E_o (kJmol^{-1})	m	Ec Matusita (kJmol^{-1})
30	-564.9 ± 27	91.1 ± 4.4	105.1 ± 6.8	98.9 ± 12.2	3	179 ± 8.6
30	-518.5 ± 40.3	81.8 ± 6.4	105.1 ± 6.8	98.9 ± 12.2	3	164.3 ± 12.8
30	-536.8 ± 26.6	83 ± 4.1	105.1 ± 6.8	98.9 ± 12.2	3	170.1 ± 8.4
30	-467.6 ± 32.9	71.6 ± 5.1	105.1 ± 6.8	98.9 ± 12.2	3	148.2 ± 10.4
30	-489.3 ± 32.3	73.7 ± 4.9	105.1 ± 6.8	98.9 ± 12.2	3	155 ± 10.2
33	-391.5 ± 14.3	58.6 ± 2.2	159.4 ± 14.7	234.1 ± 32.6	1	334.1 ± 12.2
33	-396 ± 14.3	57.7 ± 2.1	159.4 ± 14.7	234.1 ± 32.6	1	376.4 ± 13.6
33	-360 ± 29.3	52 ± 4.2	159.4 ± 14.7	234.1 ± 32.6	1	342.2 ± 27.9
33	-358.7 ± 9	51.5 ± 1.3	159.4 ± 14.7	234.1 ± 32.6	1	341 ± 8.6
33	-406.6 ± 23.9	57.8 ± 3.4	159.4 ± 14.7	234.1 ± 32.6	1	386.5 ± 22.7
40	-646.7 ± 30.1	104.2 ± 4.9	180.8 ± 20	101.1 ± 21.1	3	204.9 ± 9.5
40	-560.8 ± 19.7	89 ± 3.1	180.8 ± 20	101.1 ± 21.1	3	177.7 ± 6.2
40	-544.2 ± 25.6	84.1 ± 4	180.8 ± 20	101.1 ± 21.1	3	172.4 ± 8.1
40	-487.2 ± 34.3	74.6 ± 5.3	180.8 ± 20	101.1 ± 21.1	3	154.4 ± 10.9
40	-573 ± 29.6	86.4 ± 4.5	180.8 ± 20	101.1 ± 21.1	3	181.6 ± 9.4

APPENDIX B

Calculation of Atomic Density from SRIM Stopping/Range Table

Figure B.1 Calculation of atomic density from SRIM.

In this window put in the composition by adding elements and their stoichiometry on a scale from 0 to 1. Unless we are interested in the stopping power and range the ion, its energy etc. does not need to be changed.

Now we have the atomic density.

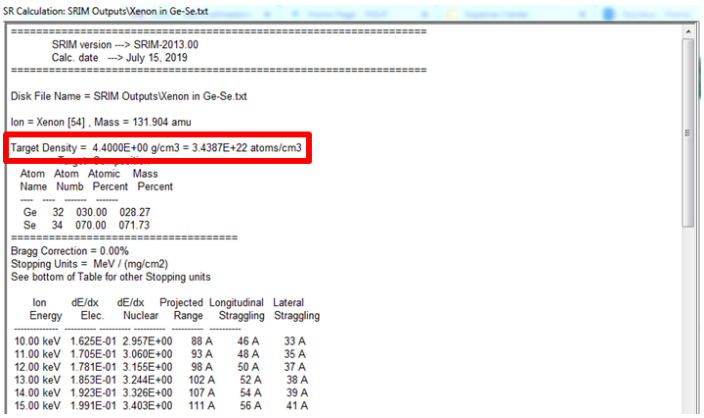

Figure B.2 Atomic density from SRIM.

Calculation of the Damage Rate (DR)

After selecting TRIM calculation on the home window of SRIM. Design the layers with corresponding composition, density and thickness can be elaborated. Ion element, number of ions, energy, and angle of incidence are also need to be selected here. After setting up everything click “Save Input & Run TRIM”.

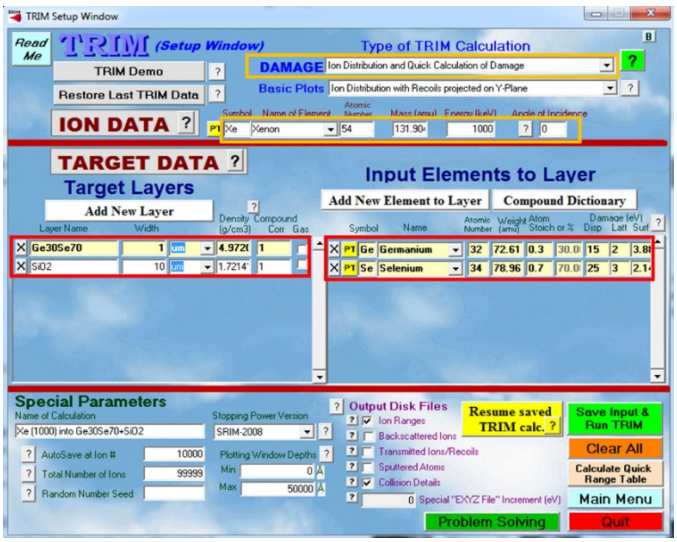

Figure B.3 Simulation setup in TRIM.

This will open several windows, each showing ions moving inside the layers from different planes.

After around 2000 incident ions, select "Damage Events" from the left-hand side menu (Figure B.4 (a)). The best would be to run it for at least 10000 ions. This will open a window with a plot like as shown in Figure B.4 (b). From this plot we get the "damage rate" at different depth which will be used for DPA* calculation. This is also function of penetration depth. For this calculation we have chosen the peak value of collision events which is somewhere in the middle of the ChG thin film. To check the interface the DR must be read at the interface of the plot, which is around 2.

Damage Rate, Time, Fluence and DPA Calculation:

$\mathbf{DR = 3.25 \frac{\#}{(Angstorm.ion)}}$ [For maximum damage rate from the plot]

Atomic Density, $N = 3.4 * 10^{22} cm^{-3}$

Current = 0.201μA [From experimental setup]

Charge of the ion, q= +1 for +1 ions, and e= $1.6 * 10^{-19} C$

Q= q*e

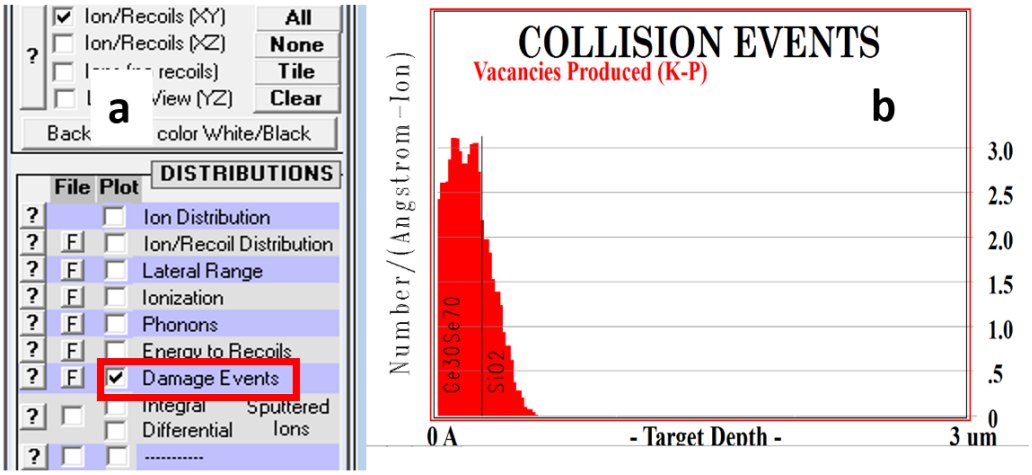

Figure B.4 a) Menu to get Damage Events and b) Damage Rate.

Area, $A = 4cm^2$ (From experimental setup)

So, to induce (for example) 5 DPA of damage at the interface of 250 nm $Ge_{30}Se_{70}$/ 1um Si with 600keV Xe^{1+} ions, where the beam/sample area, A is going to take

$$\textbf{Time} = \frac{\boldsymbol{DPA*Q*N*A}}{(\textbf{Current*DR})} \text{ sec}$$

=3108 sec

=52 min

$$\textbf{Fluence} = \frac{\boldsymbol{Time*Current}}{\textbf{Q*A}}\, cm^{-2}$$

$$= 4.86 * 10^{14} cm^{-2}$$

***DPA (Displacements per atom)** is the number of times that an atom is displaced for a given fluence.

APPENDIX C

Appendix C includes the crystallization temperature and optical properties of ChG materials in both amorphous and crystalline phases.

Table C.1 Summary of the measured complex refractive indices of synthesized glasses in amorphous and crystalline phases at 1550 nm wavelength.

Composition	Refractive index		Temperature (°C)		
	Amorphous	Crystalline	T_g (°C)	T_o (°C)	T_c (°C)
$Ge_{30}S_{70}$	2.17406+i0	1.77269+i0.11865	402	572	605
$Ge_{40}S_{60}$	2.6768+i0	2.72309+i0.17664	355	408	413
				480	489
$Ge_{33}S_{67}$	2.31779+i 8.28^{-6}	1.92455+i0.02458	435	644	694
$Ge_{30}Se_{70}$	2.37646+ $i4.06^{-5}$	3.12455+i0.25837	334.8	440.9	470.4
$Ge_{40}Se_{60}$	2.63104+i0.00575	3.1099+i0.2211	343.7	446.6	472.3
$Ge_{33}Se_{67}$	2.38753+i 0.00402	2.30756+i 0.02011	396.3	485.4	527.7

Table C.2 Measured complex refractive index of Ge40Se60 at different temperatures at 1550 nm wavelength.

Temperature (°C)	Refractive index	Temperature (°C)	Refractive index
25	2.717+i0.00547	400	2.70088+i0.01636
100	2.171516+i0.00575	450	3.35909+i0.25735
150	2.695050+i0.00547	472	3.29764+i0.09341
200	2.66978+i0.00513	479	3.1099+i0.2211
250	2.63104+i0.00575	484	3.14107+i0.22572
300	2.59792+i0.00563	500	3.2688+i0.21606
350	2.70057+i0.00938		

Table C.3 Temperature response of Ge-S and Ge-Se tip coated optical fiber-based temperature sensor

Composition	Fabrication	T_o (Expected)	T_o (measured)	T_o Time (sec)	T_c (expected)	T_c (measured)	T_c Time (sec)	T_c error
$Ge_{40}Se_{60}$	Dip-coated	446.6	460	2589	472.3	472	2627	0.3
	Evaporated	446.6	447	2462	472.3	472	2627	0.3
$Ge_{33}Se_{67}$	Dip-coated	485.5	485	2646	527.7	528	2950	0.3
	Evaporated	485.5	450	2527	527.7	485	2646	42.7
$Ge_{30}Se_{70}$	Dip-coated	440.9	400	2241	470.4	450	2527	20.5
	Evaporated	440.9	447	2462	470.4	460	2589	10.4
$Ge_{40}S_{60}$	Dip-coated	480	450	2527	489	485	2646	4
$Ge_{30}S_{70}$	Dip-coated	572	574	2830	605	600	3399	5